Spring 2020

Advanced Geometric Analyses in Vascular Disease and Interventions

Dara Ahmadi Azar

ADVANCED GEOMETRIC ANALYSES IN VASCULAR DISEASE AND INTERVENTIONS

by

Dara Ahmadi Azar

Bachelor of Science
University of Tabriz, 2015

Submitted in Partial Fulfillment of the Requirements

For the Degree of Doctor of Philosophy in

Biomedical Engineering

College of Engineering and Computing

University of South Carolina

2020

Accepted by:

Tarek Shazly, Major Professor

John F. Eberth, Committee Member

Vijaya B. Kolachalama, Committee Member

Susan M. Lessner, Committee Member

Mark J. Uline, Committee Member

Cheryl L. Addy, Vice Provost and Dean of the Graduate School

DEDICATION

I dedicate this dissertation to my family: to my bābā Mansour, to my mammâ Shirin and to my sister Golara.

ACKNOWLEDGEMENTS

I would like to express my sincerest acknowledgement and gratitude to my PhD advisor Dr Tarek Shazly for his guidance, support, true sportsmanship and setting me up for success. I was very fortunate to join your lab and learn from you on so many levels. I appreciate the enormous amount of resources you have invested in me over the last four years in my pursuit of this doctoral degree. I would also like to thank my dissertation committee members, Dr John F. Eberth, Dr Vijaya B. Kolachalama, Dr Susan M. Lessner and Dr Mark J. Uline for their contributions to my work and their candid feedback along the way. Finally, I would like to thank all of the collaborators and friends I have had the pleasure of working with.

ABSTRACT

The central function of the vascular system is the transportation and distribution of blood throughout the body. Occurrence of various forms of vascular disease, in which this central function is compromised, is associated with high mortality and morbidity rates. Vascular disease is an active and multifactorial process causing changes in local hemodynamics and blood vessel wall mechanics. The work presented here aims to advance the current knowledge on the role of local geometrical parameters in vascular disease and endovascular intervention modalities. In our first set of studies, we develop a computational framework to understand the role of aortic geometry in abdominal aortic aneurysm wall mechanics, with the purpose of predicting peak wall stress and the risk of rupture. In our next set of studies, we seek to understand possible associations between local hemodynamics and geometric variables in severe carotid artery stenosis (CAS). Using key geometric descriptors of CAS, we formulate stress-based prediction models that can be useful in disease progression risk stratification. In regard to geometric analyses in an endovascular device technology, studies are focused on identifying microstructure-function relations in drug-coated balloon (DCB) therapy and developing upon current DCB excipient design. The DCB therapy is an emerging intervention procedure with a great scope for improvement, that integrates angioplasty with local drug delivery to restore lumen patency at atherosclerotic lesion sites. Taken together, results from these studies can

contribute to clinical practices and healthcare market in capacities including disease severity diagnosis, surgical decision making, and endovascular therapy technologies.

TABLE OF CONTENTS

Dedication iii

Acknowledgements iv

Abstract v

List of Tables x

List of Figures xi

List of Abbreviations xiii

Chapter 1: Introduction 1

1.1 Clinical motivation 1

1.2 Hypotheses 5

1.3 Dissertation scope and specific aims 6

Chapter 2: Mechanical and geometrical determinants of wall stress in abdominal aortic aneurysms: a computational study 8

2.1 Abstract 9

2.2 Introduction 9

2.3 Methods 11

2.4 Results 16

2.5 Discussion 18

2.6 Acknowledgements 23

Chapter 3: Geometric determinants of local hemodynamics in severe carotid artery stenosis 32

3.1 Abstract 33

3.2 Introduction 33

3.3 Methods 35

3.4 Results 40

3.5 Discussion 44

3.6 Conclusion 46

3.7 Acknowledgements 47

Chapter 4: Intrinsic coating morphology modulates acute drug transfer in drug-coated balloon therapy 55

4.1 Abstract 56

4.2 Introduction 57

4.3 Materials and methods 59

4.4 Results 65

4.5 Discussion 68

4.6 Acknowledgements 72

Chapter 5: Surface modification using ultraviolet-ozone treatment enhances acute drug transfer in drug-coated balloon therapy 80

5.1 Abstract 81

5.2 Introduction 81

5.3 Methods 84

5.4 Results 88

5.5 Discussion 90

5.6 Acknowledgments 93

Chapter 6: Dissertation summary and conclusion 99

6.1 Major contributions to the field 99

6.2 Future works 99

References 103

Appendix A: Journal permission for Use of Manuscript 120

LIST OF TABLES

Table 2.1: Geometric parameter values for the baseline AAA (underlined) and associated parametric studies. 24

Table 2.2: Mechanical properties for referent normal aortic tissue. 24

Table 2.3. Mechanical property values for the baseline AAA (underlined) and associated parametric studies. 25

Table 2.4. Sensitivity of PWS to geometrical and mechanical parameters characterizing AAA. 25

Table 3.1: Definition of geometric variables with respective formulae. 48

LIST OF FIGURES

Figure 2.1: Referent normal aortic and baseline AAA geometries. 26

Figure 2.2: Circumferential (angular) extent of AAA bulging. 27

Figure 2.3: Predicted von Mises wall stress 28

Figure 2.4: Effects of AAA geometrical properties. 29

Figure 2.5: Effects of AAA mechanical properties. 30

Figure 2.6: Interactive effects of geometrical and mechanical properties. 31

Figure 3.1: Carotid artery reconstruction and the 2D illustration of stenotic carotid artery. 49

Figure 3.2: Descriptive statistics of CTA-based geometric variables and results obtained from CFD simulations. 50

Figure 3.3: 3D mapping of CFD results for representative samples from each stenotic subclassification, and the distribution of hemodynamics vs. the degree of stenosis. 51

Figure 3.4: Spearman correlation analysis results for ρ demonstrating the strength of the association between hemodynamic and geometric variables. 52

Figure 3.5: Relationship between hemodynamic variables obtained from CFD results with respect to the regression models and respective residuals. 53

Figure 4.1: Mechanical testing setup and a typical mechanical testing result. 74

Figure 4.2: Force-displacement curves. 75

Figure 4.3: Intrinsic shape of the balloon coatings. 76

Figure 4.4: Bulk interfacial mechanics are independent of excipient type. 77

Figure 4.5: Excipient microstructure modulates acute transfer of balloon coating. 78

Figure 4.6: Cytotoxicity of the excipients..... 79

Figure 5.1: UVO treatment of Nylon-12 films. 94

Figure 5.2: Experimental setup design for simulated DCB deployment. 94

Figure 5.3: Microstructure of coating constituents. 95

Figure 5.4: Contact angle measurement..... 95

Figure 5.5: Coating microstructure changes due to surface modification. 96

Figure 5.6: Morphological analysis of the coatings. 96

Figure 5.7: Estimation of drug delivery efficiency. 97

Figure 5.8: Correlation among biophysical response variables. 98

Figure 6.1: Nylon 12 structure and XPS analysis of UVO surface treatment. 102

Figure A.1: Permission from PLOS Journals – PLOS One to include published manuscript in this dissertation. 120

Figure A.2: Permission from Elsevier Journals – Computers in Biology and Medicine to include published manuscript in this dissertation. 120

Figure A.3: Permission from Springer Nature – Scientific Reports to include published manuscript in this dissertation. 121

Figure A.4: Permission from ACS Publications – Langmuir to include submitted, accepted or published manuscript in this dissertation. 121

LIST OF ABBREVIATIONS

2D..... Two Dimensional

3D..... Three Dimensional

AA..... Abdominal Aorta

AAA..... Abdominal Aortic Aneurysm

ANOVA.....Analysis of Variance

ATP..... Adenosine Triphosphate

AWS..... Averaged Wall Stress

CAD..... Computer-aided Design

CAS..... Carotid Artery Stenosis

CCA..... Common Carotid Artery

CEA.....Carotid Endarterectomy

CFD.....Computational Fluid Dynamics

CS..... Cross Section

CTA.....Computed Tomography Angiography

DCB..... Drug Coated Balloon

DES..... Drug Eluding Stent

DICOM.....Digital Imaging and Communications in Medicine

DSA .....Drop Shape Analyzer

FACS ..... Fluorescence Activated Cell Sorting

FD ..... Force-Displacement

FDA ..... Food and Drug Administration

FEA ..... Finite Element Analysis

FTIR ..... Fourier-transform Infrared Spectroscopy

HPLC ..... High Performance Liquid Chromatography

ICA ..... Internal Carotid Artery

IRB ..... Institutional Review Board

LC-MS ..... Liquid Chromatography–Mass Spectrometry

MRI ..... Magnetic Resonance Imaging

NASCET ..... Magnetic Resonance Imaging

NIH ..... National Institutes of Health

NSF ..... National Science Foundation

OSI ..... Oscillatory Shear Index

PAD ..... Peripheral Artery Disease

PTA ..... Percutaneous Transluminal Angioplasty

PTX ..... Paclitaxel

PWS ..... Peak Wall Stress

ROI ..... Region of Interest

RRT ..... Relative Residence Time

SEM ..... Scanning Electron Microscopy

TAWSS ..... Time-averaged Wall Shear Stress

UV ..... Ultra-violet

UVO ..... Ultra-violet Ozone

WSS ..... Wall Shear Stress

XPS ..... X-ray Photoelectron Spectroscopy

CHAPTER 1

INTRODUCTION

1.1 CLINICAL MOTIVATION

Despite advances in diagnostic and therapeutic interventions aimed at eradication of vascular disease, it remains the leading cause of morbidity and mortality in the United States. Vascular disease is often referred to as pathological state of arteries, includes coronary artery diseases and peripheral artery disease (PAD) as well as stroke and aneurysms. Most vascular disease affect older adults; In the United States 16.5 million individuals are affected by coronary artery disease, 8-12 million people various types of PAD and almost a million people have a stroke every year [1,2]. The incidence of various types of vascular disease creates $400 billion burden annually, which is estimated to be increasing [3].

Vascular Disease

Vascular disease can be diverse in terms of mechanism and pathophysiology, yet various phenotypes of vascular disease can be identified with some abnormalities in geometric characteristics. These geometric alterations are believed to reflect the development of vascular disease and exacerbate function and pathology progression. Medical diagnosis of the disease and determining the severity of pathology is closely associated with the following intensity of treatment that directly affects clinical outcome [4].

The systematic consideration of vascular geometry in relation to a pathological state can determine healthcare actions and outcome in a worthwhile manner. Thus, there is a substantial need to utilize more selective approaches in clinical decision making to intervene or manage disease progression, as perioperative and long-term risks of vascular repair procedures still figure prominently [5–7]. Below, two cases are discussed in detail.

Abdominal Aortic Aneurysm

Abdominal aortic aneurysm (AAA) is closely associated with rupture-related death and procedural risks [8–10]. AAA development is unequivocally a multifunctional process involving systematic changes in material composition and mechanical behavior, and followed by focal geometric adaptations. A mechanism postulated for AAA formation focuses on inflammatory processes that lead to matrix metalloproteinases production and elastase release; a chain of events thought to be associated with enzymatic degradation of structural proteins and AAA expansion [11,12]. Further regional changes in material properties are interrelated with geometric adaptations and contribute to the disease progression until wall stress exceeds the tensile strength of the arterial tissue and the AAA rupture occurs. Around 80% of patients with ruptured aorta will not survive this fatal yet preventable event [13]. Current method in determining the severity of AAA is to use the maximum transvers diameter of abdominal aorta (AA) criterion. However, autopsy reports indicate this current approach is not a reliable indicator since small aneurysms can also rupture, while many aneurysms can become very large without rupturing [14]. Furthermore, in majority of patients, AAA remains to be asymptomatic and often under-diagnosed [13,15]. A more inclusive approach of evaluating AA that accounts for regional attributes of the disease

geometry and changes in mechanical properties, with respect to progression of AAA, can more accurately match patients with their appropriate treatment options.

Carotid Artery Stenosis

Carotid artery stenosis (CAS) is an atheromatous narrowing of the common carotid artery or internal carotid artery and is responsible for 10-20% of all strokes [16]. The carotid arteries are major blood vessels, which at their healthy state, carry regulated blood flow and perfuse the structures of the head and neck. Nevertheless, anatomical anomalies such as siphons and branching in the different sections of the carotid artery disrupt the blood flow pattern and generate mechanical forces that cause flow recirculation, consequently, reduce shear stress/blood flow velocity [17–20]. Such reduction in the wall shear stress or creation of recirculation patterns cause endothelial dysfunction, which can lead to modifying the internal vascular structure by accumulation of atherosclerotic plaque. The progression of atherosclerosis can result in stroke or embolism. Carotid endarterectomy (CEA) remains the most commonly performed surgical treatment for symptomatic and asymptomatic carotid atherosclerotic disease [21,22]. Carotid angioplasty with stenting or other catheter-based treatment options are minimally invasive alternative approaches to CEA. Since the initial development of these intervention options, clinicians have debated around whether CEA, endovascular treatment options, or medication therapy alone is most appropriate in patients with symptomatic and asymptomatic carotid stenosis [16]. In recent years a more selective approach in classification of CAS has attracted attention due to concerns involving post-endarterectomy restenosis, perioperative risks, and comorbidities that preclude major operations. Nevertheless in practice, CAS geometry-based risk analysis is limited to a single-point measured stenotic diameter reduction, which is the backbone

current clinical decision making guidelines [7]. Current criteria do not account for regional heterogeneity, which is shown to induce patient-specific variations in hemodynamic and consequently dissimilar disease severity given the same diameter decrease [16,23,24].

Endovascular Technology – Drug Coated Balloon

Recent advances in endovascular therapies have broaden the options for treating vascular disease [25,26]. Drug-coated balloon (DCB) therapy is an emerging technology and a case in point here. A DCB consists of a standard angioplasty balloon catheter coated with an antiproliferative drug. During the DCB procedure, a deflated coated angioplasty balloon is tracked through arteries using a guide wire to the treatment site, where the DCB is inflated using an expansive force. Balloon inflation is used to disrupt the atherosclerotic plaque, delaminate the coating and transfer the therapeutics to the lumen of the artery. DCBs are currently used to treat various atherosclerosis-induced vascular diseases by opening up the blocked arteries and delivering antiproliferative therapeutics locally to prevent restenosis [27–32]. DCB therapy has multiple potential advantages over other endovascular procedures such as bare-metal stent and drug-coated stent. Primarily, DCB does not leave an implant in the treatment site, therefore, avoids metal- or polymer-induced restenosis (renarrowing of arteries) and stent fracture associated with stent implantation or stent fatigue. In theory, DCBs distribute antiproliferative drugs more homogenously than stents do and DCBs become more favorable for in-stent restenosis where avoidance of stent placement is recommended [33]. Most DCBs currently available are coated with drugs either directly without using any excipients (an excipient is an inactive substance that provides a platform to carry drug on the balloon surface and to deliver it in a controlled manner) or using different types of excipients [34,35]. Most of these excipients are selected based on their

utility to improve drug penetration into the tissue. An effective DCB excipient, among other considerations, provides structural stability as well as promoting favorable physical or chemical properties of the coating. Currently, there are major limitation related to the available DCBs, despite the great potential of the treatment. The delivery of drug from the coated balloons is neither controlled nor adequate in order to avoid drug loss during balloon tracking, arterial disruption and extended inflation time [34]. It has been reported that a substantial amount of the initial therapeutic load (up to 80%) is lost in the blood stream even before the balloon is tracked to the treatment site [34,36]. Hence, in many cases, only an insufficient level of drug is delivered at the treatment site [34,35]. Therefore, a pressing need has arisen to control the delivery of drug from the balloons to the treatment site during the short time of balloon inflation. A more efficient DCB therapy will allow for lower doses of initial therapeutic loading, possibly will cause less arterial disruption in the site of treatment by application of more regulated magnitudes of expansive force.

1.2 HYPOTHESES

Following chapters discuss a series of studies that aim to investigate the role of geometry in understanding the severity of vascular diseases, clinical decision-making process and endovascular drug delivery device development [37–40]. The central hypotheses in these studies include the following: 1) Examining isolated and combined effects of local geometrical descriptors and material properties of idealized AAAs can provide insight into the contribution of different parameters to AAA rupture risk. 2) Regional hemodynamics of CAS, and wall shear stress-based disease progression risk can be estimated using a set of geometric variables of stenotic plaque and parent vessel. 3) A judicious choice of DCB excipient based on intrinsic geometry of coating can systematically control drug uptake by

arterial tissue. 4) Systematic and repeatable manipulation of DCB microstructural geometry can increase drug transfer, while forming a biocompatible and structurally stable coating.

1.3 DISSERTATION SCOPE AND SPECIFIC AIMS

Dissertation projects collectively highlighted the significant role of geometry in vascular disease and an endovascular intervention technology, DCB. For instance, in evaluating AAA rupture risk both geometric and material properties were considered to investigate the contribution of each factor in wall stress estimation. Both geometric and material properties of AAA pathology were found to be significant, yet select key factors in isolation resulted in more drastic changes in wall stress. In case of carotid artery stenosis, a diverse set of geometric variables were defined and extracted from medical images of CAS, and correlations with local hemodynamics were studied. As reported previously, hemodynamics of CAS can be related to the risk of stroke, embolic events and disease progression. Therefore, this study focused on developing a framework that can predict hemodynamics based on patient-specific geometry descriptor without resources necessary for individual simulations. Finally, microstructural analysis of DCB therapy is another case in point; where coating contact mechanics and DCB drug excipient geometry were researched. This work found an association between a DCB procedural factor, application force, coating intrinsic shape and acute drug transfer. Results of this study inspired more research in this field in order to increase DCB therapeutic efficacy. Research activities in this area aim to explore effects of systematic and repeatable changes to DCB surface on drug transfer, and ultimately identify and produce a more ideal surface characteristics to

optimize the DCB therapy with respect to procedural factors including application force and time.

CHAPTER 2

MECHANICAL AND GEOMETRICAL DETERMINANTS OF WALL STRESS IN ABDOMINAL AORTIC ANEURYSMS: A COMPUTATIONAL STUDY[1]

[1] Azar D., Ohadi D., Rachev A., Eberth J. F., Uline M. J., Shazly T., 2018. Mechanical and geometrical determinants of wall stress in abdominal aortic aneurysms: A computational study. *Plos One*. 13:e0192032.
DOI: https://doi.org/10.1371/journal.pone.0192032
Reprinted here with permission of publisher.

2.1 ABSTRACT

An aortic aneurysm (AA) is a focal dilatation of the aortic wall. Occurrence of AA rupture is an all too common event that is associated with high levels of patient morbidity and mortality. The decision to surgically intervene prior to AA rupture is made with recognition of significant procedural risks, and is primarily based on the maximal diameter and/or growth rate of the AA. Despite established threshold levels for intervention, rupture occurs in a notable subset of patients exhibiting sub-critical maximal diameters and/or growth rates. Therefore, a pressing need remains to identify new predictors of rupture risk and ultimately integrate their measurement into clinical decision making. In this study, we use a series of finite element-based computational models that represent a range of plausible AA scenarios, and evaluate the relative sensitivity of wall stress to geometrical and mechanical properties of the aneurysmal tissue. Taken together, our findings encourage an expansion of geometrical parameters considered for rupture risk assessment, and provide perspective on the degree to which tissue mechanical properties may modulate peak stress values within aneurysmal tissue.

2.2 INTRODUCTION

A significant manifestation of cardiovascular disease involves a regional dilation of the aorta termed an aortic aneurysm (AA) [6,41–55]. Diagnosed using ultrasonography, computed tomography, or magnetic resonance imaging, a segment of the aorta that is found to be greater than 50% larger than that of a healthy individual of the same sex and age is considered aneurysmal [56]. AA can arise in either the thoracic or abdominal sections, with current estimates that over a quarter-million new cases of AA occur each year in the United

States alone. Thus, several million patients carry the diagnosis of AA, and unfortunately a significant portion of these patients will either die from rupture or morbidity arising from complex surgical/endovascular repairs.

While stimuli for AA genesis and progression can be diverse, wall rupture is ultimately a mechanical failure that occurs when intramural stresses exceed wall strength [11,57]. Intramural stresses generally increase with aneurysm growth and inherently depend on the applied loads, the geometry and location of the AA, and the mechanical properties of the aortic wall. Despite the multiple determinants of wall stress, a set-point point of 5.0 – 5.5 cm in diameter is the typical threshold for surgical intervention [46,51]. Endovascular or surgical repair of AA is not without significant costs and complications [6,41,46,47,49,52]. Therefore, any advancement in terms of assessing the risk of AA rupture would be of high clinical significance.

Computational modeling utilizing finite element analysis (FEA) is a well-established approach to predict wall stresses in the context of AA. Previous studies have shown that, in addition to maximum AA diameter, centerline tortuosity is a deterministic parameter in AA rupture risk [58,59]. Other studies have also suggested that indices of AA surface curvature and wall thickness impact rupture risk [60], primarily via correlation of rupture location with geometrical features of the AA [61]. The results of any FEA-based study are highly dependent on the employed material models and distinct domains in which wall stress is computed. A previous study that assessed ruptured and non-ruptured AA via computed values of the peak wall stress (PWS) demonstrated that incorporation of various levels of geometric complexity derived from computed tomography data could significantly impact obtained results [62]. Thus, if the modeling objective is to generate a

patient-specific prediction of wall mechanics in the context of AA, it is likely that high-fidelity geometries and accurate material models would be required.

As opposed to generating patient-specific predictions of AA wall mechanics, the purpose of this study is to compare the isolated and synergistic effects of general geometric and mechanical properties on AA rupture potential in idealized scenarios. Although both contribute significantly to the wall stresses experienced by the AA under physiological loading, only the former is regularly considered in risk analysis with most interventional criteria focused on diameter measurements alone. We systematically explore certain geometrical characteristics descriptive of AA (i.e., location within the parent vessel, axial/circumferential extent, thickness, and tortuosity) which may significantly increase mural stress levels and thereby warrant an elevated risk status for the patient. While noninvasive measurement of AA mechanical properties is admittedly limited, we utilize established constitutive models and prior studies to provide reasonable estimates of baseline mechanical properties. Thus we explore the potential for the use of representative mechanical properties, in combination with diverse but accessible measurements of AA geometric properties, as a basis for risk evaluation [63–65].

2.3 METHODS

Overview A series of finite-element based computational models of human abdominal aorta that are based on classic continuum mechanics were developed to quantify the wall stress field in the context of abdominal aortic aneurysm (AAA) under normotensive conditions. The premise of our study is that while the deformed diameter of AAA is the clinical standard for estimating rupture risk, other AAA characteristics may be useful in predicting local elevations in wall stress. Computational parametric studies were

designed to isolate the dependence of wall stress on aneurysm geometry/location and tissue mechanical properties; the interactive effects of select characteristics on wall stress were also analyzed. Two response variables were extracted from each simulation, namely the average and peak Von Mises stress within the aneurysmal region.

2.3.1 Referent Normal Aortic Geometry

The constructed geometry of the abdominal aorta and the aortic bifurcation were based on previous anatomical examinations [66]. Three-dimensional (3-D) geometrical models of the aorta (with and without AAA) were generated using CATIA V5R21 CAD software. All models entail a symmetric aorta-iliac bifurcation and common iliac arteries. The referent normal aortic geometry has dimensions: length (L) of 120 mm; outer diameter (D) of 20 mm; uniform wall thickness (t) of 2 mm (Figure 2.1A-B). The proximal diameter of the iliac arteries is 13 mm and gradually decreases to 10.3 mm over the considered length of these vessels (42 mm). The take-off angle of the iliac arteries at the bifurcation (α) and the angle between the aortic centerline and the plane formed by both iliac arteries (β), are 20° and 15°, respectively. The radii of curvature at the aorta-iliac junction is 50 mm on both sides.

2.3.2 AAA Geometric Parameters

Geometric parameters used to characterize AAAs are defined with reference to cross-sectional planes (CS0 – CS8) spanning the longitudinal section of the aorta as follows: axial and circumferential extent of the AAA region, axial location of the AAA region, maximum transverse outer diameter of AAA region, local wall thickness and centerline tortuosity of the AAA region (Figure 2.1C-D). The baseline values and

examined range for each geometric parameter (described below) were motivated by clinical observations of AAA (Table 2.1).

2.3.3 AAA Geometry

The longitudinal length of the aorta considered for geometric variation (L*) is 128 mm and is defined by nine cross-sections (CS0 – CS8) that are parallel to XY-plane (Figure 2.1C). To impart geometric variations reflective of AAA and enable parametric computational studies, CS0 – CS8 were systematically manipulated and then closed splines connecting their perimeters were applied to define outer and inner surfaces. For the baseline AAA geometry, outer closed splines on CS1 and CS2 are circles (corresponding to a 360° circumferential extent) with a diameter of 45 mm; wall thickness smoothly decreases from its referent normal value of 2 mm to 1.50 mm on CS1 and CS2. All other CSs remained unchanged with respect to the previously generated referent normal aortic geometry, with the exception of CS3, which was left free of constraints to produce a smooth evolution of surfaces. The midway plan of the baseline AAA sac is located 32 mm from CS0 (Figure 2.1C-D).

For sensitivity analyses, each geometrical parameter was varied in isolation over physiologically-relevant ranges as follows: AAA location via the center of the AAA sac along the Z-axis; wall thickness via the inner splines on CS1 and CS2; maximum AAA diameter via inner and outer splines on CS1 and CS2; tortuosity in XZ- and YZ- planes via the centers of inner and outer circles on CS1 and CS2; axial extent via the number of CS planes included within AAA sac; the circumferential extent of the AAA sac via progressive reduction of the anterior quarter of CS1 and CS2 by 90° (Figure 2.2).

2.3.4 Mechanical Properties of the Referent Normal Aorta

The mechanical properties of aortic tissue were quantified using a previously developed structure-motivated constitutive model, where the strain energy function $\overline{\psi}$ is the sum of an isotropic term $\overline{\psi}_{iso}$ and anisotropic term $\overline{\psi}_{aniso}$,

$$\overline{\psi} = \overline{\psi}_{iso}(\bar{I}_1) + \overline{\psi}_{aniso}(\bar{I}_4, \bar{I}_6) \quad (2.1)$$

and $\bar{I}_1, \bar{I}_4, and\ \bar{I}_6$ are invariants of the right Cauchy-Green strain tensor [67,68]. A neo-Hookean material model is used for $\overline{\psi}_{iso}$ with the following analytical form,

$$\overline{\psi}_{iso}(\bar{I}_1) = \frac{\mu}{2}(\bar{I}_1 - 3) \quad (2.2)$$

where μ has the dimension of stress and is the only material parameter [67]. A sum of two exponential function is used for $\overline{\psi}_{aniso}$, which describes the strain energy stored by two symmetrically-oriented collagen fiber families with respect to the vessel longitudinal axis. $\overline{\psi}_{aniso}$ has the following analytical form,

$$\overline{\psi}_{aniso}(\bar{I}_4, \bar{I}_6) = \frac{k_1}{2k_2}\sum_{i=4,6}\{\exp[\,k_2(\bar{I}_i - 1)^2] - 1\} \quad (2.3)$$

where the invariants $\bar{I}_4$ and $\bar{I}_6$ correlate with the square of the stretches of two fiber families in their respective directions. Moreover, $k_1 > 0$ is a material parameter with units of stress and $k_2 > 0$ is dimensionless [67]. The referent normal values for all material parameters (Table 2.2) are based on previous ex-vivo mechanical studies of aortic tissue [69].

2.3.5 Mechanical Properties of Aneurysmal Tissue

Within the constitutive framework provided by (Equations 2.1-2.3), Pierce et al. estimated material parameters for eight human AAA samples [70]. The fitted values for all material parameters informed our specification of baseline AAA as well as the examined

ranges in parametric studies (Table 2.3). In all AAA simulations, collagen fiber angle was fixed at 45°and no fiber dispersion factor was applied.

2.3.6 Meshing, Boundary Conditions and Solving

Generated 3-D geometries were meshed using Altair HyperMesh v12.0 software package via first order hybrid tetrahedral elements. Tetrahedral elements were selected for meshing to avoid elemental collapse in model geometries with high curvature regions [71,72]. Mesh independency studies were performed on both the referent normal and baseline AAA geometries, wherein simulation results were deemed mesh-independent if additional mesh refinement led to a less than 4% change in both the peak and average von Mises stress. A total of 289,762 tetrahedral elements were required for mesh-independency, which set the minimum meshing threshold for all parametric studies. Boundary conditions were applied to the meshed geometries using a FEBio Software package pre-processor, PreView. A uniform pressure of 120mmHg (0.016 MPa) was applied to the vessel inner surface via a gradual ramping up from zero pressure. The presented results thus refer to a stationary solution. A complete motion constraint (displacement and rotation) at all vessel initiation/termination surfaces were applied to facilitate solution convergence. All studies were performed with the full Newtonian solver settings in FEBio FEA open-source software [73].

2.3.7 Post-processing of Computational Data

The direct output of all simulations (displacement vector field) was transformed using FEBio post-processor, PostView, with computed response variables including peak von Mises wall stress (PWS) and average von Mises wall stress (AWS) within the

aneurysmal sac (or analogous location for the referent normal aorta). For calculation of AWS, obtained values were weighted by element size (area-weighted average stress).

2.4 RESULTS

2.4.1 Wall Stress in the Referent Normal Aorta

Colorimetric surface plots (without gradient smoothing, anterior and posterior views) of the von Mises stress in the referent normal aorta reveal a relatively uniform wall stress distribution until the aortic bifurcation, with AWS of 0.013 MPa. A notable elevation in wall stress occurs at the aortic bifurcation, with a PWS of 0.091 MPa. Continuity of the von Mises stress field extending from the model boundaries qualitatively suggests that edge effects are minimized in the referent normal simulation (Figure 2.3A).

2.4.2 Wall Stress in AAA

Analogous surface plots of the von Mises stress field in the baseline AAA show a nonuniform wall stress distribution in comparison to the referent normal aorta. (Figure 2.3B). The AWS within the aneurysmal sac is 0.11 MPa, while a PWS of 0.76 MPa occurs near the sac center point. While stress values generally exhibit an order-of-magnitude increase in the baseline AAA as compared to the referent normal aorta, the PWS remains below the assumed ultimate strength (1 MPa) of aortic tissue [74] (discussed below).

2.4.2.1 Effects of AAA Geometry

A series of simulations were performed under isolated variation of geometric parameters with respect to the baseline AAA model. AWS and PWS computed throughout these parametric studies reveal the relative sensitivity of wall mechanics to distinct

morphological features (Figure 2.4A-G). In all parametric sweeps, the percent variability in AWS over the examined range is reduced in comparison to that of PWS.

In terms of AAA axial extent, the largest value (96 mm) induces the greatest stress levels (Figure 2.4A). Interestingly, decreasing the axial extent with respect to the baseline AAA value (64 mm → 48 mm) also results in an increase in PWS; this is understood as a local consequence of increased sac curvature in proximity to the aortic bifurcation. Variation in AAA circumferential extent, as defined in this study, also has a non-monotonic effect on PWS (Figure 2.4B). In this case, a 270° circumferential extent of the sac causes an approximately 30% increase in PWS as compared to the baseline AAA case (circumferential extent of 360°); this is a consequence of sac asymmetry and the resultant increase in local curvature on the posterior sac surface. For all other examined scenarios, both PWS and AWS exhibit a monotonic response to isolated manipulation of the defined geometric parameters (Figure 2.4C-G). Among these, the most deterministic parameters are clearly sac diameter (Figure 2.4C) and wall thickness (Figure 2.4E), for which maximal percent changes in PWS with respect to baseline AAA are 231% and 457%, respectively (Table 2.4).

2.4.2.2 Effects of AAA Mechanical Properties

A second series of parametric studies entails isolated manipulations of the AAA mechanical properties with respect to the baseline AAA model. (Figure 2.5A-C). As with geometrically-focused parametric sweeps, the percent variability in AWS over the examined range is reduced in comparison to that of PWS. PWS was notably more sensitive to mechanical properties associated with the anisotropic (as opposed to isotropic) component of the strain energy function ($\bar{\psi}_{aniso}$), with k_1 and k_2 inducing a maximal

percent changes in PWS with respect to baseline AAA of 314% and 156%, respectively (Table 2.4).

2.4.2.3 Interactive Effects of AAA Properties

A third series of parametric studies examines the relative change in sensitivity of PWS to select AAA geometrical and mechanical properties with progressively increasing sac diameter (Figure 2.6). In the case of wall thickness, a 50% reduction (2 mm → 1 mm) leads to an increase in PWS that is approximately 1 MPa when the sac diameter is 35 mm, and 2 MPa when the sac diameter is 70 mm (Figure 2.6A). Comparatively, a 50% increase in AAA axial extent (64 mm → 96 mm) leads to an increase in PWS that is less than 0.02 MPa when the sac diameter is 35 mm, but over 2 MPa when the sac diameter is 70 mm (Figure 2.6B). An even more significant interactive effect occurs when diameter changes in tandem with AAA mechanical properties. When computed over the examined range of material parameter K_1, the change in PWS is approximately 1.5 MPa at a sac diameter of 35 mm but increased to nearly 6 MPa at a sac diameter of 70 mm (Figure 2.6C).

2.5 DISCUSSION

The aim of this study is to apply finite element-based computational modeling to gain insight on the relative degree to which geometrical and mechanical properties of AAA determine the AWS and PWS within the aneurysmal sac. Potential interactive effects between select properties are also analyzed. In a similar computational model by Raghavan et al., the PWS computed for a referent normal aorta (diameter = 20 mm) was 0.12 MPa, which is close to our obtained value (0.091 MPa) [63]. As a benchmark for our baseline AAA model, we compared our results to findings by Roy et al. in which a model with similar

geometry/properties exhibited a PWS of 0.76 MPa [75]. In the same study, they also considered patient-specific geometries and found a maximum principal stress of 0.79 MPa in a mid-sized AAA [75]. The reported values for PWS in these representative AAA scenarios are close to our findings in the baseline AAA model (PWS of 0.76 MPa). Finally, Rodriguez et al. developed a representative AAA model and computed a maximum principal wall stress of 0.79 MPa, which is close in value to the PWS obtain by us and others. Analyses of peak von Mises stress and maximum principal wall stress across these studies is justified by the relatively low values of shear stresses within the vessel wall seen in our study and reported in others [76].

Aneurysmal sac rupture theoretically occurs when peak wall stress exceeds the ultimate strength of the vascular tissue. In line with this notion, it is not surprising that wall stress can predict sac rupture better maximum diameter [77,78]. To facilitate the quantification of rupture risk, numerous studies have sought to identify the ultimate tissue strength in AAA, wherein Giannoglu (2006) reported a median value of 1.23 MPa and Vande Geest et al. predicted values ranging from 0.54 MPa to 1.43 MPa [59,79]. Similarly, others suggest failure stresses on the order of 1MPa [74,80]. For the purposes of subsequent discussion, we consider the ultimate strength of the AAA wall to be 1 MPa.

Obtained results confirm that wall stress is highly sensitive to sac diameter (Figure 2.3C, Table 2.4), thereby supporting the established clinical approach of monitoring maximal sac diameter and its expansion rate for estimation of rupture risk. Our model predicts that as sac diameter reaches the standard clinical threshold for surgical intervention (5.0 – 5.5 cm), PWS is near/above the assumed ultimate strength of aortic tissue (1 MPa).

Moreover, increasing diameter above this threshold leads to a dramatic increase in PWS, supporting the need for immediate surgical intervention to prevent rupture.

Although many previous computational studies use uniform wall thickness to predict AAA mechanics [58,77,81–85], it is intuitively obvious that an isolated reduction in wall thickness will increase PWS within the aneurysmal sac. The choice to maintain a uniform wall thickness close to the baseline value is supported by some previous studies, in which AAA wall thickness was measured to be near its referent normal value [61,86]. Therefore, our predicted PWS response to varying wall thickness (Figure 2.4E) may not be applicable to all instances of AAA; rather, our results provide clinical motivation to monitor wall thickness as a precautionary measure. Indeed, a significant fraction (13%) of AAAs under 5 cm in diameter rupture [87], underscoring the need to identify additional risk factors beyond maximal sac diameter/expansion rate. Of the previous studies that did examine AAA wall thickness, Venkatasubramaniam et al. predicted that increasing/decreasing wall thickness by 25% leads to nearly a 20% decrease/increase in PWS, respectively [83]. In a multivariate study, Celi et al. (2010) showed that an AAA characterized by a relatively larger diameter and uniform thickness would exhibit reduced PWS compared to an AAA with a smaller diameter and reduced wall thickness [8]. In our study, PWS was the most sensitive to wall thickness among the explored parameter space, which therefore supports its consideration as a key factor in clinical risk assessment.

Previous studies have demonstrated that as the axial extent of the AAA increases, PWS also increases [60,81]. While our results are in line with this expectation for axial extents exceeding the baseline AAA value (above 64 mm), we also predict an increase in PWS at exceedingly low levels (48 mm). We speculate that this latter effect is a consequence on

enhanced surface curvature in the distal portion of the AAA combined with the proximity to the aortic bifurcation. Indeed, Venkatasubramaniam et al. concluded that overall shape and sac asymmetry are significant determinants of AAA wall stress [83]. Other studies have developed various methods to interrelate sac asymmetry to wall stress levels, and in all cases concluded a positive correlation between the two [81,88–90].

AAA asymmetry can be magnified by increased tortuosity, which is a recognized geometric determinant of not only wall stress but also intra-aneurysmal flow patterns and resultant flow-induced shear stresses [58,59,81,91–95]. In our parametric sweeps, the applied tortuosity variation in either the XZ or YZ planes was modest in comparison to these and other previous studies due to the increased complexity of surface assignment. Nevertheless, PWS exceeding the tissue ultimate strength was observed within our examined range (Fig 4F and G). Although not realized in this study, we expect that additional increase of AAA tortuosity would lead to even greater PWS values.

Despite containing parametric sweeps focused on AAA mechanical properties within reported ranges for AAA tissue, it is important to note that isolated property manipulation in this sense may create a scenario (set of mechanical properties) that is not reflective of aneurysmal (or referent normal) tissue. Nevertheless, computed changes in AWS and PWS compared to those observed with geometric sweeps enable qualitative speculation on the relative impact of geometrical versus mechanical properties on AAA mechanics. Based on the notable percent change in PWS (314%) predicted for variation of k_1, we conclude that material and geometrical properties are potentially equally deterministic of PWS.

2.5.1 Study limitations

The conclusions drawn in this study should be considered along with some study limitations. Firstly, all simulations were performed under normotensive conditions, although some AAA patients often also present hypertension. Clearly the application of higher values of pressure in our model (to simulate a hypertensive state) would result in different (higher) peak wall stress [96]. However, we specifically want to draw attention to cases where clinically-determined geometric parameters, most notably the maximal AAA diameter, are beneath established thresholds for intervention but wall stress is elevated beyond a critical limit. We believe this analysis is more relevant under normotensive conditions where the impetus for surgical intervention is nominally lower, motivating our selection of the applied pressure boundary condition. Secondly, our simulations were carried out in the framework of classical continuum solid mechanics, and therefore ignore the potential for flow-induced shear stress on the inner vessel surface to impact AAA rupture risk, as pursued in previous studies [58,60,61,75,81,97]. Thirdly, the ultimate strength of vascular tissue is patient-specific and would vary with age and disease states, wherein our analyses assumed a single, representative ultimate strength of 1 MPa based on the range of values found in the literature [74]. Finally, the ranges of geometries and material properties explored in our study are based on idealized scenarios rather than patient-specific characteristics, which limits the translational significance of our findings. However, rather than evaluating actual clinical scenarios, the aim of this study is to identify general (idealized) determinants of PWS that can be introduced into risk evaluation irrespective of patient-to-patient differences.

2.5.2 Conclusion

The predicted interactive effects of sac diameter with thickness, axial extent, and material parameter k_1 accentuate the need for integration of additional risk factors into clinical decision making. Even with the few potential interactions considered in this study, it is evident that PWS values above the ultimate tissue strength are readily attainable in the sub-critical diameter range (< 5.0 cm). Taken together, our findings encourage an expansion of AAA parameters considered for clinical risk assessment and decision making and demonstrate the potential for computational modeling to further elucidate key factors governing AAA mechanics.

2.6 ACKNOWLEDGEMENTS

This research was supported by the NIH INBRE Grant for South Carolina (P20GM103499) and (R01HL133662).

Table 2.1: Geometric parameter values for the baseline AAA (underlined) and associated parametric studies.

Axial extent [mm]	Circumferential extent [°]	Diameter[1] [mm]	Location on Z-axis[2] [mm]	Thickness [mm]	Tortuosity XZ-plane	Tortuosity YZ-plane
48	90	35	<u>32</u>	0.75	-1.175	-1.175
<u>64</u>*	180	40	48	1.00	-1.05	-1.05
80	270	<u>45</u>	64	1.25	<u>1.00</u>	<u>1.00</u>
96	<u>360</u>	50		<u>1.50</u>	+1.05	+1.05
		55		1.75	+1.175	+1.175
		60		2.00		
		65				
		70				

[1] Maximum transverse diameter

[2] Distance from the bottom-most-cross-section (CS0) to the midway plane of aneurysmal sac in positive Z-direction

* Values underlined are geometrical input parameters defining the baseline AAA

Table 2.2: Mechanical properties for referent normal aortic tissue.

μ [MPa]	k_1 [MPa]	k_2	φ [°]
0.007	2.87	17.26	36.0

Table 2.3. Mechanical property values for the baseline AAA (underlined) and associated parametric studies.

μ [MPa]	k_1 [MPa]	k_2	φ [°]
0.001	1.00	0.001	45.0*
0.004	1.50	1	
0.009	2.00	30	
<u>0.013</u>**	<u>2.74</u>	70	
0.017	6.00	<u>119.6</u>	
0.040	15.00	350	
0.085	50.00	500	
0.100			

* Fiber angle of 45.0° was applied to all aneurysmal models

** Values underlined are material input parameters defining the baseline AAA case

Table 2.4. Sensitivity of PWS to geometrical and mechanical parameters characterizing AAA.

Parameter	Referent normal	Baseline AA	Range of input parameter	Percentage change in PWS[3]
μ [MPa]	0.007	0.013	[0.001,0.1]	22.0%
k_1 [MPa]	2.87	2.74	[1,50]	314%
k_2	17.26	119	[0.001,500]	156%
Axial extent [mm]	N/A	64	[48,96]	172%
Circumferential extent [°]	N/A	360	[90,360]	88.1%
Diameter[1] [mm]	20	45	[35,70]	231%
Location on Z-axis[2] [mm]	N/A	32	[32,64]	9.06%
Thickness [mm]	2.0	1.50	[0.75,2.00]	457%
Tortuosity XZ-plane	1	1	[-1.175,1.175]	62.1%
Tortuosity YZ-plane	1	1	[-1.175,1.175]	112%

[1] Maximum transverse diameter

[2] Distance from the bottom-most cross-section (CS0) to the midway plane of aneurysmal sac in positive Z-direction

[3] Maximum percentage change over examined range with respect to baseline AAA value

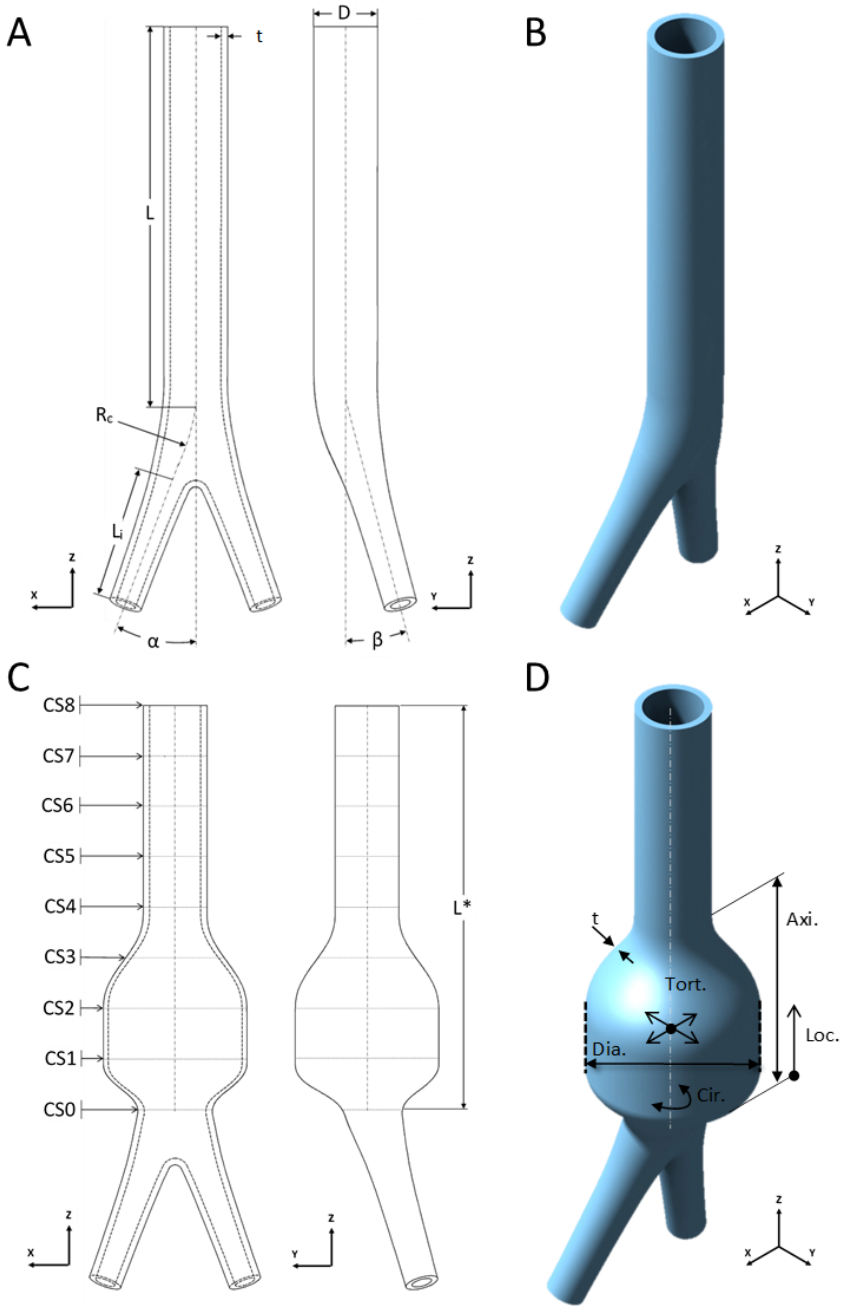

Figure 2.1: Referent normal aortic and baseline AAA geometries.
(A) Referent normal aortic geometry in XZ- and YZ-planes; L is the length of abdominal aorta, D is the outer diameter, t is the thickness, Rc is the radius of curvature, Li is the length of common iliac arteries, α and β are the take-off angle of the iliac arteries at the bifurcation and the angle between the abdominal aorta centerline and the plane formed by both iliac arteries, respectively. (B) An isometric view of the referent normal aortic geometry. (C) Baseline AAA geometry in XZ- and YZ-planes; L* is the length of geometrical variations field, CS0-8 are cross-sectional planes formed by dividing field of geometrical variations into eight sections longitudinally. (D) An isometric view of baseline

AAA geometry and depiction of geometrical input variables; t is the thickness within the aneurysmal sac, Dia. is the maximum transverse outer diameter of the aneurysmal sac, Cir. depicts the circumferential extent of the aneurysmal sac, Tort. indicates the tortuosity in XZ and YZ-planes, Axi. and Loc. are the axial extent and the longitudinal location of aneurysmal sac, respectively.

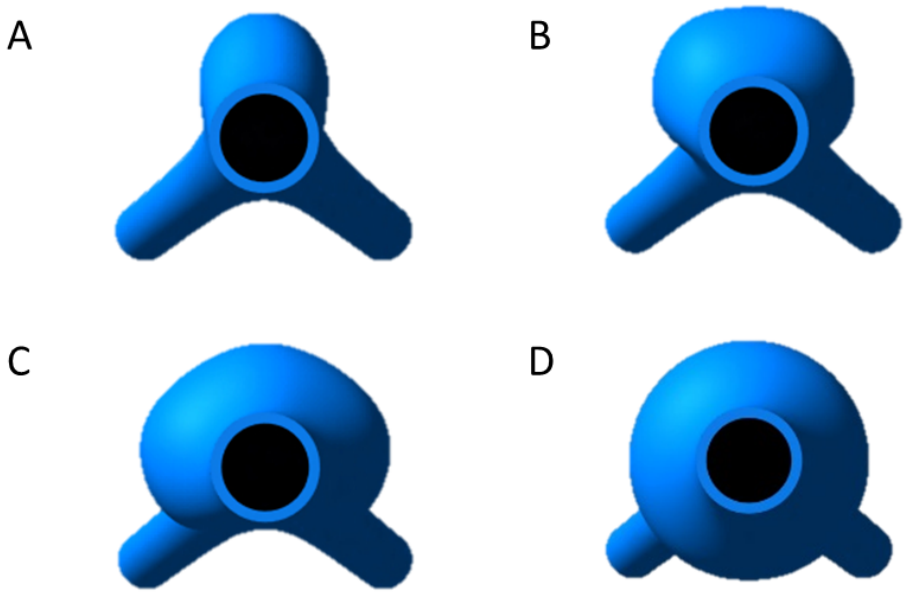

Figure 2.2: Circumferential (angular) extent of AAA bulging.
Top views of a (A) 90° (B) 180°, (C) 270° sweep and (D) 360° sweep on anterior face of aneurysmal sac.

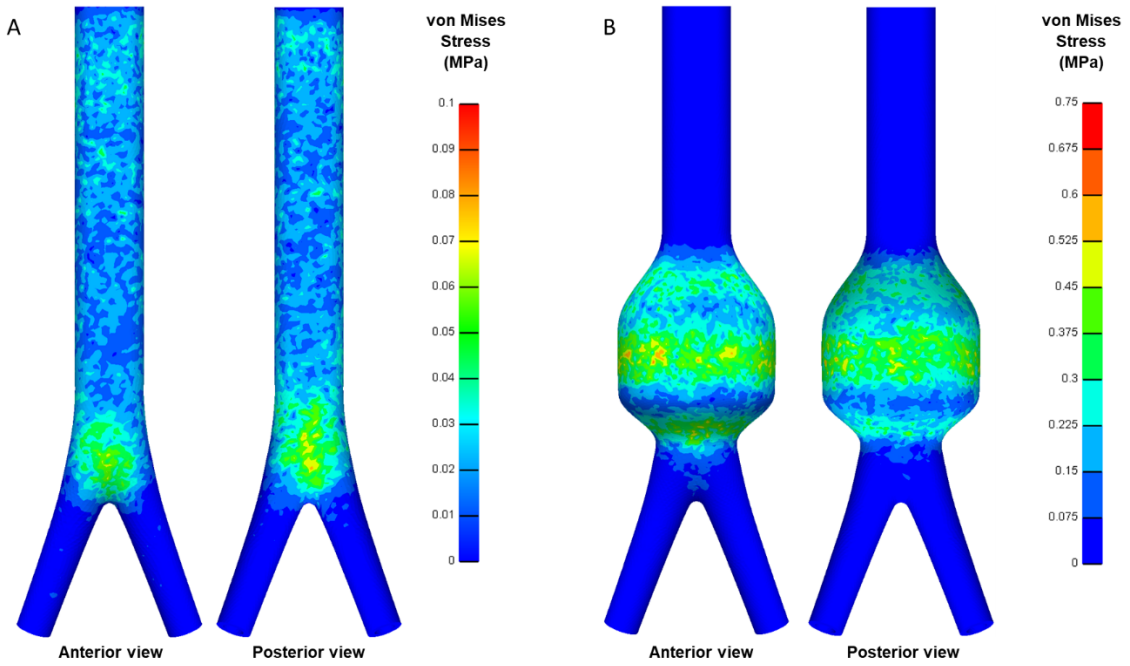

Figure 2.3: Predicted von Mises wall stress.
Computed von Mises wall stress distributions for (A) referent normal aorta and (B) baseline AAA simulations. (For interpretation of the references to color in this figure legend, the reader is referred to the Web version of this article.)

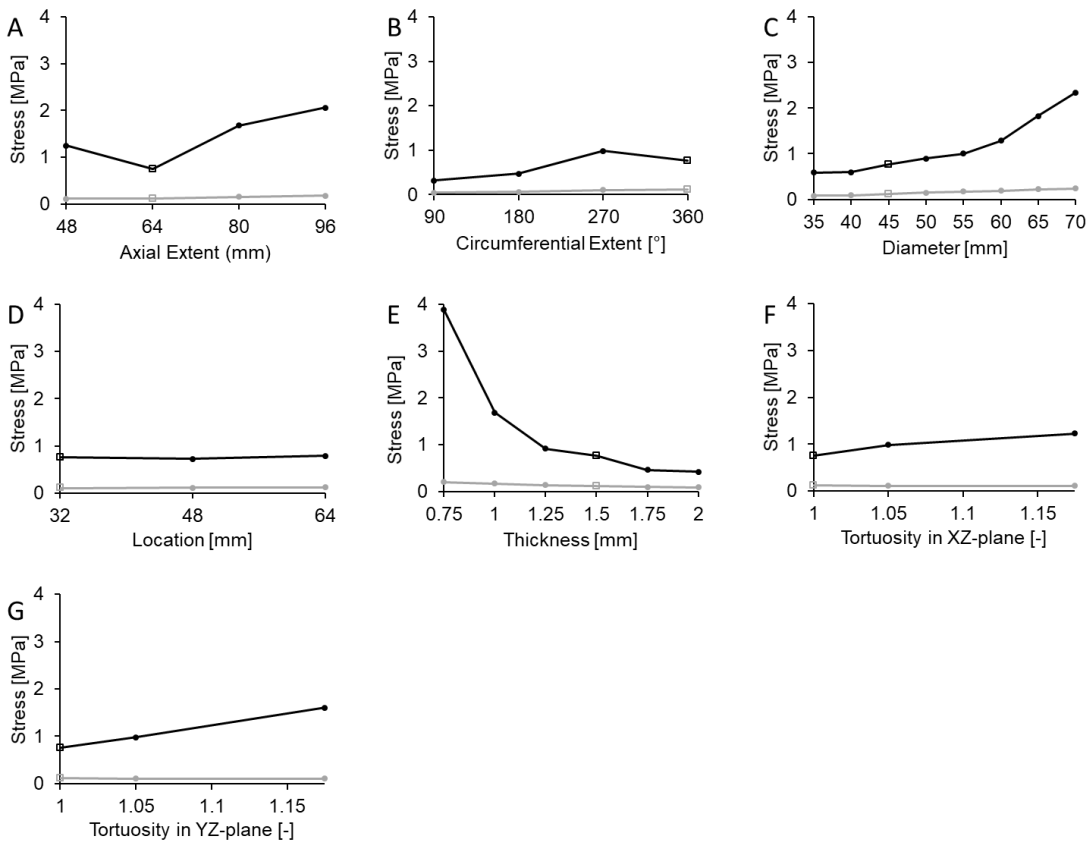

Figure 2.4: Effects of AAA geometrical properties.
PWS (black) and AWS (grey) are computed over isolated variations of defined AAA geometrical properties, including (A) axial extent, (B) circumferential extent, (C) maximum sac diameter, (D) sac location, (E) wall thickness, (F) tortuosity in XZ plane, and (G) tortuosity in YZ plane. In all cases, hollow square markers indicate the baseline AAA values.

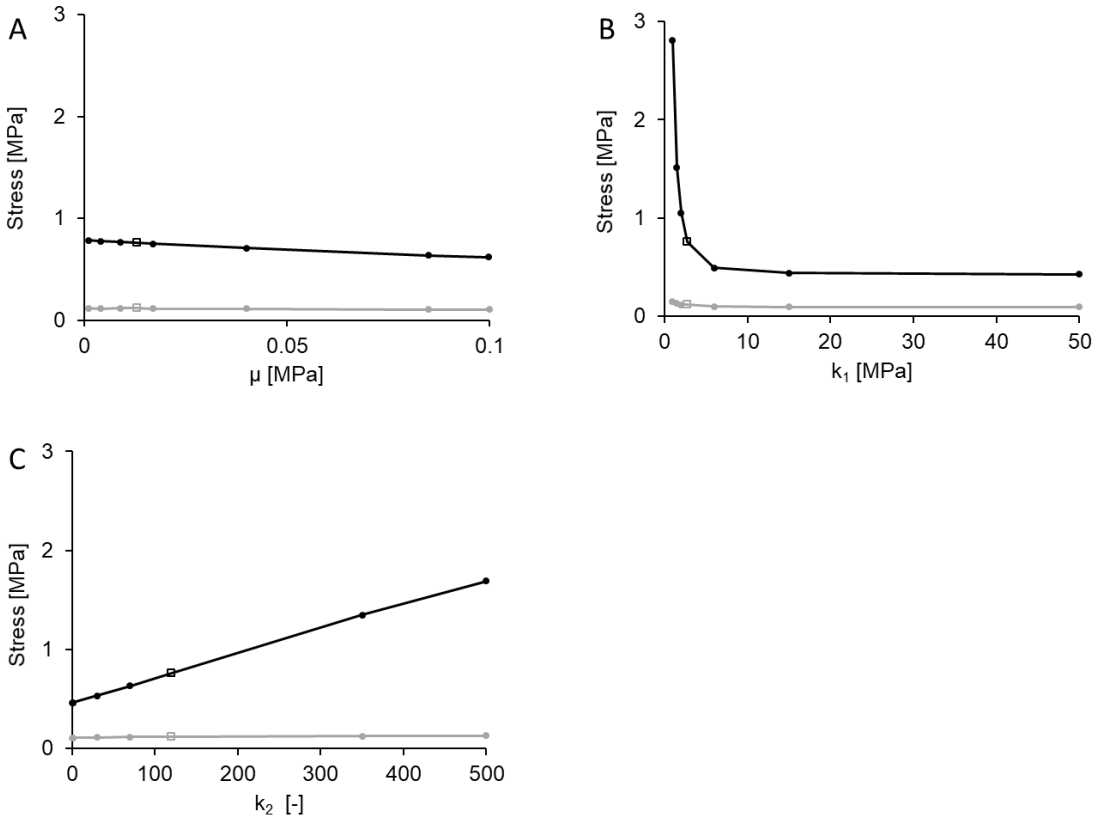

Figure 2.5: Effects of AAA mechanical properties.
PWS (black) and AWS (grey) are computed over isolated variations of defined AAA mechanical properties, including (A) μ, (B) k_1, and (C) k_2. In all cases, hollow square markers indicate the baseline AAA values.

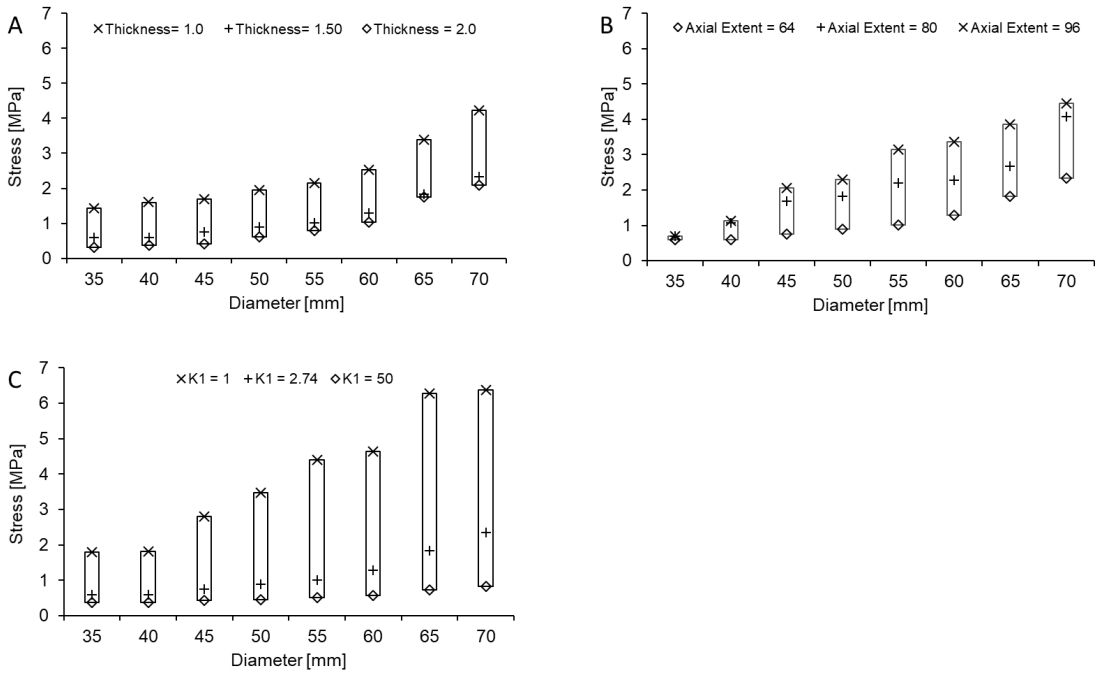

Figure 2.6: Interactive effects of geometrical and mechanical properties.
PWS as a function of sac diameter and prescribed levels of (A) wall thickness, (B) axial extent, and (C) K_1. The size of bars containing data points at a given diameter reflect the sensitivity of PWS to each parameter.

CHAPTER 3

GEOMETRIC DETERMINANTS OF LOCAL HEMODYNAMICS IN SEVERE CAROTID ARTERY STENOSIS[2]

[2] Azar D., Torres W. M., Davis L. A., Shaw T., Eberth J. F., Kolachalama V. B., Lessner S. M., Shazly T. 2019. Geometric determinants of local hemodynamics in severe carotid artery stenosis. Elsevier - *Computers in Biology and Medicine*. 114:103436. DOI: https://doi.org /10.1016/j.compbiomed.2019.103436

3.1 ABSTRACT

In cases of severe carotid artery stenosis (CAS), carotid endarterectomy (CEA) is performed to recover lumen patency and alleviate stroke risk. Under current guidelines, the decision to surgically intervene relies primarily on the percent loss of native arterial lumen diameter within the stenotic region (i.e. the degree of stenosis). An underlying premise is that the degree of stenosis modulates flow-induced wall shear stress elevations at the lesion site, and thus indicates plaque rupture potential and stroke risk. Here, we conduct a retrospective study on pre-CEA computed tomography angiography (CTA) images from 50 patients with severe internal CAS (>60% stenosis) to better understand the influence of plaque and local vessel geometry on local hemodynamics, with geometrical descriptors that extend beyond the degree of stenosis. We first processed CTA images to define a set of multipoint geometric metrics characterizing the stenosed region, and next performed computational fluid dynamics simulations to quantify local wall shear stress and associated hemodynamic metrics. Correlation and regression analyses were used to relate obtained geometric and hemodynamic metrics, with inclusion of patient sub-classification based on the degree of stenosis. Our results suggest that in the context of severe CAS, prediction of shear stress-based metrics can be enhanced by consideration of readily available, multipoint geometric metrics in addition to the degree of stenosis.

3.2 INTRODUCTION

Carotid artery interventions, such as carotid endarterectomy (CEA) and carotid artery stenting, have been used for over half a century to reduce stroke risk in patients presenting with severe carotid artery stenosis (CAS). However, these interventions carry

an aggregate complication rate of 4.5%–7.0%, with potential negative outcomes including myocardial infarction, pulmonary embolism, and post-operative stroke [98–100]. Clinical observations and experimental studies have demonstrated the importance of plaque geometry on local hemodynamics and embolic potential, motivating consideration of the degree of vessel stenosis in clinical decision making [37,101–104]. Current guidelines for CEA from most major international bodies recommend intervention for neurologically symptomatic CAS with ≥ 70% diameter reduction in the internal carotid artery (ICA), while others use a threshold of ≥ 50% diameter reduction [16,105]. Clinical guidelines recommend that in these cases, surgery is performed within two weeks of the onset of neurological symptoms [106]. Existing guidelines for neurologically asymptomatic cases are less uniform, but clinical decision-making still depends mainly on the maximum degree of stenosis [16,106]. In addition to the degree of stenosis, higher fidelity geometric details of the atherosclerotic plaque and parent vessel are accessible via clinical imaging including computed tomography angiography (CTA), and have been shown to significantly impact the local blood flow field and plaque mechanics [24,107–109]. For instance, an increase in lesion axial length is inversely related to axial plaque stress in severely stenotic cases (≥60%), thus suggesting extended lesions have relatively diminished embolic potential [24]. Plaque asymmetry in the stenosed region has also been shown to impact local wall shear stress magnitudes and flow recirculation patterns [107,110]. Other studies have found correlation between vessel tortuosity and flow-dependent pressure gradients, with a co-dependence on the degree of stenosis [111]. In a study that examined both degree of stenosis and plaque eccentricity, these factors exhibited a strong interactive effect on the wall shear stress distribution [112]. In these and other studies, finite element-based computational fluid

dynamics (CFD) models were used to interrelate plaque geometry and local hemodynamics [23,37,113,114].

Clinical integration of CFD models requires a noninvasive, image-based assessment of plaque and vessel geometry and estimation of inlet/outlet blood velocities/pressures in a control volume encompassing the diseased vasculature. CFD solutions provide three-dimensional transient velocity/pressure fields and enable quantification of multiple hemodynamic metrics. These metrics include: flow-induced wall shear stress (WSS) – the tangential friction force on the endothelial or plaque surface; oscillatory shear index (OSI) – the temporal fluctuation of the WSS; and relative residence time (RRT) – the relative dynamic measure of local nonadherent particles within the flow field. These metrics have been linked to plaque accumulation, remodeling, and rupture risk [10,115].

The goal of the present study was to process pre-CEA CTA images to define and quantify multipoint descriptors of lesion geometry, and then build CFD models to compute hemodynamic metrics at the lesion site. Our hypothesis is that multiple metrics of lesion geometry, including but not limited to the degree of stenosis, will interactively modulate local hemodynamics in stenotic carotid arteries.

3.3 METHODS

3.3.1 Patient-specific data acquisition

Fifty de-identified CTA images in DICOM format were obtained from patients with highly stenotic ICAs evaluated for CEA (Greenville Health System, Greenville, SC). According to the North American Symptomatic Carotid Endarterectomy Trial (NASCET) criteria, all cases were at a high risk of stroke with the degree of stenosis ranging from

67.4% to 99.1%. Handling and processing of patient images were performed in accordance with institutional ethics committee guidelines. All patients gave informed consent for use of their clinical imaging studies under IRB protocol (Pro00027940).

3.3.2 Geometry reconstruction and analysis

3.3.2.1 Reconstruction of patient-specific geometries

A semi-automated approach was developed to efficiently reconstruct the 3D arterial lumen and identify patient-specific geometric variables of the plaque and local vasculature (elaborated upon in subsequent sections). This semi-automated process yielded reproducible assessments independent of operator variability while minimizing time and resource consumption. The CTA volume is represented in a series of 2D images with a known distance between each image. A segmentation protocol was established using the Vascular Modeling Toolkit (VMTK; www.vmtk.org), an open-source pre-processing resource, to identify the boundaries of the arterial lumen for each slice of the scan using the distinct density-dependent voxel intensities between the angiography contrast dye and the plaque/arterial wall. The underlying algorithm in this automated process is based on an identification of centerlines and a robust decomposition of the bifurcation into its constituent branches, followed by mapping the surface of each of the branches onto the parametric plane [116]. After manual selection of a seed point and definition of bounds, the boundaries of the arterial lumen were detected and smoothing algorithms were applied to remove fine-scale irregularities from the reconstructed surface. Finally, a non-uniform rational b-spline was then fit to the surface to facilitate domain discretization for CFD analysis (Figure 3.1A).

Reconstructed domains were imported into the ANSYS ICEM-CFD meshing software and fit with a linear tetrahedral surface mesh using a robust octree formulation [117–119]. After smoothing this mesh to increase the quality of the individual elements, a tetrahedral volume mesh was generated using a Delauney formulation [110,114]. Finally, the arterial wall was fit with a triple layer of post-inflation hexahedral prism elements to allow for a more accurate capture of the hemodynamics in the boundary layer.

3.3.2.2 Calculation of geometric variables

A MATLAB code was developed to extract the centerline along the vessel geometry and the cross-sectional area function (*A(x)*) at every point along the centerline path [116]. *A(x)* was computed based on normal cross-sections of maximal inscribed spheres along the centerline. Geometric variables (described below) were calculated from *A(x)* center-point coordinates and the associated function value. The region of interest (ROI) for geometric variable calculation was a 5 mm radius sphere with a center point coincident with the maximal degree of stenosis (S_{max}) (Figure 3.1B). The employed ROI sphere radius (5 mm) was motivated by typical lesion length (along the centerline) across the entire study cohort. Shear stress and related metrics (discussed in below sections) were temporally- and spatially-averaged within the ROI to minimize response variable sensitivity to model discretization.

A set of nine geometric variables were extracted from the reconstructed geometries to describe the complex geometry of the ROI. Degree of stenosis, *S*, is the ratio between the minimal lumen area within the ROI and the proximal lumen area of the non-diseased section of the common carotid artery. For subsequent analyses, cases were subclassified based on the degree of stenosis ($0.67 < S < 0.80$, $0.80 \leq S < 0.90$ and $0.90 \leq S < 1.00$; where

$S\times100$ corresponds to the percentage of stenosis). Proximal tortuosity, τ_P, and distal tortuosity, τ_D, are the ratios of the centerline path length divided by the point-to-point distances from S_{max} to the proximal and distal ends of the ROI, respectively. Proximal luminal concavity, C_P, and distal luminal concavity, C_D, are the absolute values of the second derivative of *A(x)* with respect to proximal/distal locations *(x)*. *A(x)* is a quadratic function that returns the lumen area at the position *x* defined with respect to the location of S_{max}. Proximal area-averaged slope, $\bar{m}_P$, and distal area-averaged slope, $\bar{m}_D$, are the integrals of the first derivative of *A(x)* with respect to distance divided by the area function in either proximal and distal sides of the S_{max}, respectively. Stenosis-to-proximal-end slope m_P, and distal-end-to-stenosis slope, m_D, are the absolute values of the change in lumen area over end-to-end distance (Table 3.1).

3.3.3 CFD model construction

CFD models were developed with a finite volume-based Navier- Stokes solver (ANSYS-Fluent v. 17.2), and each model was run over three cardiac cycles under an assumption of laminar flow [120,121]. The results presented here refer to averages obtained over the third cardiac cycle in order to minimize the influence of initial flow conditions. The blood was characterized as an incompressible non-Newtonian Carreau fluid (η_0=0.25 Pa·s; η_∞=0.0035 Pa·s; λ=25; n=0.25) with a constant density of 1060 kg/m^3 and zero-slip boundary conditions were applied to the rigid arterial walls [121]. A previously acquired carotid artery velocity profile attained from a healthy human male subject was converted to a continuous function using a Fourier transform and then used as an inlet velocity boundary condition on the proximal segment of the common carotid artery (CCA) [122–125]. A fully developed velocity profile was established within 2 cm downstream of the inlet

across all cases. In accordance with prior studies on highly stenoses carotid arteries, uniform pressures of 70 mmHg and 90 mmHg were prescribed to the internal and external carotid artery outlets, respectively [126]. A mesh-independent solution was identified in a subset of cases (5) as the lowest mesh density for which subsequently increasing density (>30% increase in total number of elements) did not significantly alter the computed peak WSS value (<1% change). Based on these studies, a minimum of 100,000 elements spanning the 8 cm length of the reconstructed carotid bifurcation was used in all models.

3.3.4 Post-processing

3.3.4.1 Hemodynamic response variables

To calculate time-averaged wall shear stress (TAWSS), the instantaneous WSS was calculated and then averaged spatially/temporally across all elements in the ROI over the third cardiac cycle:

$$\text{TAWSS} = \frac{1}{T}\int_0^T |WSS|\, dt \qquad (3.1)$$

Mean oscillatory shear index (OSI) is a dimensionless parameter ranging from 0 to 0.5 that is defined based on the temporal fluctuation of WSS and averaged over the ROI, as:

$$\text{OSI} = 0.5\left[1 - \frac{\left|\int_0^T WSS\, dt\right|}{\int_0^T |WSS|\, dt}\right] \qquad (3.2)$$

where T is the elapsed time and WSS is the magnitude at each individual node. Mean relative residence time (RRT) considers both the averaged WSS and mean OSI:

$$\text{RRT} = \frac{1}{\text{TAWSS}(1-2\ \text{OSI})} = \frac{1}{\left|\int_0^T WSS\, dt\right|} \qquad (3.3)$$

with values reported in Pa^{-1}. RRT reflects the residence time of blood in contact with or near the endothelium and is considered an important factor in plaque genesis [121].

3.3.4.2 Statistical analyses

Data were analyzed using MATLAB to identify correlations between geometric and hemodynamic variables, with Spearman correlation used to quantify correlation strength and significance. Correlation analyses were carried for all cases together (general approach) or a piecewise approach that was based on a sub-classification of cases via degree of stenosis ($0.67 < S < 0.80$, $0.80 \leq S < 0.90$ and $0.90 \leq S < 1.00$). Geometrical variables with statistically significant correlation to a given CFD hemodynamic variable were then used to develop predictive regression models that consider the former as input and the latter as output. Backward stepwise multiple linear regression was performed for model parameter identification, with inclusion of variable interactions only if model R^2 was increased by > 0.05 due to the inclusion. Regression models were developed based on either the entire sample set (general regression) or over the defined sub-classification ranges (piecewise regression). Of the 50 CTA images, 45 were used for regression model parameter identification, and 5 were reserved for evaluating the predictive capability of the regression models by comparing predicted values of hemodynamic response variables against obtained CFD results.

3.4 RESULTS

CTA-based vessel geometric models were used to extract geometric variables (9 per case) using the aforementioned semi-automated approach. Geometric models were also used in CFD simulations that compute local hemodynamic response variables derived from WSS (3 per case). Descriptive statistics for geometrical variables and CFD-based hemodynamic variables are shown in Figure 3.2. Three representative cases from each sub-

classifications of the degree of stenosis are shown along with the distribution of hemodynamic variables relative to the degree of stenosis (Figure 3.3)

3.4.1 Simulation results and correlation: TAWSS

Computational simulations qualitatively show an increase in TAWSS magnitudes with increasing degree of stenosis, with clearly nonuniform stress distributions both proximal and distal to the bifurcation point (Figure 3.3A). Within these cases of severe CAS, TAWSS was generally elevated with increasing degree of stenosis. However, an exponential regression model was statistically insignificant when applied across all cases ($R^2 = 0.52$; $p = 0.14$), motivating consideration of additional geometric variables to predict shear stress and related metrics. When sub-classified based on the degree of stenosis, TAWSS is relatively more sensitive to increased stenosis in the severe cases ($0.90 \leq S < 1.00$); with averaged values of 17.81 ± 16.05 Pa, 29.74 ± 15.95 Pa and 118.72 ± 117.71 Pa for $0.67 < S < 0.80$, $0.80 \leq S < 0.90$ and $0.90 \leq S < 1.00$, respectively (Figure 3.3A). While a general correlation analysis revealed a positive correlation between TAWSS and the degree of stenosis, as well as both proximal and distal area-averaged slopes, the significance of these factors was not fully maintained throughout piecewise correlation analysis (Figure 3.4). Most notably, no correlation between TAWSS and the degree of stenosis was observed in the intermediate stenosis subclassification ($0.80 \leq S < 0.90$).

3.4.2 Simulation results and correlation: OSI and RRT

Representative colorimetric plots of OSI and RRT underscore the inherent relation between these flow field metrics, with obvious coincidence of vessel regions experiencing locally elevated values (Figure 3.3B and C). There was no general correlation ($p<0.15$) between the area-averaged mean OSI and the degree of stenosis, and only sporadic

correlation when sub-classifications were considered (Figure 3.4). Using the general correlation analysis, no statistically significant relationship was found between OSI and any of the defined geometric variables. For the OSI piecewise correlation analyses, there is at least one geometric variable with stronger correlation as compared to degree of stenosis in each subclassification range. Area-averaged mean RRT exhibits a consistent negative correlation to the degree of stenosis, with the strongest relation in the least stenosed vessels ($0.67 < S < 0.80$) (Figure 3.4).

3.4.3 Regression models

Multiple linear regression models were generated using the defined geometric variables that correlated with CFD hemodynamic variables ($p<0.1$), as well as potential interactive effects among these geometric variables. For each of the hemodynamic variables, the following general and piecewise regression models were obtained:

<u>TWASS</u>

General:

$$Mean\ TAWSS\ [\text{Pa}] =$$

$$261.44 - 274.7 \times S - 488.04 \times \overline{m}_D + 564.64 \times S \times \overline{m}_D, \qquad p < 0.001$$

Piecewise:

$$Mean\ TAWSS\ [\text{Pa}] =$$

$$\begin{cases} 17.94 - 3.47 \times \overline{m}_D - 19.30 \times m_D + 20.58 \times \overline{m}_D \times m_D & 0.67 < S < 0.80, p = 0.075 \\ 8.8104 + 17.278 \times \overline{m}_P & 0.80 \leq S < 0.90, p = 0.035 \\ -1754.8 + 1856.9 \times S + 49.77 \times \overline{m}_D & 0.90 \leq S < 1.00, p = 0.002 \end{cases}$$

<u>OSI</u>

General: ----

Piecewise:

$$Mean\ OSI\ [-] =$$

$$\begin{cases} 0.009 + 0.017 \times C_D & 0.67 < S < 0.80,\ \ p = 0.066 \\ 0.07 - 0.04 \times \overline{m}_D - 0.02 \times m_D - 0.01\, m_D \times \overline{m}_D & 0.80 \le S < 0.90,\ \ p = 0.001 \\ -0.24 + 0.28 \times S + 0.16 \times\ \overline{m}_P - 0.01 \times \overline{m}_D - 0.18\, S \times \overline{m}_P + 0.01 \times\ \overline{m}_P \times \overline{m}_D & \\ & 0.90 \le S < 1.00,\ \ p = 0.010 \end{cases}$$

RRT

General:

$$Mean\ RRT\ [\mathrm{Pa}^{-1}] =$$

$$\begin{aligned} 0.355 - 0.1437 \times S + 0.609 \times C_D - 0.504 \times \overline{m}_D + 0.265 \times m_P - 0.63 \times S \times C_D \\ + 0.493 \times S \times \overline{m}_D - 0.341 \times S \times m_P - 0.068 \times C_D \times \overline{m}_D \\ + 0.0566 \times C_D \times m_P + 0.0184 \times \overline{m}_D \times m_P \qquad p < 0.001 \end{aligned}$$

Piecewise:

$$Mean\ RRT\ [\mathrm{Pa}^{-1}] =$$

$$\begin{cases} 9.82 - 10.6 \times S - 10.92 \times C_P - 0.44 \times \overline{m}_P + 12.41 \times C_P \times \overline{m}_P & \\ & 0.67 < S < 0.80,\ \ p = 0.011 \\ -3.93 + 4.64 \times S + 4.67 \times C_D + 1 \times m_P - 5.31 \times S \times C_D - 1.14\ \times S \times m_P & \\ & 0.80 \le S < 0.90,\ \ p < 0.001 \\ 1.11 + 1.20 \times S + 1.06 \times m_P - 1.10 \times S \times m_P & 0.90 \le S < 1.00,\ \ p = 0.018 \end{cases}$$

The descriptive and predictive capabilities of identified regression models were evaluated by comparing model- and CFD-derived values of hemodynamic response variables (Figure 3.5). While no significant general regression model was obtained for OSI, piecewise regression resulted in significant descriptive and predictive models (Figure 3.5B). Piecewise as opposed to general regression modeling resulted in a substantial

improvement in both the descriptive and predictive capabilities with respect to TAWSS and RRT (Figures 3.5A and C).

3.5 DISCUSSION

The present study involves presurgical CTA scans from 50 patients with sufficient carotid artery stenosis to meet the current NASCET guidelines for the recommendation of surgical intervention (i.e. carotid endarterectomy). These guidelines, although the current gold standard for surgical decision making, inherently rely on one geometric parameter determined at one axial plaque location [127]. Several experimental and computational studies have elucidated the importance of other geometrical attributes of the plaque on flow-induced wall shear stress, flow reversal and stenosis progression [24,107,128]. To that end, the primary goal of this study was to identify a set of novel local geometric variables that can collectively predict local wall shear stress and related hemodynamic indicators of risk in highly stenotic carotid arteries. Although risk assessment in CAS is highly multifactorial, this work focuses on predicting local shear stress levels based on patient-specific geometry.

Regions with complex geometries are susceptible to focal complications arising from low WSS, exemplified by the prevalence of carotid atheroma in the vicinity of the carotid bifurcation [129,130]. Conversely, moderately elevated WSS (~30 Pa) can promote the formation of lumen thrombus and severely elevated WSS (over 40 Pa) can cause local endothelial injury and denudation [131]. Several previous studies have examined trends in the TAWSS in severely stenotic cases; Li et al. reported TAWSS as high as 73 Pa located distal to the point of maximal stenosis in a patient-specific model [120]. A similar observation was made by Su et al., noting elevated TAWSS (79 Pa) with 90% stenosis, compared to baseline values that were less than 12 Pa [132]. As reported in the literature and observed this study,

stenosis generally elevates TAWSS but does so in a complex manner that is suggestive of interactive effects with other geometric characteristics [24,128].

Spatial and temporal fluctuations of the WSS vector are quantified by the mean OSI and RRT. Higher degrees of stenotic occlusion (>50-60%) are associated with a sharp increase of OSI and RRT [121]. It was shown previously that in an idealized geometry an increase in stenosis results in larger downstream vortices, and as a result higher magnitudes of OSI become more prominent farther from the maximum stenosis [121,128]. We observed a reduction in OSI local to the lesion which our results find to be independent of the local geometry [133,134]. OSI, however, does show a positive association with stenosis as occlusion progresses and demonstrates correlations with parameters other than stenosis at different stages of the pathology (i.e. three subcategories of stenotic severity). Furthermore, our qualitative examinations confirmed an increase of OSI distal and proximal to the lesion site, areas where flow reversal is predominant [133,135].

For RRT, it was shown that the degree of stenosis has a strong negative association with the RRT, regardless of what sample population was considered. Strong negative correlation between the degree of stenosis and the mean RRT in the ROI can be explained with the increased pressure gradient induced by the pathology that will result in lower residence time while WSS values are maximal [121,133]. An interesting outcome of this study is that all correlating proximal characteristics showed a positive relation with the RRT, and almost all distal parameters a negative relation. Among all geometric variables that demonstrated correlation within sub-classifications, the positive correlation between m_P and the mean RRT remained consistent and thus is strong candidate variable to predict RRT directly from CTA images.

3.5.1 Limitations

While our study incorporated a total of 50 cases and yielded multiple significant predictors of local hemodynamic variables, identified regression models may not be relevant to non-severe cases. In these models, vessel walls are assumed rigid; results might differ in models with deformable vessel walls and when fluid-structure interactions are accounted for. Furthermore, CFD models were built using patient-specific geometries, but representative flow field boundary conditions were applied uniformly across all cases. It is well acknowledged that the application of an inlet flow waveform acquired from a healthy patient diminishes the direct translational relevance of obtained results; however, uniform boundary conditions (among cases) were selected to facilitate isolation of geometric determinants of local wall shear stress. Additionally, all CFD models in this study were generated under the laminar flow assumption. While previous studies suggest a likely transition to turbulent flow in the case of highly stenotic carotid arteries, we only considered laminar flow [109,136–138]. Future iterations of our work will consider new segmentation methods in which flux-based higher order tensor is utilized for an improved modeling accuracy at branching points [139]. Finally, our computational models must be validated in future studies via comparing predictions to results acquired from four-dimensional flow magnetic resonance imaging (MRI) and reference CFD analysis results [140].

3.6 CONCLUSION

Our study is based on the definition and quantification of a novel set of local geometric variables which extended beyond the degree of stenosis. Computational results predict that key geometric variables, in addition to the degree of stenosis, significantly

modulate local wall shear stress (and related metrics) in the context of severe CAS. Moreover, piece-wise multiple linear regression modeling suggests that different sets of geometric variables (which include the degree of stenosis) are determinants of wall shear stress across case subclassifications based solely on the degree of stenosis. We expect that different sets of geometric determinants would manifest under lower degrees of stenosis, which could be identified in CFD-based analyses and potentially influence surgical decision making in the context of CEA.

3.7 ACKNOWLEDGEMENTS

This research was supported by the NIH INBRE Grant for South Carolina (P20GM103499), NSF Grant (CMMI-1760906) and the NIH/ NIBIB (1R03 EB019663).

Table 3.1: Definition of geometric variables with respective formulae.

Geometric variables	Definition
Degree of stenosis; S	$= 1 - \frac{\text{minimum } A(x)}{\text{maximum } A(x)}$
Proximal tortuosity; τ_P	$= \frac{\text{Length}}{\text{Distance}}$ between the vessel centerline at the proximal end of the region of interest and S_{max}
Distal tortuosity; τ_D	$= \frac{\text{Length}}{\text{Distance}}$ between the vessel centerline at the distal end of the region of interest and S_{max}
Proximal luminal concavity; C_P	$= \left\lvert \frac{d^2A}{dx^2_{Prox/Distal}} \right\rvert$, where A is a quadratic function of distance on proximal side; $A(x) = ax^2 + bx + c$.
Distal luminal concavity; C_D	$= \left\lvert \frac{d^2A}{dx^2_{Prox/Distal}} \right\rvert$, where A is a quadratic function of distance on distal side; $A(x) = ax^2 + bx + c$.
Proximal area-averaged slope; $\bar{m}_P$	$= \int_0^{x_{Prox/Distal}} \frac{\frac{dA}{dx_{Prox/Distal}}}{A} dx$, where A is a quadratic function of distance on proximal side; $A(x) = ax^2 + bx + c$.
Distal area-averaged slope; $\bar{m}_D$	$= \int_0^{x_{Prox/Distal}} \frac{\frac{dA}{dx_{Prox/Distal}}}{A} dx$, where A is a quadratic function of distance on distal side; $A(x) = ax^2 + bx + c$.
Stenosis-to-proximal-end slope; m_P	$= \left\lvert \frac{\Delta A}{\Delta X_{Prox/Distal}} \right\rvert$, where ΔA is the area change over length on proximal side of the region of interest.
Distal-end-to-stenosis slope; m_D	$= \left\lvert \frac{\Delta A}{\Delta X_{Prox/Distal}} \right\rvert$, where ΔA is the area change over length on distal side of the region of interest.

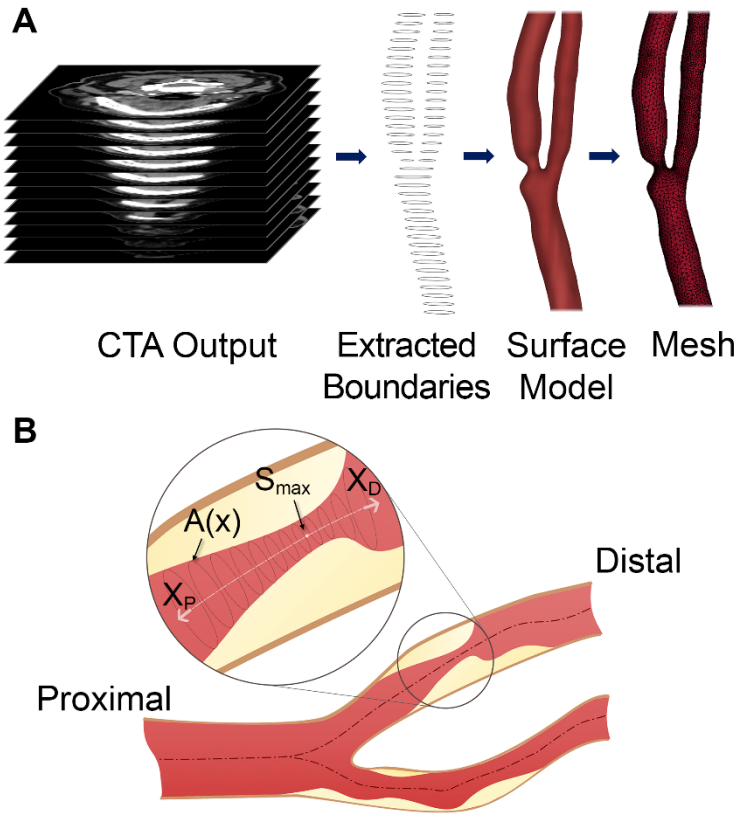

Figure 3.1: Carotid artery reconstruction and the 2D illustration of stenotic carotid artery.

(A) Carotid artery reconstruction steps; CTA imaging output shown by a stack of 2D images of a representative carotid artery segment, extracted boundaries to define the surface of the arterial lumen, surface model and the linear tetrahedral volumetric mesh. (B) The maximal stenosis S_{max} and cross-sectional area A(x) are depicted. X_D and X_P specific center-point locations in the distal and proximal directions, respectively.

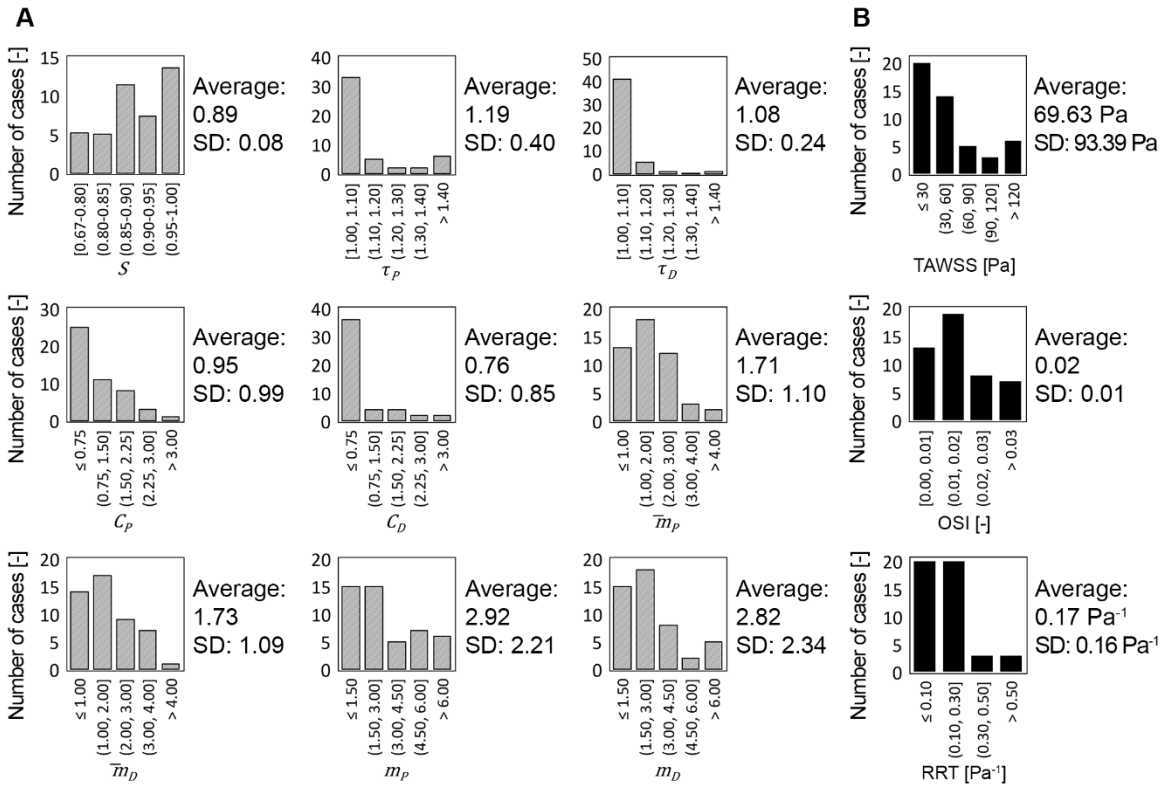

Figure 3.2: Descriptive statistics of CTA-based geometric variables and results obtained from CFD simulations.

(A) Each bar represents a range of values. The length of each bar denotes the frequency of each range for each of the geometric variables; Degree of Stenosis; S, Proximal Tortuosity; τ_P , Distal Tortuosity; τ_D , Proximal Luminal Concavity; C_P , Distal Luminal Concavity; C_D, Proximal Area-Averaged Slope; $\overline{m}_P$, Distal Area-Averaged Slope; $\overline{m}_D$, Stenosis-to-Proximal-end Slope; m_P and Distal-end-to-Stenosis Slope; m_D. (B) - output variables calculated from CFD simulations; TAWSS, OSI and RRT.

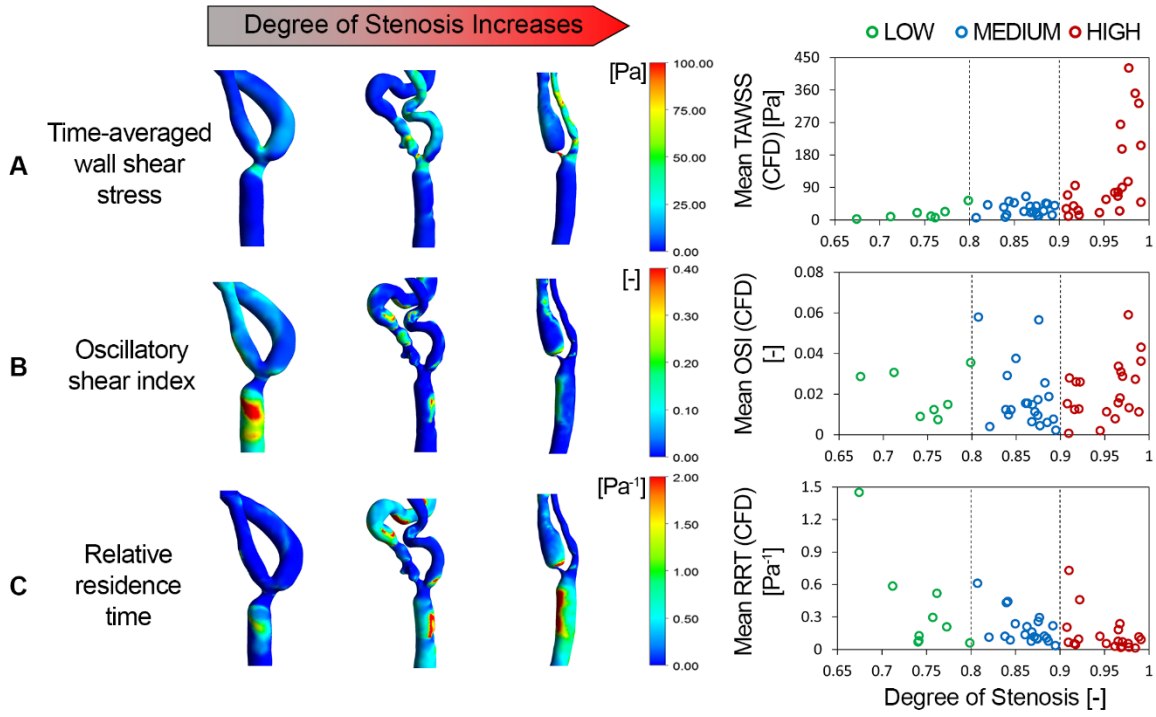

Figure 3.3: 3D mapping of CFD results for representative samples from each stenotic subclassification, and the distribution of hemodynamics vs. the degree of stenosis. 3D mapping of results from CFD simulations for a representative sample of reconstructed geometries selected from each of the three ranges of stenotic severity ($0.67 < S < 0.80$, $0.80 \leq S < 0.90$ and $0.90 \leq S < 1.00$) and the distribution of hemodynamic variables with respect to the degree of stenosis for all samples. Stenosis severity ranges from $0.67 < S < 1$ and datapoints are labeled with different colors indicating the severity category (Green: $0.67 < S < 0.80$, Blue: $0.80 \leq S < 0.90$ and Red: $0.90 \leq S < 1.00$). (A) 3D mapping of TAWSS for three representative cases and distribution of TAWSS with respect to degree of stenosis. (B) 3D mapping of OSI for three representative cases and distribution of OSI with respect to degree of stenosis. (C) 3D mapping of RRT for three representative cases and distribution of RRT with respect to degree of stenosis. (For interpretation of the references to color in this figure legend, the reader is referred to the Web version of this article.)

A

All		Mean TAWSS [Pa]	Mean OSI [-]	Mean RRT [Pa^{-1}]
Geometrical Variables	*Degree of* Stenosis; S	0.67**	0.16	-0.57**
	Proximal Tortuosity; τ_P	-0.05	0.16	0.07
	Distal Tortuosity; τ_D	0.16	0.08	-0.36
	Proximal Luminal Concavity; C_P	-0.14	0.09	0.31
	Distal Luminal Concavity; C_D	-0.09	0.26	0.25*
	Proximal Area-Averaged Slope; $\overline{m}_P$	0.44**	0.22	-0.23
	Distal Area-Averaged Slope; $\overline{m}_D$	0.56**	0.04	-0.42**
	Stenosis-to-Proximal-end Slope; m_P	-0.09	0.08	0.24*
	Distal-end-to-Stenosis Slope; m_D	0.00	-0.08	-0.07

B

0.67 < S < 0.80		Mean TAWSS [Pa]	Mean OSI [-]	Mean RRT [Pa^{-1}]
Geometrical Variables	*Degree of* Stenosis; S	0.75*	-0.04	-0.75*
	Proximal Tortuosity; τ_P	-0.43	0.39	0.43
	Distal Tortuosity; τ_D	-0.46	-0.11	0.29
	Proximal Luminal Concavity; C_P	-0.53	-0.11	0.86**
	Distal Luminal Concavity; C_D	0.14	0.82**	-0.20
	Proximal Area-Averaged Slope; $\overline{m}_P$	-0.55	0.11	0.79**
	Distal Area-Averaged Slope; $\overline{m}_D$	0.82**	0.46	-0.68*
	Stenosis-to-Proximal-end Slope; m_P	-0.61	-0.25	0.82**
	Distal-end-to-Stenosis Slope; m_D	0.79**	0.39	-0.50

C

0.80 ≤ S < 0.90		Mean TAWSS [Pa]	Mean OSI [-]	Mean RRT [Pa^{-1}]
Geometrical Variables	*Degree of* Stenosis; S	0.07	-0.26	-0.37*
	Proximal Tortuosity; τ_P	0.00	0.28	-0.01
	Distal Tortuosity; τ_D	-0.09	-0.12	-0.35
	Proximal Luminal Concavity; C_P	0.43	0.04	0.07
	Distal Luminal Concavity; C_D	-0.40	0.20	0.41*
	Proximal Area-Averaged Slope; $\overline{m}_P$	0.65**	0.05	0.17
	Distal Area-Averaged Slope; $\overline{m}_D$	0.11	-0.45**	-0.27
	Stenosis-to-Proximal-end Slope; m_P	0.03	0.10	0.42*
	Distal-end-to-Stenosis Slope; m_D	0.04	-0.41*	-0.26

D

0.90 ≤ S < 1.00		Mean TAWSS [Pa]	Mean OSI [-]	Mean RRT [Pa^{-1}]
Geometrical Variables	*Degree of* Stenosis; S	0.65**	0.46**	-0.35*
	Proximal Tortuosity; τ_P	-0.27	-0.12	0.27
	Distal Tortuosity; τ_D	0.24	0.23	-0.29
	Proximal Luminal Concavity; C_P	-0.09	0.19	0.45**
	Distal Luminal Concavity; C_D	-0.26	-0.04	0.22
	Proximal Area-Averaged Slope; $\overline{m}_P$	0.36	0.41*	-0.13
	Distal Area-Averaged Slope; $\overline{m}_D$	0.61**	0.47**	-0.23
	Stenosis-to-Proximal-end Slope; m_P	-0.37	0.18	0.39*
	Distal-end-to-Stenosis Slope; m_D	-0.34	0.13	0.32

Figure 3.4: Spearman correlation analysis results for ρ demonstrating the strength of the association between hemodynamic and geometric variables.
(A) Spearman correlation coefficient and statistical significance assessment using the general approach and including all samples. (B-D) – using the piecewise approach with $0.67 < S < 0.80$, $0.80 \leq S < 0.90$ and $0.90 \leq S < 1.00$, respectively. $\rho>0$ and $\rho<0$ values are shaded with shades of red and blue, respectively. darker shades indicate greater magnitudes of ρ values. (* indicates p-value<0.1 and ** indicates p-value<0.05). (For interpretation of the references to color in this figure legend, the reader is referred to the Web version of this article.)

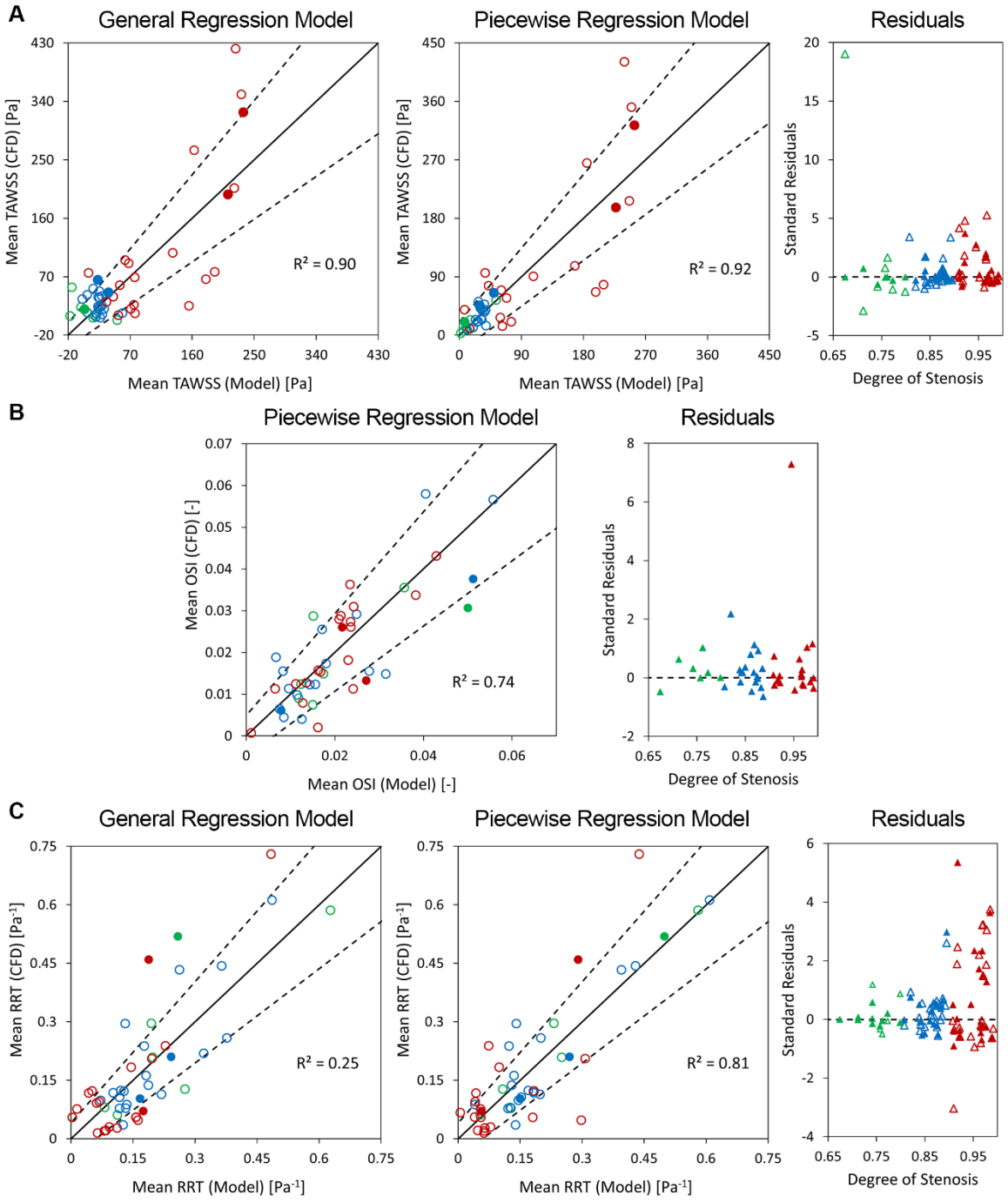

Figure 3.5: Relationship between hemodynamic variables obtained from CFD results with respect to the regression models and respective residuals.
(A) Distribution of the TAWSS from CFD and regression models (general and piecewise) obtained using 45 cases. Filled data points show values predicted by the model that were not used in development of the model (5 cases). (Right:) Distribution of residuals with respect to the degree of stenosis for all samples using general regression and piecewise regression model; filled data points indicate results from the piecewise model. (General model average residual and standard deviation: 0.86 and 3.10, respectively. Piecewise

model average residual and standard deviation: 0.28 and 0.90, respectively). (B) Distribution of the OSI from CFD and piecewise regression model obtained using 45 cases. Filled data points show values predicted by the model that were not used in development of the model (5 cases). (Right:) Distribution of residuals with respect to the degree of stenosis for all samples using piecewise regression model. (Average residual and standard deviation: 0.35 and 1.18, respectively). (C) Distribution of the RRT from CFD and regression models (general and piecewise) obtained using 45 cases. Filled data points show values predicted by the model that were not used in development of the model (5 cases). (Right:) Distribution of residuals with respect to the degree of stenosis for all samples using general regression and piecewise regression model; filled data points indicate results from the piecewise model. (General model average residual and standard deviation: 0.46 and 1.27, respectively. Piecewise model average residual and standard deviation: 0.43 and 1.18, respectively). For all (A), (B) and (C), datapoints are labeled with different colors (Green, Blue and Red; from low to high) indicating their associated stenosis severity category, and dotted lines represent 95% confidence intervals. (For interpretation of the references to color in this figure legend, the reader is referred to the Web version of this article.)

CHAPTER 4

INTRINSIC COATING MORPHOLOGY MODULATES ACUTE DRUG TRANSFER IN DRUG-COATED BALLOON THERAPY[3]

[3] Chang G. H.*, Azar D. A.*, Lyle C., Chitalia V. C., Shazly T., Kolachalama V. B. 2019. Intrinsic coating morphology modulates acute drug transfer in drug-coated balloon therapy. Nature Springer - *Scientific Reports.* 9:6839. *Indicates equal contribution. DOI: https://doi.org/10.1038/s41598-019-43095-9

Reprinted here with permission of publisher.

4.1 ABSTRACT

The hallmark of drug-coated balloon (DCB) therapy for the treatment of peripheral vascular disease is that it allows for reopening of the narrowed lumen and local drug delivery without the need for a permanent indwelling metal implant such as a stent. Current DCB designs rely on transferring drugs such as paclitaxel to the arterial vessel using a variety of biocompatible excipients coated on the balloons. Inherent procedural challenges, along with limited understanding of the interactions between the coating and the artery, interactions between the coating and the balloon as well as site-specific differences, have led to DCB designs with poor drug delivery efficiency. Our study is focused on two clinically significant DCB excipients, urea and shellac, and uses uniaxial mechanical testing, scanning electron microscopy (SEM), and biophysical modeling based on classic Hertz theory to elucidate how coating microstructure governs the transmission of forces at the coating-artery interface. SEM revealed shellac-based coatings to contain spherical-shaped microstructural elements whereas urea-based coatings contained conical-shaped microstructural elements. Our model based on Hertz theory showed that the interactions between these intrinsic coating elements with the arterial wall were fundamentally different, even when the same external force was applied by the balloon on the arterial wall. Using two orthogonal cell-based assays, our study also found differential viability when endothelial cells were exposed to titrated concentrations of urea and shellac, further highlighting the need to maximize coating transfer efficiency in the context of DCB therapies. Our results underscore the significance of the excipient in DCB design and suggest that coating microstructure modulates acute drug transfer during device deployment.

4.2 INTRODUCTION

Peripheral arterial disease (PAD) was estimated to affect over 200 million people around the world in the preceding decade and this number is increasing continuously [141,142]. Endovascular interventions such as percutaneous transluminal angioplasty (PTA) with or without stenting are among the preferred choices for the treatment of PAD. Recent randomized controlled clinical trials have demonstrated the superiority of drug-coated balloon (DCB) therapy when compared to PTA alone, at least in terms of improved patency and reduced target lesion revascularization [143–147]. In all these studies, paclitaxel (PTX) was the drug of choice but each device differed in terms of the drug dosing, the selection of the excipient and the overall coating formulation. For example, two DCBs that have recently obtained regulatory approval within the United States have 3.5 μg/mm2 of PTX with urea as the excipient (IN.PACT Admiral, Medtronic, Santa Rosa, CA, USA), and 2 μg/mm2 of PTX with a mixture of polysorbate and sorbitol as the excipient (Lutonix DCB, C. R. Bard, New Hope, MN, USA), respectively. Additionally, few DCBs that are undergoing clinical trials as well as the ones in development also use PTX as the drug, (e.g. Stellarex DCB, Spectranetics, Colorado Springs, CO, USA containing 2 μg/mm2 of PTX with polyethylene glycol as the excipient). During the endovascular procedure, the belief is that an optimal coating enables efficient transfer of drug from the balloon to the artery, with concomitant adherence to the arterial wall. The adhered coating is then expected to serve as a sustained drug source, leading to a second phase of drug delivery to the arterial wall. Studies have shown that only a small portion (<8%) of the coating gets transferred during balloon inflation [148], and almost 90% of the delivered drug is lost within about 24–48 hours [31]. These numbers point to the poor efficiency of drug delivery from balloon catheters.

Hence, there is a need to better understand the factors influencing delivery efficiency and what causes these persistent limitations [30,32]. We sought to examine the interactions between the balloon coating and the arterial wall on multiple scales to better understand device-dependent arterial pharmacokinetics. We selected PTX as the drug along with urea and shellac as the excipients for the balloon coating in our experimental study. While a balloon catheter using urea as an excipient is already in clinical use within the United States (IN.PACT Admiral, Medtronic) for the treatment of PAD [146,147], a DCB device with shellac as the excipient (DIOR II, Eurocor) is approved in the European Union for coronary applications [149]. First, we performed a series of bench-top experiments to estimate coating-specific mechanical behavior that allowed us to characterize the contact between the balloon coating and the arterial wall. Using these parameters, we developed a biophysical model to quantify the interfacial mechanics as a function of the intrinsic shape of the coating microstructure and the force applied by the balloon on the arterial wall. Developed metrics of interfacial mechanics were then associated with experimental measurements of arterial drug transfer. To further quantify excipient-based differences among potential DCBs, we examined cultured human endothelial cell viability when treated with increasing concentrations of urea and shellac. While the mechanical tests and modeling relate to essential device function at the time of DCB deployment, the latter studies are relevant to the notion of increasing coating adherence/retention to serve as a sustained drug source. Taken together, obtained results underscore the importance of coating composition as a determinant factor of DCB efficiency and suggest that coating microstructure modulates the acute drug delivery from these devices.

4.3 MATERIALS AND METHODS

4.3.1 Preparation of PTX-excipient coated and control films

We developed balloon coatings with PTX and urea (1:1), as well as with PTX and shellac (1:1), using a micropipetting-coating method. Briefly, urea and shellac, 5–20% w/v, were dissolved in ethanol-200 at ~200 rpm for 4–6 hours. PTX solution was prepared in ethanol-200 at 10 mg/mL and added dropwise to the excipient solutions to generate several (5–20%) w/v mixtures. Each solution was then micropipetted on a sheet of balloon material (Nylon-12), and was kept at room temperature for 6 hours, which resulted in a coated surface with 3 μg/mm^2 PTX with either excipient. The dried films were cut in 25 × 25 mm squares and glued to a rigid 3D-printed testing block, creating flat test elements for uniaxial mechanical testing (Figure 4.1A).

4.3.2 Mechanical characterization of coated balloon in isolation

The compressive mechanical response of coated balloons was measured using a mechanical testing system (Bose ElectroForce 5270) configured for uniaxial testing. The test elements were placed between two flat plates, and subjected to a compressive displacement (0.005 mm/sec) until the force response was 1, 2 or 3 N. Once the target force was reached, the compression plates were held at the same position for a dwell time of 60 s, following by unloading of the sample at the same displacement rate. Sample force and displacement data (Figure 4.1B) were continuously recorded at an acquisition rate of 20 s^{-1} using a system-integrated software (Wintest).

To facilitate calculation of the reduced modulus of the coated balloon, the resultant force-displacement data were fit to a two-term exponential model, defined as:

$$F = \sum_{i=1}^{2} e^{\alpha_i \delta_b} \qquad (4.1)$$

where F is the recorded compressive force, δ_b is the displacement, and α_i are the parameters for the exponential model (Figure 4.2). The reduced elastic modulus of the coated balloon then becomes:

$$\frac{1}{E_b^*} = \sqrt{A}\frac{d\delta_b}{dF} \quad (4.2)$$

where

$$\frac{d\delta_b}{dF} = \left[\sum_{i=1}^{2} \alpha_i e^{\alpha_i \delta_b}\right]^{-1} \quad (4.3)$$

4.3.3 Mechanical characterization of coated balloon in contact with arterial vessel

During balloon inflation, the coating contacts and directly interacts with the arterial wall. To facilitate procedural simulation with our coated balloon test elements, we created analogous flat arterial tissue elements from porcine femoral arteries obtained from a local abattoir immediately following animal sacrifice (8-12-month-old, 75-125 lbs., male American Yorkshire pigs). We configured these two elements – the coated balloon and arterial tissue sample – in series to enable uniaxial compression testing (Figure 4.1A). The same loading-dwell-unloading protocol as described above was applied to this 2-element system. Obtained data allowed relation of the overall compliance of this 2-element system ($d\delta_0/dF$) to E_b^* (obtained above; Figure 4.1B), and the reduced modulus of the arterial wall (E_t^*), as:

$$\frac{1}{E_t^*} = \sqrt{A}\,\frac{d\delta_0}{dF} - \frac{1}{E_b^*} \quad (4.4)$$

where δ_0 is the total displacement of the 2-element system, F is the recorded compressive force, A is the overall contact area between the balloon coating and the arterial wall, E_b^* and E_t^* are the reduced moduli of the balloon and arterial wall, respectively [150,151].

4.3.4 Scanning electron microscopy

Variable pressure scanning electron microscopy (SEM) (Tescan Vega-3 SBU) was used to assess the surface microstructure of the coated balloons. Obtained images were processed to measure the average intrinsic shape of the coatings (MATLAB, MathWorks, Natick, MA). Each SEM image was first converted to grayscale and then binarized. The 'regionprops' feature was used to read all the objects within the binarized image and several properties including mean perimeter and mean contact angle were estimated that defined the intrinsic shape of shellac and urea microstructures, respectively (Figure 4.3A and B). For shellac, we observed a spherical microstructure, whereas for urea, we noticed a micro needle-like structure with a polygonal cross-section along the length of the needle, thus representing a conical contact with the arterial surface. Note that the conical contact assumption was made for cases when the micro needle was lying flat on the arterial surface or when the tip of the micro needle was in contact with the arterial surface.

4.3.5 Contact mechanics model

We modeled the interactions between the balloon coating and the artery during balloon angioplasty as an elastic contact problem using the classic Hertz theory. The surface of the balloon coating has a unique microstructure characterized by its intrinsic shape and asperity. For PTX-shellac, we assumed that when these spherical microstructures come in contact with the arterial vessel, they result in an elastic deformation within the region of the point of contact. This contact region is smaller than the surface area of the spherical element and is defined using (Figure 4.3C):

$$a_0 = \sqrt{\delta R} \qquad (4.5)$$

where a_0 is the contact radius, δ is the indentation depth, and R is the radius of the intrinsic spherical elements [152,153]. The resulting force applied by the spherical element on the arterial wall then becomes:

$$F_0 = \frac{4}{3} E_t^* R^{1/2} \delta^{3/2} \qquad (4.6)$$

where E_t^* is the reduced elastic modulus of the arterial wall. While the force applied results in the elastic interaction between the spherical coating element and the arterial wall, only the contact region experiences this force. Thus, the distribution of this force over a smaller region is quantified by the mean contact pressure $\bar{P} = F_0/(\pi a_0^2)$. For PTX-shellac, this becomes:

$$\bar{P} = \frac{4}{3\pi} E_t^* \sqrt{\frac{\delta}{R}}\,. \qquad (4.7)$$

For the case of PTX-urea, the observed needle-like structures were considered as conical structures with sharp facet angles (Figure 4.3B), where the contact radius is defined as (Figure 4.3D):

$$a_0 = \frac{2\delta}{\pi \tan\theta} \qquad (4.8)$$

where θ is the angle (assumed as 30°) between the conical shape and the indented surface [152,154]. The total force applied by each conical element then becomes:

$$F_0 = \frac{2E_t^* \delta^2}{\pi \tan\theta} \qquad (4.9)$$

and the mean contact pressure for each element is defined as:

$$\bar{P} = \frac{1}{2} E_t^* \tan\theta \qquad (4.10)$$

4.3.6 Measurement of arterial drug transfer

Stored arterial vessel samples (obtained after mechanical testing) were prepared for high-performance liquid chromatography (HPLC) to measure the amount of transferred drug. Each sample was first submerged in methanol and vortexed briefly. The vessel was then homogenized in methanol for 3 minutes using a probe sonicator and vortexed again for 10 minutes. The sample was then centrifuged at 1000 rpm for 10 minutes. The supernatant holding the extracted drug was transferred to a fresh experiment tube. This sample was diluted in methanol and readied for HPLC testing. The extraction method above was validated by two control experiments; dissolving known amounts of drug in methanol and loading drug (paclitaxel) onto vessel samples followed by rapid freezing, extraction using methanol and dilution prior to HPLC. Then, standard solutions and sample solutions were analyzed through HPLC.

4.3.7 Cell culture

We performed cell culture experiments to determine if the presence of different balloon coating materials would affect cell viability. Human umbilical endothelial cells were cultured as described previously [155]. Cells were maintained at 37°C and 5% CO_2. Early passage cells (less than eight passages) were used for the study.

4.3.8 Flow cytometry

To examine the cytotoxicity of the excipients on live cells, LIVE/DEAD staining followed by analysis was conducted. Endothelial cells (2×10^5) were plated in 12 well plates and were treated for 24 hours with a titrated concentration of the shellac and urea. Molecular grade ethanol (Pharmco) was used to dissolve shellac (Sigma Aldrich) (10 μM – 100 mM) and double distilled autoclaved water was used to dissolve urea (Sigma

Aldrich) (10 μM – 100 mM). Single cell suspensions were analyzed using FACS LSR II (BD Biosciences). Cells were harvested and viable versus non-viable cells determined by staining with Zombie UV™ Fixable Viability Kit (Biolegend), as described previously [156,157]. Cells were stained in dark conditions for 30 minutes at room temperature in protein free phosphate buffered saline. Gating was done on live cells whose intact membranes prevent dye infiltration while dye positive dead cells were excluded. The positive control consisted of dead cells, which were induced using Staurosporine [158]. Data were analyzed with Flowjo software (Tree Star).

4.3.9 Cell viability assay

To examine the cytotoxicity of the excipients, viability of the cells was determined by measuring released ATP using the Cell Titer–Glo Luminescent assay (Promega) performed using manufacturer's instructions. Endothelial cells (5×10^4/100 μL) were plated on a 96 well plate and treated with various concentrations of 200 proof ethanol (Pharmco) dissolved shellac (10 μM – 100 mM) and double distilled autoclaved water dissolved urea (10 μM – 100 mM) for 24 hours. Cell Titer Glo buffer and substrate were equilibrated to room temperature. The buffer was added to the lyophilized substrate and mixed gently using vortexing. Equal volume (100 μL) of the homogenous solution was added to the plated cells. Luminescence was measured with a plate reader. Luminescent signal is proportional to the amount of ATP. Presence of ATP is directly proportional to the number of viable cells in culture. Data were analyzed with GraphPad Prism.

4.3.10 Statistical analysis

Descriptive statistics are presented as the mean and standard deviation. Unpaired Student's t-test was used to compare experimental groups as appropriate. For some cases,

significance of the Pearson correlation coefficient was computed using two-tailed probability, given the correlation value (R^2) and the sample size. A p-value less than 0.05 was considered statistically significant.

4.4 RESULTS

4.4.1 Surface morphology of the coatings

SEM imaging allowed us to characterize the distinct morphologic structures of PTX-urea and PTX-shellac, respectively (Figure 4.3A-B). We performed image processing on the SEM images to measure the intrinsic shape and the number of microstructures per unit area of the coating microstructures. The shellac coating consisted of spherical microstructures with a mean radius of 0.84 μm and a standard deviation of 0.30 μm (Figure 4.3A), and the microstructures distributed densely with 0.18 microstructures per square micrometer. The urea coating consisted of needle-like crystalline microstructures with a mean length of 21.6 μm and a standard deviation of 8.5 μm (Figure 4.3B), and the microstructures distributed more sparsely with 0.003 microstructures per square micrometer. As these surface morphologic signatures can lead to dissimilar modes of interaction with the arterial vessel, we hypothesized that these modes can also lead to differential drug transfer patterns. Additionally, the Hertz theory allowed us to relate SEM-observed intrinsic shapes of the coatings to define the contact regions between the balloon coating and the vessel wall.

4.4.2 Mechanical properties of the test elements

We leveraged uniaxial compression testing to simulate the coating-artery interaction during angioplasty. The compression phase of the experiment simulates balloon

inflation, which was reflected as a gradual increase in tissue displacement with increasing applied compressive force. The compressive moduli of the test samples were calculated from the force-displacement (FD) curves during the compression phase. During the 60 s displacement dwell period, the test constructs underwent a relaxation phase, as indicated by the gradual reduction in compressive force. During the decompression phase, the coating is separated from the contact region and the applied force gradually returns to zero, indicating complete interfacial failure, which could be attributed to adhesive failure of formed interface and/or fracture of the balloon coating (Figure 4.1B).

The first set of mechanical testing experiments generated FD curves during the compression phase when shellac- and urea-coated balloons were compressed on flat, rigid surfaces, respectively (Figure 4.4A-B). These experiments allowed us to estimate the mean compliance values of both the urea- and shellac-coated balloons at the maximum compressive force of 1, 2 and 3 N, respectively (Figure 4.4C). Interestingly, there were no statistically significant differences between the mean compliance values of shellac- and urea-coated balloons ($p=0.36$ for 1 N, $p=0.41$ for 2 N and $p=0.62$ for 3 N). The second set of mechanical testing generated FD curves during the compression phase when shellac- and urea-coated balloons were compressed on excised femoral arteries opened *en face* so that the intraluminal side of the vessel was in contact with the balloon coating (Figure 4.4D-E). Mean overall compliance values of the 2-element test constructs were then computed (Figure 4.4F). Even for this set of experiments, we found no statistically significant differences between the mean overall compliance values of shellac and urea ($p=0.27$ for 1 N, $p=0.87$ for 2 N and $p=0.84$ for 3 N). Later, for each experiment that generated a unique FD curve during the compression phase, the compliance of the arterial vessel used for that

experiment was then computed as the net difference between the overall compliance of the 2-element system and the estimated average compliance of the coated balloon. In this fashion, we were able to compute arterial sample-specific estimates of compliance, and these values were used further to quantify the coating-artery interactions. Taken together, these results imply that within our experimental design space and under the examined mode of coating-tissue interaction, bulk interfacial mechanics are insensitive to excipient type.

4.4.3 Relating coating-specific interactions with arterial drug transfer

We hypothesized that coating surface microstructure impacts the interactions between the coating and the arterial wall. We computed the mean contact pressure for each coating, which is a function of the applied force and the contacting surface area of the coating (Figure 4.5A). Interestingly, we found statistically significant differences in the mean contact pressure values between shellac and urea as a function of application force (p=1.2e-2 for 1 N, p=3.3e-3 for 2 N and p=7.6e-4 for 3 N). We also found that the size of the contact region was different between urea and shellac, respectively (Figure 4.5B), regardless of the amount of application force (p=1.0e-4 for 1 N, p=6.0e-4for 2 N and p=2.2e-3 for 3 N). Importantly, the arterial drug uptake following mechanical testing correlated with mean contact pressure in a coating-specific fashion (Figure 4.5C; $R^2 = 0.45$, p=1.3e-2 for urea and $R^2 = 0.05$, p=0.465 for shellac). These results indicate a stronger correlation of drug uptake with mean contact pressure in the case of urea than for shellac. Systematic analysis in this fashion can allow us to quantify these relationships to a broad range of candidate excipients.

4.4.4 Cytotoxicity of the excipient

While the coating shape-dependent aspects associated with corresponding transfer of the balloon coating, the task was to determine how these coatings behaved within the cellular environment. As such, DCBs are placed within the vessel wall, which exposes the coating directly to the vascular endothelium. To this end, human umbilical endothelial cells were exposed to titrated concentrations of shellac and urea for 24 hours. The cells were subjected to LIVE/DEAD and ATP release assays, respectively. Both these assays showed that low concentrations (10 μM/mL) of shellac and urea did not affect cell viability compared to vehicle treated cells (Figure 4.6A-B). However, shellac from 10μM to 100μM resulted in an increase from 8.5% cell death to 30.5% cell death. This change was not found in similar concentrations of urea. Increasing the concentration of urea from 10μM to 100μM, did not affect cell viability and this trend continued up to a 10,000-fold increase of urea to 1mM. These data corroborated with the luminescent cell viability assay (Figure 4.6C). Shellac demonstrated a dose-dependent decrease in cell viability. Cells treated with higher dosages of shellac resulted in decreased ATP levels when compared to cells treated with the same concentration of urea (Figure 4.6D). Since the presence of ATP is an indicator of metabolically active cells, this assay strongly suggests that shellac potentially decreases cell viability at high concentrations. Collectively, both these assays consistently showed lower viability at an eqimolar concentration of shellac compared to urea.

4.5 DISCUSSION

Catheter-based endovascular therapy involving balloon angioplasty in concert with local drug delivery is highly appealing as it circumvents the use of permanent indwelling implants such as stents [27,31,33,34,159–161]. Balloon angioplasty alone or angioplasty followed

by stenting as such have stood the test of time [162], and their strengths as well as limitations are appreciated by the clinical community. On the other hand, clinical studies focused on intraluminal delivery of therapeutic compounds from these balloon catheters have demonstrated great promise but have not yet fully proven to result in a sustained, long-term benefit [146,163,164]. Balloon-vessel contact times are short due to the nature of the procedure (2–3 min), and moreover, the process of coating transfer from the balloon to the vessel wall and drug delivery efficiency within this period are not fully understood. Continuation of this trend can lead to a problem - DCB therapy could remain under-appreciated and interventional strategies for PAD using currently approved DCBs can lead to sub-optimal outcomes. It is therefore important to identify factors that promote efficient delivery and track consequent arterial pharmacokinetics.

Using a series of bench-top experiments and modeling the interaction between the balloon coating and the arterial wall (Figure 4.1), we computed compliance values of the arterial wall and mean compliance values of the balloon coating. Using the classic Hertz theory, we defined shape-specific contact mechanics and the contact force applied on the arterial wall. Mean contact pressure, which is a function of the contact force and the intrinsic shape of the coating, was then computed for each of these cases and associated with corresponding acute transfer of the balloon coating (Figure 4.5E). Also, endothelial cells exposure to either shellac or urea, induced differential toxic effects that were dose-dependent (Figure 4.6). These results underscore the importance of fully characterizing the nature of the excipients so as to optimize DCB therapy.

The DCB excipient has an important role to play before, during and after balloon angioplasty. During the pre-procedural or the design phase, a coating technique is used to

create a thin layer on the surface of the balloon, where the excipient directly plays a role to support adhesion of the coating to the balloon. During the procedure, as the balloon is expanded to reopen an occluded arterial vessel, a portion of the balloon-adhered drug coating detaches from the balloon and gets transferred to the arterial wall. Here, the excipient acts as the carrier to facilitate rapid drug transfer to the mural surface. The procedural time is short (~2–3 minutes) but can be logically considered as 2 sub-phases defined as the compression and decompression of the tissue-balloon interface (Figure 4.1B). During the compression sub-phase, the coating is adhered to the balloon and concomitantly initiates contact with the mural surface. This mechanical contact initiated due to the radially outward force generated by balloon expansion leads to adhesion of the coating to the mural surface. Several properties of the excipient play a role in terms of dictating the extent of adhesion. During the decompression sub-phase, the radially inward force generated by balloon deflation generates interfacial failure between the mural surface and the drug coating and potentially between the balloon and the drug coating. Cohesive bond failure within the coating itself is also a possibility during the decompression sub-phase. Once the procedure is completed, the expectation is that the transferred drug coating continues to adhere to the mural surface, which can lead to a sustained therapeutic response. In this phase, the excipient acts as an agent to support adhesion and creates a source for local delivery of drug to the mural surface. In sum, the pre-procedural design considerations, the procedural aspects involving different modes of bonding failure and post-procedural phenomenon related to mural adhesion of drug coating can together determine the success of DCB delivery. As a first step towards fully characterizing the role of excipients, we focused on quantifying the impact of coating surface morphology and its

interaction with the mural surface during the procedure on acute transfer of the balloon coating.

Our study's main finding is that the unique microstructure of the balloon coating can directly impact acute transfer of the balloon coating. This is due to the fact that at this scale, the interaction between a spherical-shaped element and the arterial wall is fundamentally different from that of a conical-shaped element, even when the same external force is applied by the balloon on the arterial wall. The classic Hertz theory allowed us to mathematically decompose this deterministic aspect of contact mechanics (Figure 4.3C-D) in terms of the mean contact pressure associated with a specific excipient and application force (Figure 4.5A-B). We found distinct differences in balloon transfer of paclitaxel as a function of mean contact pressure for urea and shellac (Figure 4.5E).

Our study has some limitations. We used explanted porcine femoral arteries for mechanical testing and for subsequent measurements of drug transfer. These vessels may lose some structural integrity immediately after sacrifice, even though we took utmost care to preserve tissue viability. Our uniaxial mechanical testing protocol is designed to isolate contact phenomena that likely underlie DCB performance, but does not mimic exact clinical deployment of these devices. We assumed linear elastic behavior for all components in our contact mechanical model, although nonlinear effects may become important at larger strains/strain rates experienced in device deployment. During mechanical testing, both cohesive and adhesive bond forces play a role during compression and decompression phases, respectively, and this dynamic may ultimately determine the amount of drug coating adhered to the vessel wall. We did not attempt to isolate the individual roles of cohesion and adhesion in the context of our study, as our goal was to

estimate metrics relevant to balloon-tissue contact and acute drug transfer. This type of bonding failure (adhesive or cohesive) will dictate the amount of drug coating that is retained on the mural surface under physiologic conditions (i.e. blood flow), and is thus significant to drug retention at the application site.

In conclusion, our study connects the application force, which is a procedural factor that exemplifies balloon angioplasty with the intrinsic shape of the balloon coating microstructure, which is a design parameter of the device itself. By relating the coating-specific morphology and its subsequent interactions with the arterial vessel, we have demonstrated a mechanistic basis by which to evaluate different balloon coatings. While examination of bulk interfacial mechanics found no coating-specific differences, mean contact pressure computed by normalizing the application force with the intrinsic shape of the coating was significantly different between urea and shellac. This means that no two excipients can be alike in terms of their microscopic mechanical interactions with the arterial vessel, and when coated on the balloons along with the same drug can still result in differential arterial pharmacokinetics. Our paradigm can be further used to design coating formulations that can have maximal balloon transfer of drug, higher arterial uptake and minimal loss within the systemic circulation, thereby paving way towards efficient therapeutic approaches using balloon catheters.

4.6 ACKNOWLEDGEMENTS

This work was supported by the American Heart Association through a Scientist Development Grant [17SDG33670323 to V.B.K]; the Hariri Institute for Computing and Computational Science & Engineering at Boston University through a Research Award to V.B.K; the National Center for Advancing Translational Sciences, National Institutes of

Health, through BU-CTSI Grant [1UL1TR001430 to V.B.K]; the Whitaker Cardiovascular Institute at Boston University School of Medicine through a pilot grant award to V.B.K; the National Institutes of Health through a T32 training grant [DK007053-44 to C.L.]; and the National Institutes of Health [R01HL132325 and R01CA175382 to V.C.C.]. Its contents are solely the responsibility of the authors and do not necessarily represent the official views of the NIH.

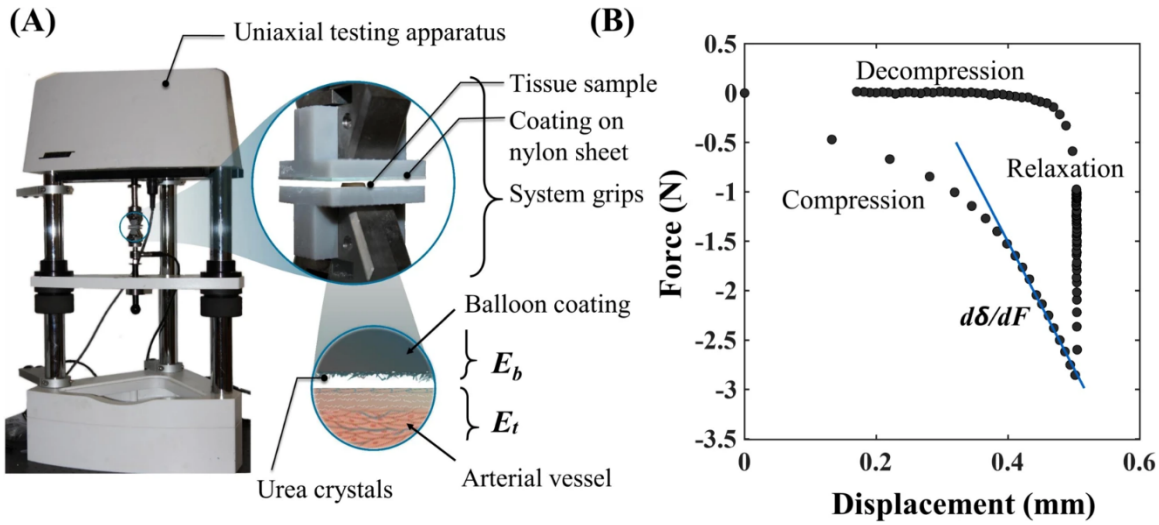

Figure 4.1: Mechanical testing setup and a typical mechanical testing result.
(A) Mechanical testing setup customized for uniaxial compression testing. Schematic of the 2-element test system containing the arterial vessel and the drug-coated balloon is also shown. (B) A typical force-displacement (FD) curve that results from a mechanical test. Data resulting from the FD curve was used to estimate compliance values of the test construct.

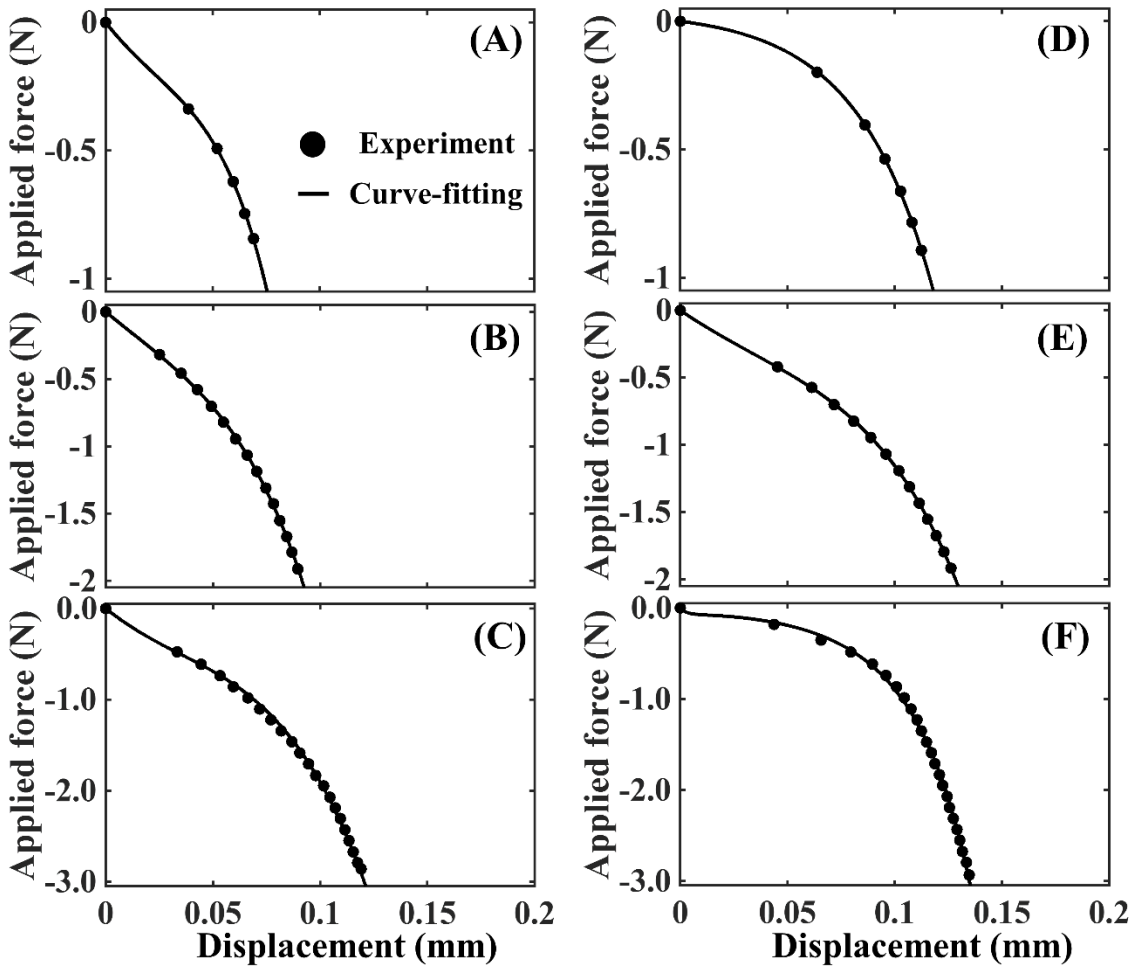

Figure 4.2: Force-displacement curves.
(A-C) Average force-displacement curves generated from the compression test. Curve-fitting results for the shellac coated balloon with application force of 1N (A), 2N (B) and 3N (C) are shown. (D-F) Average force-displacement curves for the compression test, followed by curve-fitting results for the urea coated balloon with application force of 1N (D), 2N (E) and 3N (F) are shown.

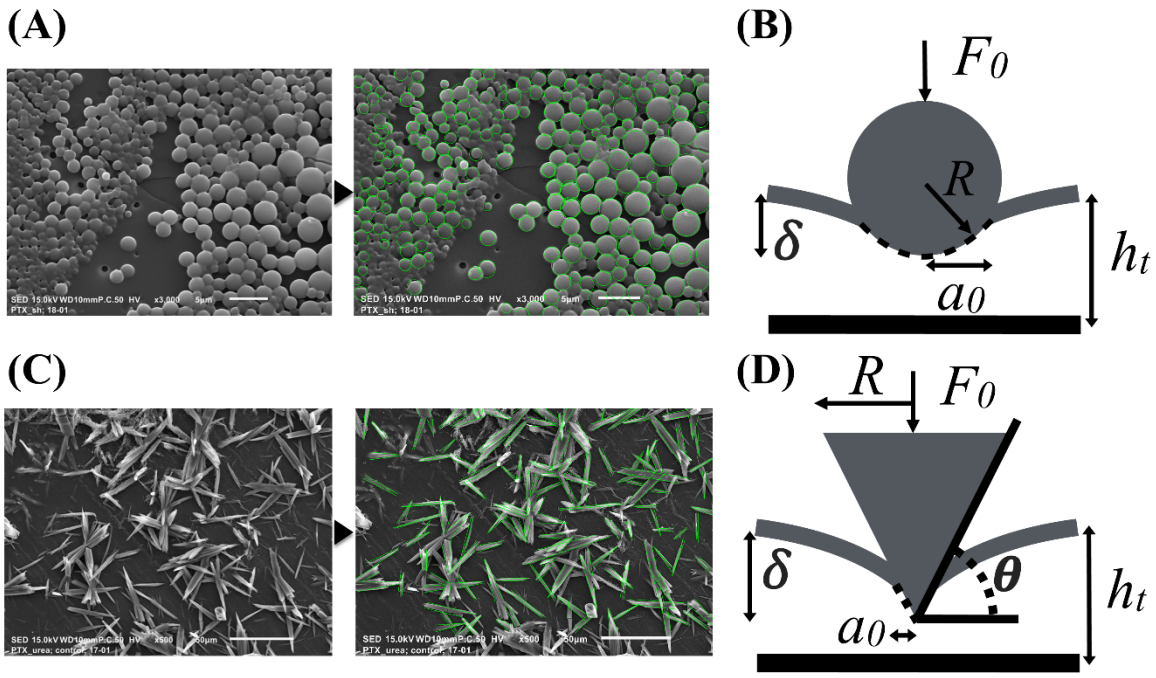

Figure 4.3: Intrinsic shape of the balloon coatings.
SEM imaging revealed a spherical structure for shellac (A), and conical structure for urea (B). Contact mechanics models were developed based on Hertz theory by considering a spherical element for shellac (C) and a conical element for urea (D).

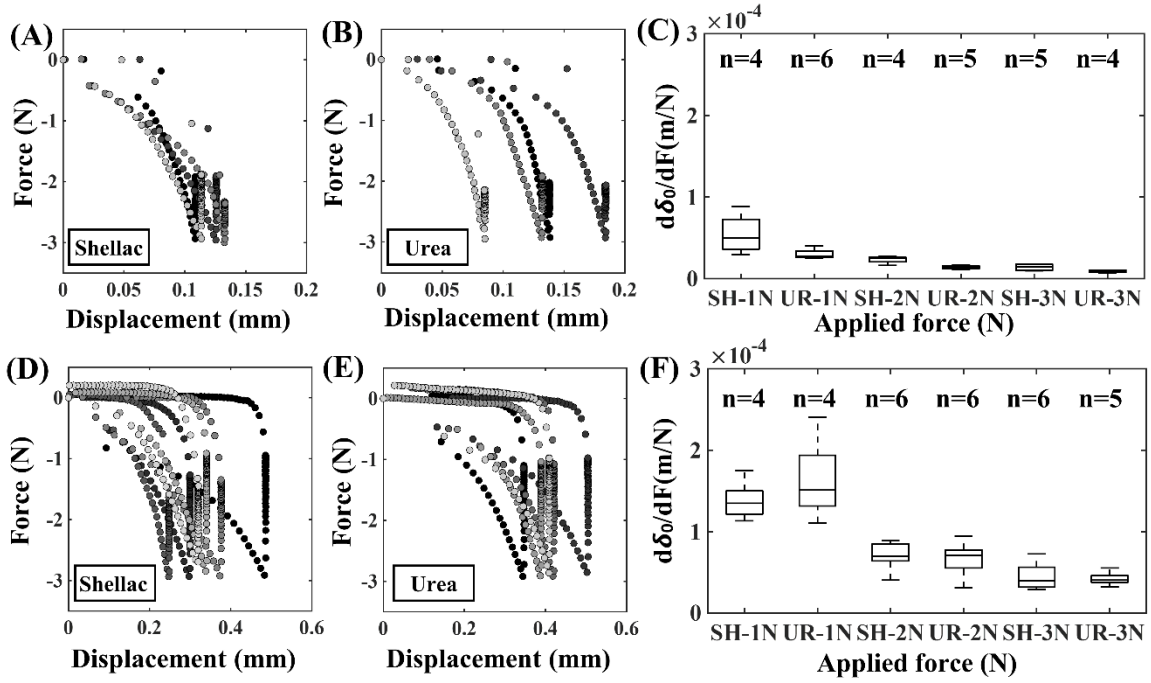

Figure 4.4: Bulk interfacial mechanics are independent of excipient type.
Force-displacement (FD) curves from the mechanical test when shellac (A) and urea (B) were used as the balloon coating materials, respectively. For (A) and (B), the test element comprised of the balloon coating compressed on a flat, rigid surface, which allowed us to estimate the balloon compliance (C) of shellac (indicated by the abbreviation SH) and urea (indicated by the abbreviation UR), respectively. FD curves from the mechanical test when shellac (D) and urea (E) were used as the balloon coating materials, respectively, where the test element comprised of the balloon coating compressed on an excised porcine arterial vessel. This experiment allowed us to estimate the overall compliance values of the 2-element system (F) with shellac and urea, respectively. The dwell time was maintained at 60 s with a maximum application force of 3N.

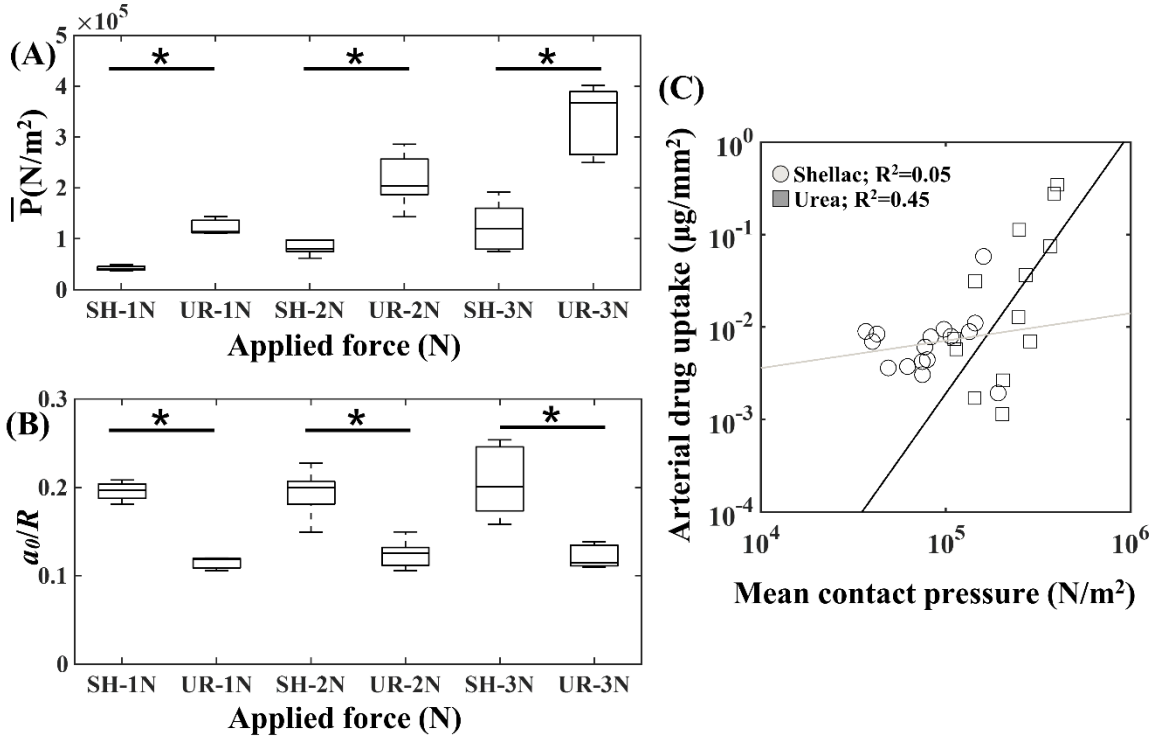

Figure 4.5: Excipient microstructure modulates acute transfer of balloon coating. (A) Mean contact pressure was computed by normalizing the application force with the intrinsic shape of shellac and urea. (B) Normalized contact radius was different between shellac and urea as well. Asterisks indicate statistical significance ($p<0.05$). (C) Net coating transfer as a function of mean contact pressure for urea and shellac. Data on both axes is plotted in log-10 scale.

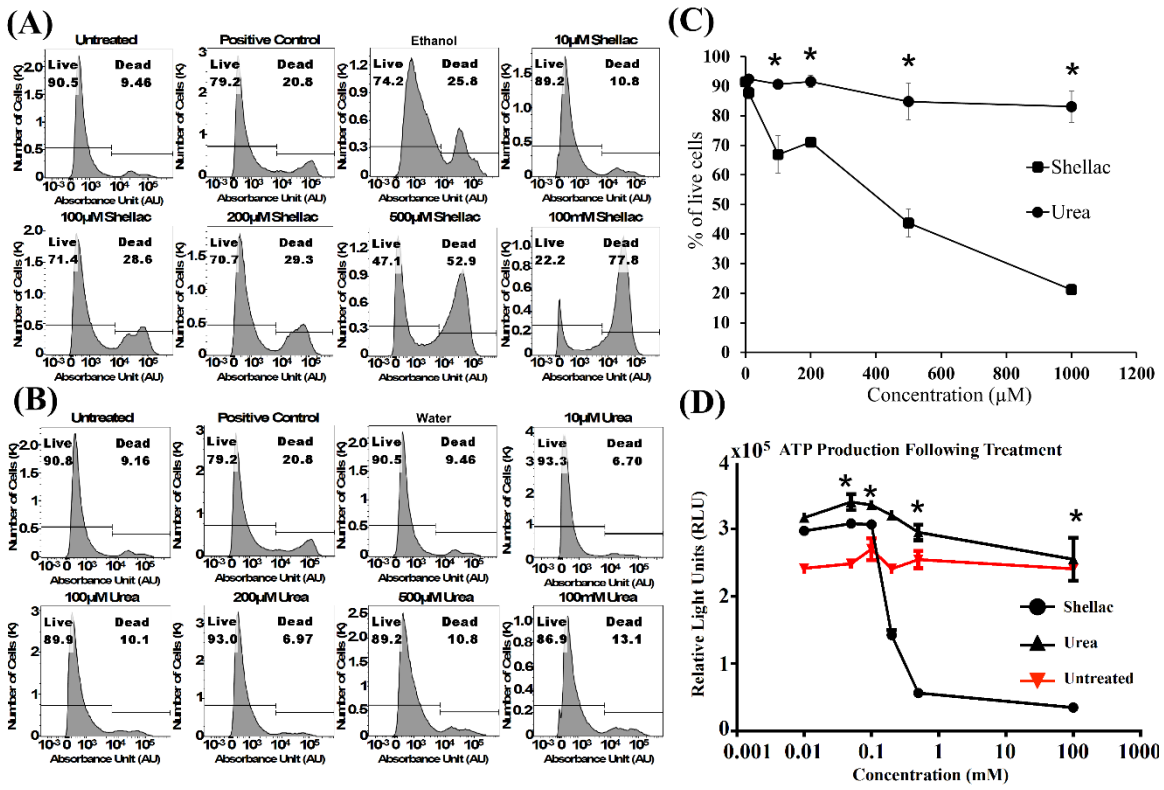

Figure 4.6: Cytotoxicity of the excipients.

(A) and (B) Cell death with increasing concentrations of shellac and urea. Endothelial cells (1x106) were treated for 24 hours with increasing concentrations of shellac and urea. Cells were harvested and stained with Zombie UV™ viability fluorescent dye and analyzed by flow cytometry. Heat-shocked cells were used as positive control. Ethanol was used as a vehicle control for shellac and water for urea. Representative Fluorescence Activated Cell Sorting (FACS) images from two independent experiments is shown. Increase in concentration of urea did not result in decreased cell viability. (C) Average percentage of live cells in response to the treatment of shellac and urea done in two independent experiments is shown. The symbol * indicates p-value that compares live cells between shellac and urea-treated samples. Also, p = 0.03 for 100 µM, p = 0.005 for 200 µM, p = 0.017 for 500 µM, p = 0.004 for 1000 µM. Standard errors are shown on error bars. (D) Average of ATP production from two independent experiments is shown. ATP production indicates the viability of endothelial cells as a function of increasing concentrations of urea and shellac. The symbol * indicates p-value that compares ATP between shellac and urea-treated cells. Also, p = 0.02 for 100 µM, p = 0.001 for 200 µM, p = 0.001 for 500 µM, p = 0.01 for 1000 µM. Increase in concentration of urea did not compromise ATP production in endothelial cells. Standard errors are shown on error bars.

CHAPTER 5

SURFACE MODIFICATION USING ULTRAVIOLET-OZONE TREATMENT ENHANCES ACUTE DRUG TRANSFER IN DRUG-COATED BALLOON THERAPY[4]

[4] Azar D., Lott J. T., Jabbarzadeh E., Shazly T., Kolachalama V. B. 2020. Surface modification using ultraviolet-ozone treatment enhances acute drug transfer in drug-coated balloon therapy. Submitted to American Chemical Society - *Langmuir*. DOI: https://doi.org/10.1021/acs.langmuir.0c00298

5.1 ABSTRACT

Endovascular deployment of drug-coated balloons (DCB) is an emerging strategy for revascularization of arterial disease. Randomized clinical trials have demonstrated DCB effectiveness, but a recent meta-analysis reported increased mortality risk in humans with use of DCBs containing the common antiproliferative drug paclitaxel. While many factors could have contributed to adverse outcomes, current DCB designs have poor drug delivery efficiency, risk of systemic toxicity, and limited potential to retain therapeutic drug concentrations within the arterial wall following the procedure. Our study focuses on developing a strategy to enhance acute drug transfer from the balloon to the arterial wall over the short procedural window (~30-120 secs). We employed ultraviolet-ozone plasma (UVO) treatment to increase the hydrophilicity of a prototypical balloon material (Nylon-12), and subsequently applied a urea-paclitaxel coating previously shown to undergo favorable adhesive interactions with the arterial wall under simulated ex-vivo deployment. A series of assays were performed to characterize our experimental DCBs in terms of UVO-induced alterations in balloon surface hydrophobicity, formed coating microstructure, coating stability, and acute drug transfer to the arterial wall. Obtained results suggest that UVO-based surface modification of angioplasty balloons is a promising design strategy and highlight the critical role of coating microstructure in determining drug transfer efficiency in DCB therapy.

5.2 INTRODUCTION

Drug-coated balloon (DCB) therapy is increasingly considered for the treatment of peripheral arterial disease [145,147,165,166], as well as for in-stent restenosis (Giacoppo et al.,

2019) and de novo lesions [167] within the coronary vasculature. An important reason for adoption of DCB devices is both cost effectiveness and inherent avoidance of a permanent implant, such as with a metallic-based drug-eluting stent (DES). However, in a recent summary-level meta-analysis comprising randomized, controlled trials of femoropopliteal paclitaxel (PTX) coated balloon and stent interventions, [168] identified excess late mortality in paclitaxel-treated patients [168]. Following the publication of this surprising result, the U.S. Food and Drug Administration (FDA) released a letter to healthcare providers recommending DCB use in only the highest-risk patients and close post-procedural follow-up. This has led to a broad clinical pause on the use of DCB devices, as PTX is the drug used in all the FDA-approved DCBs. While there is no known causal mechanism linking PTX and mortality, the rapid and extreme FDA response to this recent study underscores our limited understanding of how DCB devices work and the conditions that can lead to untoward scenarios. Therefore, there is a clear need for better identification of factors that govern DCB performance and potentially the introduction of novel formulations that mitigate long-term adverse events.

Several experimental and computational studies have attempted to identify key factors driving DCB performance. While some investigations focused on optimizing the drug-excipient constituents and their ratios on the balloon catheters prior to delivery [169,170], others have attempted to quantify post-procedural mechanisms related to drug uptake, retention within the arterial wall [30], and spatiotemporal distribution [171]. Moreover, device manufacturers use several proprietary excipients, touting their ability to effectively deliver the drug to the vessel wall. Despite such efforts, DCB delivery efficiency remains poor, as a large majority of drug (~80-90%) gets lost within the systemic circulation [169,172–174]. In

anticipation of low delivery efficiency, PTX doses on the balloon catheters are an order-of-magnitude higher than typically used with a coronary DES [175]. Such high dosing results in a significant uptake of drug into the vessel wall during the short procedural time (~30–120 secs), likely saturating all local drug binding sites. Reversible drug binding kinetics and transport mechanisms then play an important role in determining post-procedural local drug concentrations; however, the duration over which therapeutic drug levels are maintained remains unknown. Given the recent setbacks associated with endovascular PTX delivery and our current knowledge gaps on DCBs, there is a pressing need to delineate and optimize the key factors governing DCB efficacy [176].

In our previous work [39], we reported that the DCB excipient urea enhances adhesive interactions between the coating and arterial wall during balloon deployment, and as such promotes acute PTX transfer. Through biophysical modeling, we further showed that coating-vessel contact is modulated by the coating microstructure, wherein the needle-like microstructure of urea-based coatings increases local contact pressures and promotes acute drug transfer to the arterial wall.

In this study, we extended upon our previous findings by developing a method to modulate acute drug transfer from urea-based coatings, with the purpose of enhancing PTX delivery efficiency. We leveraged ultraviolet-ozone plasma (UVO) treatment, a well-known surface modification technique, to alter the surface properties of the balloon prior to coating application [177]. We characterized UVO-treated balloon surfaces before and after coating application using dynamic contact angle measurements, scanning electron microscopy (SEM) and quantitative image analysis. Subsequently, we related the induced alterations in balloon/coating properties to coating stability and arterial drug transfer in an

ex-vivo model of DCB deployment. Our findings support UVO-based balloon surface treatment as a potential strategy to improve drug transfer efficiency, and provide further evidence linking coating microstructure to acute drug transfer during DCB deployment.

5.3 METHODS

Our study is designed to demonstrate that acute drug transfer from urea-based DCBs can be enhanced by surface modification of the balloon prior to coating application. Specifically, we explore UVO treatment as a strategy to modify the surface of Nylon-12. Our experimental approach entails preparation and characterization of a series of UVO-treated Nylon-12 surfaces, assessment of how these surfaces modulate the microstructure of a subsequently applied urea-PTX coating, and ex-vivo evaluation of formed coating stability and drug transfer efficiency when contacting the arterial wall.

5.3.1 Preparation of PTX-urea coatings

Experimental DCBs for PTX delivery were prepared using previously described techniques. Briefly, coatings containing PTX (LC Laboratories, MA) and urea (Sigma Aldrich) (w/w 1:1) were prepared via controlled micropipetting of the drug-excipient solution onto flat Nylon-12 surfaces [178]. The coating solution was formed with agitated (~200 rpm) dissolution of PTX and urea (15 mg/mL of each constituent) in ethanol (200-proof) for 4 hours. Nylon-12 films (0.5 mm thickness) were cut into squares (25 × 25 mm), sonicated in an ethanol bath at 40°C to remove any potential surface particles, uniformly coated with urea-PTX solution (120 μL), and stored at room temperature and controlled humidity (< 5%) for 6 hrs. This process resulted in coated samples with 3 $\mu g/mm^2$ of each constituent. In an identical fashion, urea-only and PTX-only coatings were prepared

(coating density of 3 μg/mm^2 for each) for comparative analyses. All samples were stored in a desiccator at room temperature until use to prevent rehydration.

5.3.2 Surface modification of balloon using UVO treatment

UVO treatment of uncoated balloon films (Nylon-12) was performed in a commercial UV-ozone surface cleaner (UV/Ozone ProCleaner, Bioforce Nanosciences). UVO treatment is a photosensitized oxygenation process, which potentiates the addition of oxygen-based functional groups to the exposed surface (Figure 5.1). During the treatment, atomic oxygen is continuously produced from ultraviolet-driven ozone-oxygen generation and dissociation cycle. Nylon-12 films were exposed to UVO treatment for 20, 40 or 60 minutes, immediately after which PTX-urea coatings were applied following the above protocol.

5.3.3 Balloon hydrophilicity

The dynamic contact angle of an evaporating sessile liquid drop placed on the balloon surfaces was used to measure hydrophilicity prior to coating application. Image capture (1.67 frames/sec) spanning the entire evaporation period of a distilled water drop was performed using a drop shape analyzer (DSA) (Kruss DSA 100 GmbH, Germany), as previously described [179]. Obtained videos were processed with custom build software developed using MATLAB to determine the dynamic contact angle of a liquid drop. To account for potential variation in drop volume, dynamic contact angle measurements were normalized with respect to time under the assumption that all drop sizes were below the capillary length.

5.3.4 Coating microstructure

Scanning electron microscopy (SEM) was used to image the surface of urea-PTX coatings, as well as PTX- and urea-only control coatings. Samples were sputter coated (2.5 kV, 20 mA) with gold-palladium nanoparticles, resulting in a 7.5 Å conductive coating over the native sample surface. SEM images were acquired at three magnification levels (100×, 400× and 1400×). A commercial image-analysis package (AMIRA, Thermo Fisher Scientific, MA, USA) was used to quantify coating surface microstructure. A systematic edge enhancement protocol was applied to grayscale images followed by conversion to binary maps. Domains of material that are in aggregate or diffuse forms were separated via threshold-based separation protocols. Briefly, material domain connections narrower than 5 pixels (~13 μm) were separated. Continuous domains larger than 100 μm^2 (domain size range: 0-50,000 μm^2) were categorized as aggregate sites, while those less than 100 μm^2 were categorized as diffuse regions. Extracted image parameters include aggregation site size, distribution, and frequency, as well as diffuse/aggregate material area fraction. To further quantify aggregate region microstructure, we defined a novel parameter based on the excluded area from an aggregated site area-equivalent circle superimposed on the image and positioned at the centroid of aggregate domain.

5.3.5 Coating stability

An in-vitro wash-off assay was used to assess coating stability under pre-deployment conditions. Coated samples were immersed in Dulbecco's phosphate buffered saline (pH 7.2) containing 0.06% (w/v) polyoxyethylene-20 sorbitan monolaurate (Tween 20) and dH2O at 37°C for 30 sec or 3 min. After the submersion period, samples were retrieved and analyzed for retained PTX content (described below).

5.3.6 Acute drug transfer to arterial vessel

A uniaxial mechanical testing machine (Bose ElectroForce 5270) was used to facilitate controlled contact between the arterial vessel samples and experimental DCB surfaces (Figure 5.2A). DCB peripheral vascular deployment was simulated via a programmed, three-stage motion of compression-dwell-decompression as previously described [39] (Figure 5.2B-C). Briefly, fresh porcine (8-12-months old, 75-125 lbs., female American Yorkshire pigs) femoral arteries were obtained from a local abattoir and used to form flat, circular (8-mm diameter) test elements. Arterial test elements were mounted onto test blocks with the endothelium exposed. Analogous test elements/blocks were formed with experimental DCB surfaces and likewise mounted with the test system. The testing blocks were placed in controlled no-force contact to initiate testing. The blocks were then compressed (0.01 mm/sec) until the force reached 8 N, then subjected to a force-controlled dwell for 30 sec, and finally decompressed (0.01 mm/sec). Both test elements were isolated, snap-frozen via submersion in liquid nitrogen, and stored at -80°C for further analysis.

5.3.7 Quantification of PTX

Coated balloon surfaces (obtained after stability test, section 5.3.5) and the arterial vessel samples (obtained after contact test with coated films, section 5.3.6) were prepared for liquid chromatography–mass spectrometry (LC-MS) to quantify PTX concentrations. To extract PTX for LC-MS analysis, each sample was submerged in HPLC-grade methanol and 0.1% Acidic acid (v/v) and vortexed for 1 min. Acidic acid was added to prevent transesterification of PTX in methanol. The samples were then sonicated twice for 30 minutes in a water bath sonicator, vortexed for 3 min between two runs, and centrifuged at

5000 rpm for 10 minutes. The supernatant holding the extracted drug was transferred to a fresh experiment tube. Each sample was diluted in methanol and prepared for LC-MS testing. The extraction protocol was validated for each substrate (coated balloon surfaces/arterial vessel samples) using controls with known amounts of PTX.

5.3.8 Statistical analysis

Standard error and mean were used to present descriptive statistics. Statistical significance between experimental groups was determined using analysis of variance (ANOVA) and unpaired t-test. For non-parametric statistical analysis of data with skewed distribution, a series of Mann-Whitney U tests were used. Pearson's correlation coefficient (ρ) was calculated among obtained biophysical variables. A p-value less than 0.05 was considered statistically significant.

5.4 RESULTS

5.4.1 Coating component morphology

Urea-only coatings exhibited a high degree of aggregation, while PTX-only coatings exhibited no discernable micro-level architecture with a largely diffuse appearance (Figure 5.3A-B). The urea-PTX coating formed a distinct, needle-like surface morphology upon application to untreated Nylon-12 (Figure 5.3C). Preliminary evidence of coating nucleation sites with urea-PTX motivated the subsequent variant characterization based on aggregation site frequency, size, and shape.

5.4.2 Balloon surface hydrophobicity

On untreated Nylon-12, the liquid drop had a high mean initial contact angle (85.6 ± 6.7°) indicating a natively hydrophobic surface (Figure 5.4A). UVO treatment reduced

surface hydrophobicity, with an approximately 40% decrease in the mean initial contact angle following a 20 min treatment ($p < 0.001$) (Figure 5.4B). Further decreases in the mean initial contact angle with prolonged UVO treatments (40 and 60 mins) also occurred, but these changes were comparatively minor and statistically indistinguishable from the response observed following the 20 min treatment (Figure 5.4C-D). In line with previous findings on canonical hydrophobic and hydrophilic surfaces [179], the drop evaporation dynamics on the untreated Nylon-12 surface was less smooth than observed following UVO treatment (all treatment times), providing further evidence for a UVO-mediated decrease in surface hydrophobicity.

5.4.3 Surface morphology of the balloon surfaces

Variably magnified SEM images of urea-PTX coatings on native Nylon-12 further demonstrate surface heterogeneity and aggregate region formation (Figure 5.5A). UVO treatment of Nylon-12 notably curtailed PTX-urea coating aggregation, resulting in a diffuse coating fraction (i.e. not in aggregate form) that became more prevalent with increased treatment times (Figure 5.5B-D).

Image analysis revealed clear evidence of aggregate region area and site frequency reductions with UVO treatment but a minimal effect of increased treatment time (Figure 5.6A-B). Qualitative observations of aggregate coating domains (Figure 5.6C) revealed an increasing divergence from a circular morphology (i) into more outstretched configurations (ii) with increased treatment time. Image processing of the diffused areas revealed that a greater number of diffuse crystals with lower length-width ratio were present on the untreated balloon surface, and these ratios increased with treatment time (Figure 5.5D). Additional characterization of aggregate domains showed that island sizes were higher on

the untreated surface and size decreased with treatment time (Figure 5.5E). The aggregate crystal excluded area (represented by two typical cases in Figure 5.5C) was higher for the UVO-treated case than the untreated case, indicating that the crystal aggregates formed a more uniform distribution in the case of the untreated cases, with more dispersion of aggregate domains with increased treatment time (Figure 5.5F).

5.4.4 Coating stability and acute PTX transfer

UVO treatment did not cause any systematic and significant changes in the amount of retained PTX after static submersion (Figure 5.7A). However, the amount of acutely transferred PTX to the vessel wall following simulated DCB deployment increased by ~400% ($p<0.05$) in the 20-min UVO-treated case as compared to the untreated case (Figure 5.7B). Additional UVO treatment time resulted in no further increase in acute drug transfer.

5.4.5 Response variable correlations

Correlations analyses revealed numerous strong relations among obtained biophysical response variables (Figure 5.8). Static contact angle and diffuse coating fraction exhibited a negative correlation, suggesting that increasing surface hydrophilicity diminished aggregate region formation. A negative correlation was also observed between contact angle and PTX transfer, linking increasing hydrophilicity to enhanced PTX delivery efficiency.

5.5 DISCUSSION

Endovascular therapy using DCBs is undergoing additional recent scrutiny. While several clinical trials have demonstrated DCB efficacy by performing head-to-head comparison with plain balloon angioplasty [147,165,180], and noninferiority with respect to

stent-based counterparts [167,181], recent findings on late-stage mortality for all PTX-containing devices have derailed the clinical momentum of DCB therapies [168,182]. It is now incumbent upon the scientific community to provide better characterization of this therapeutic modality, both in terms of elucidating functional mechanisms and providing strategies for improved device design. As such, there is extensive focus on identifying novel excipients to load the drug on the balloon catheter before the angioplasty procedure [180,183]. Note that this portion of research is increasingly attractive for device manufacturers to claim intellectual property. On the other hand, several studies have also focused on post-procedural mechanisms to better quantify arterial drug transport, tissue binding, and drug retention [30,184]. However, there is limited focus on the peri-procedural factors that determine DCB efficacy, and we do not fully understand how to optimize the transfer of a lipophilic drug such as PTX in combination with an excipient, which is generally hydrophilic, to the vessel wall within a short procedural time. In this work, we focused on developing a methodology that allows for enhanced drug transfer from the balloon catheter to the vessel wall.

Strategies that alter tissue-material interactions upon DCB deployment, including the presently considered balloon UVO-treatment strategy, can be potentially beneficial under at least two distinct scenarios. First, enhancing local contact pressures and adhesion with the vessel wall would promote post-procedural coating retention near/within the targeted lesion, which potentiates sustained drug delivery via late release from transferred coating material. Urea-based coatings, by virtue of their microstructural features, promote such interactions and therefore warrant continued consideration for DCB design [39]. Second, increasing the efficiency of acute PTX delivery with balloon/constituent modification, as

observed with UVO treatment, enables a reduction in requisite initial drug loading an insomuch limits the risk of systemic toxicity. UVO-treated, urea-based coatings thus show potential to enhance DCB efficacy in both scenarios, which motivates their further consideration in pre-clinical and eventually clinical studies.

Our study suggests key structure-property-function relations that underly DCB performance, and that these relations can be favorably altered via UVO treatment of the balloon surface. Specifically, we expect that UVO treatment increases to the presence of oxygen-containing balloon surface chemical species, which in turn increases the hydrophilicity of the surface and alters the microstructure of subsequently applied coating material. The general change in the microstructure can be characterized as a dispersion of coating material, which from a functional perspective increases the contact area with the arterial vessel and thus enhances diffusion of drug into the vessel wall during DCB deployment. Additionally, UVO treatment of the balloon surface, in addition to the manifest potential for enhancing acute PTX delivery, is also a standard method for removing surface contaminants and thus could aid in device sterilization [185]. Moreover, UVO treatment is inexpensive, simple-to-use, and could be easily incorporated into device preparation.

Our study has the following limitations that should be considered. Although suggested by previous studies with urea-based coatings, we did not examine if UVO treatment alters adhesive interactions of the coating and the arterial wall and ultimately coating transfer. Rather, we focused on developing a strategy to enhance acute drug transfer, which as mentioned is not the sole determinant of device efficacy. We did not directly analyze the changes in balloon surface chemistry that occur as a result of UVO

treatment, but did assess the change in a key surface property (hydrophilicity) – attenuated total reflectance Fourier transform infrared spectroscopy (FTIR) could be performed in future studies to address this limitation. Finally, we did not examine if the enhanced acute PTX transfer impacts long-term drug concentrations in the arterial wall and retention at the lesion site – subsequent in-vivo studies will provide insight into this critical aspect of DCB evaluation.

In conclusion, our study examines a translational method of altering the surface properties of the balloon catheter to enhance acute transfer of PTX to the arterial vessel. We showed that UVO treatment significantly decreased hydrophobicity of a canonical balloon material, which promoted more uniform and diffuse formation of a urea-based, drug-containing coating. Under simulated conditions of balloon angioplasty, there was a significant increase in acute transfer of the PTX from the balloon to the arterial vessel. Further studies are required to determine if UVO treatment of the balloon could lead to long-term clinical benefit in the context of DCBs.

5.6 ACKNOWLEDGMENTS

This work was supported by the American Heart Association through a Scientist Development Grant [17SDG33670323 to V.B.K]; the Hariri Institute for Computing and Computational Science & Engineering at Boston University through a Research Award to V.B.K; the Whitaker Cardiovascular Institute at Boston University School of Medicine through a pilot grant award to V.B.K; NIH INBRE Grant for South Carolina [P20GM103499 to T.S.].

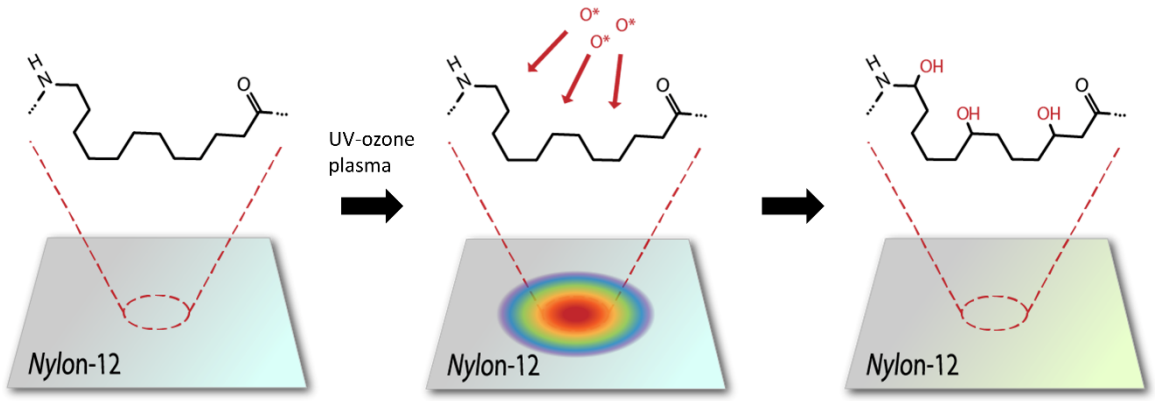

Figure 5.1: UVO treatment of Nylon-12 films.
Material samples were placed in a commercial UVO surface cleaner. Oxygen-based functional groups were added to the polymer molecules present on the Nylon-12 films by exposing them to atomic oxygen in the chamber.

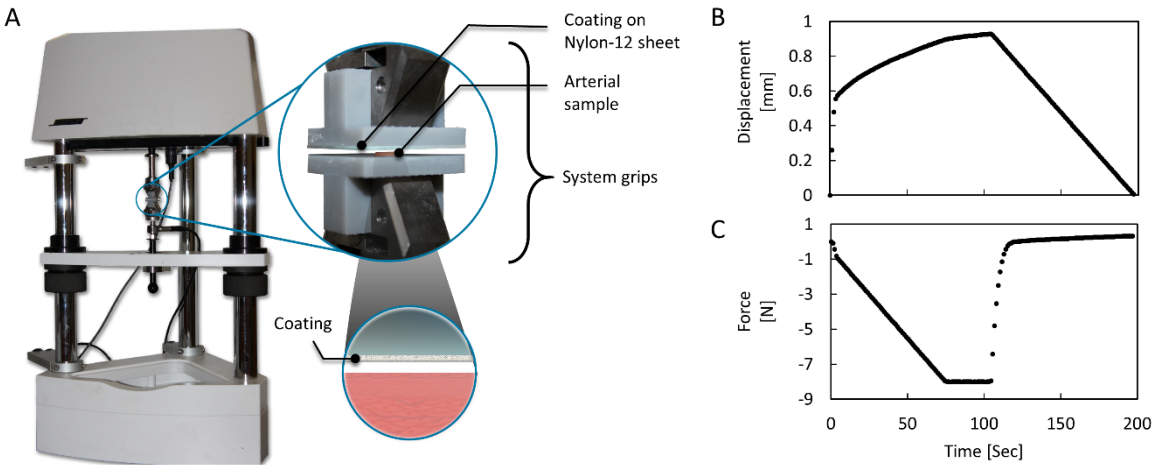

Figure 5.2: Experimental setup design for simulated DCB deployment.
(A) A uniaxial mechanical testing system was utilized to set the interface between arterial sample and DCB specimens. The system enables automated application of a compression-dwell-decompression protocol, as exemplified by the (B) displacement and (C) compressive force response curves.

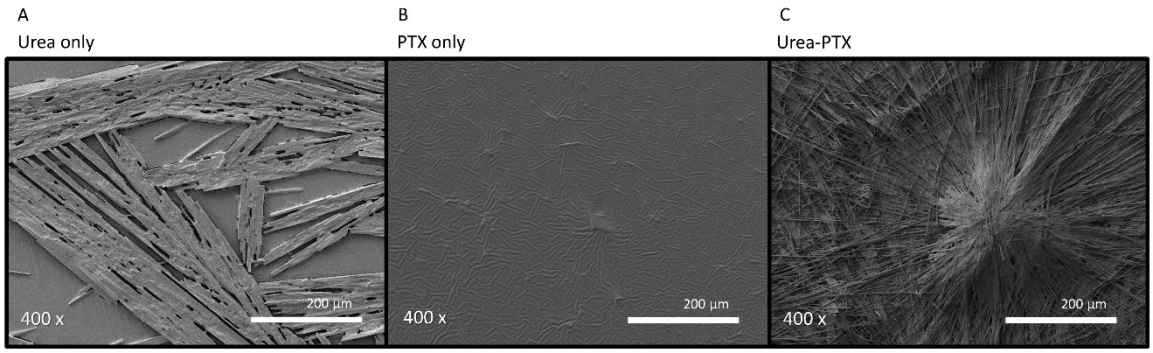

Figure 5.3: Microstructure of coating constituents.
SEM was used to examine the balloon surface coated with (A) urea only, (B) PTX only, and (C) PTX-urea. Images were taken at 400x magnification.

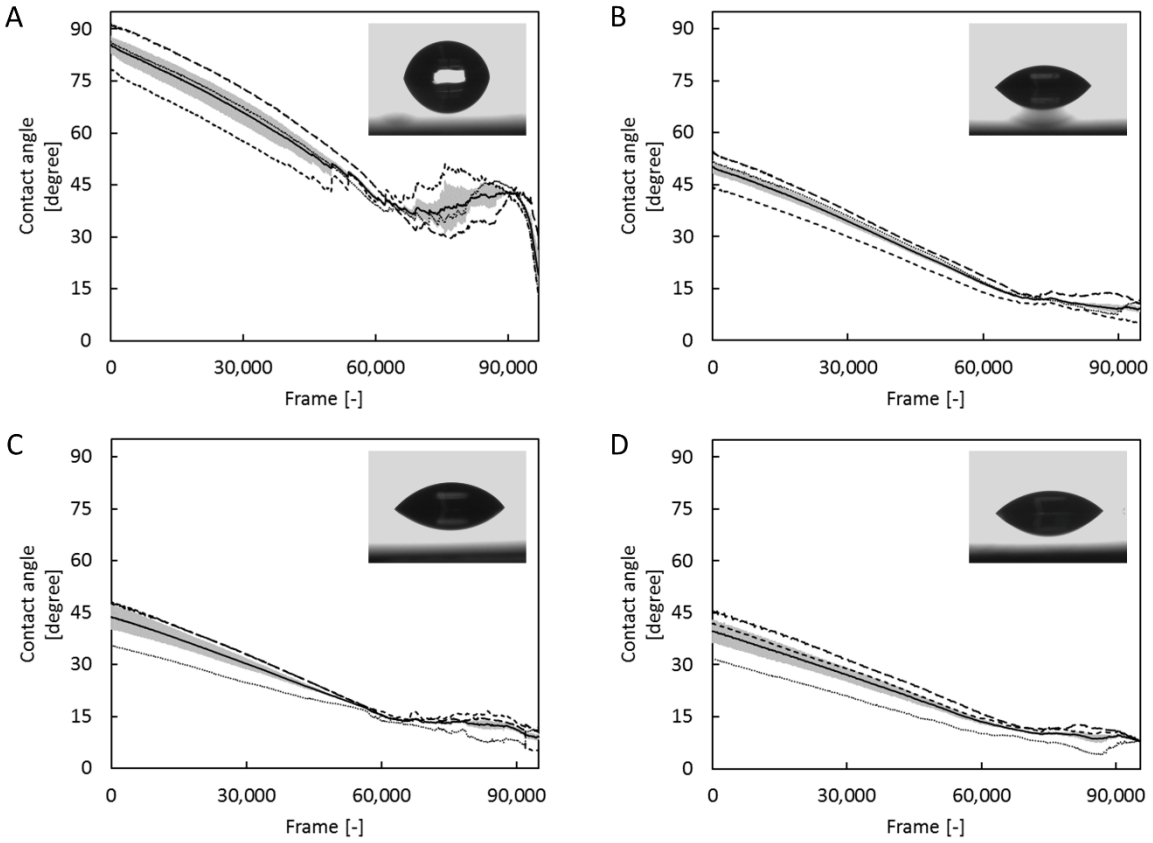

Figure 5.4: Contact angle measurement.
Dynamic contact angle of a sessile distilled water drop placed on the balloon surface was measured. Four scenarios showing contact angle measurements of water drops placed on (A) untreated Nylon-12 film, as well as UVO-treated Nylon-12 with (B) 20 min, (C) 40 min and (D) 60 min treatment times. Outputs from three independent trials (dotted lines) along with the average output (solid line), computed from these trials are shown. The inserts depict the drop profile for the first measured frame.

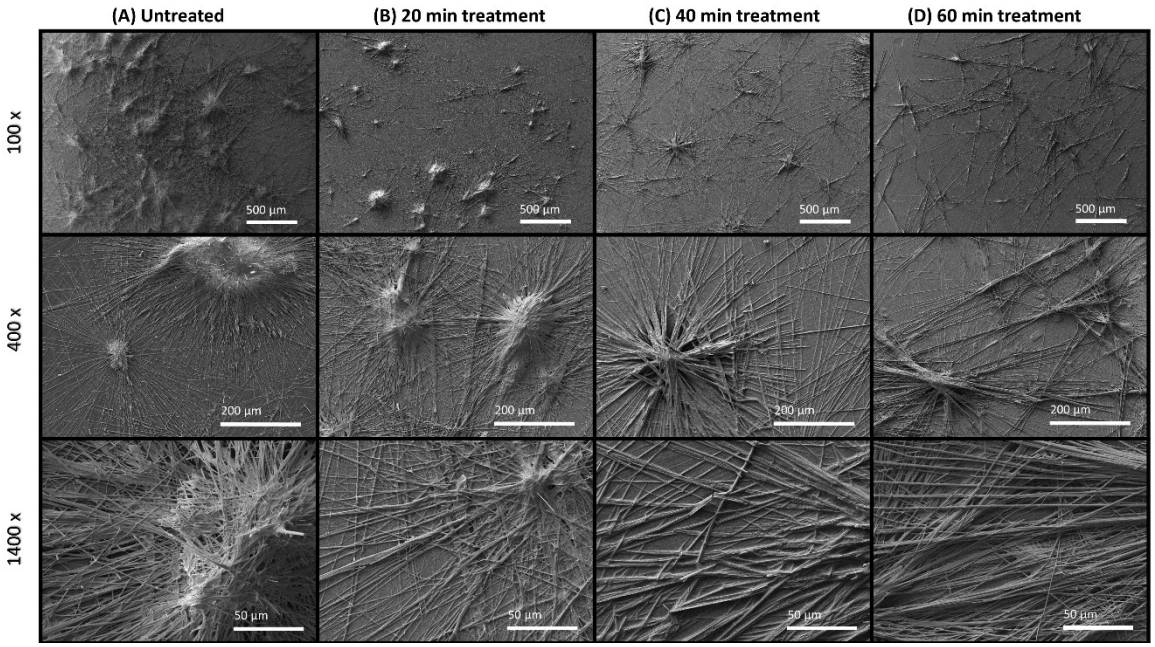

Figure 5.5: Coating microstructure changes due to surface modification.
SEM was used to examine the change in microstructure of the balloon surfaces due to UVO treatment. Four scenarios showing urea-PTX coatings on an (A) untreated balloon surface as well as UVO-treated Nylon-12 film with (B) 20 min, (C) 40 min, and (D) 60 min treatment times. Images taken at three different magnifications (100x, 400x and 1400x) are shown.

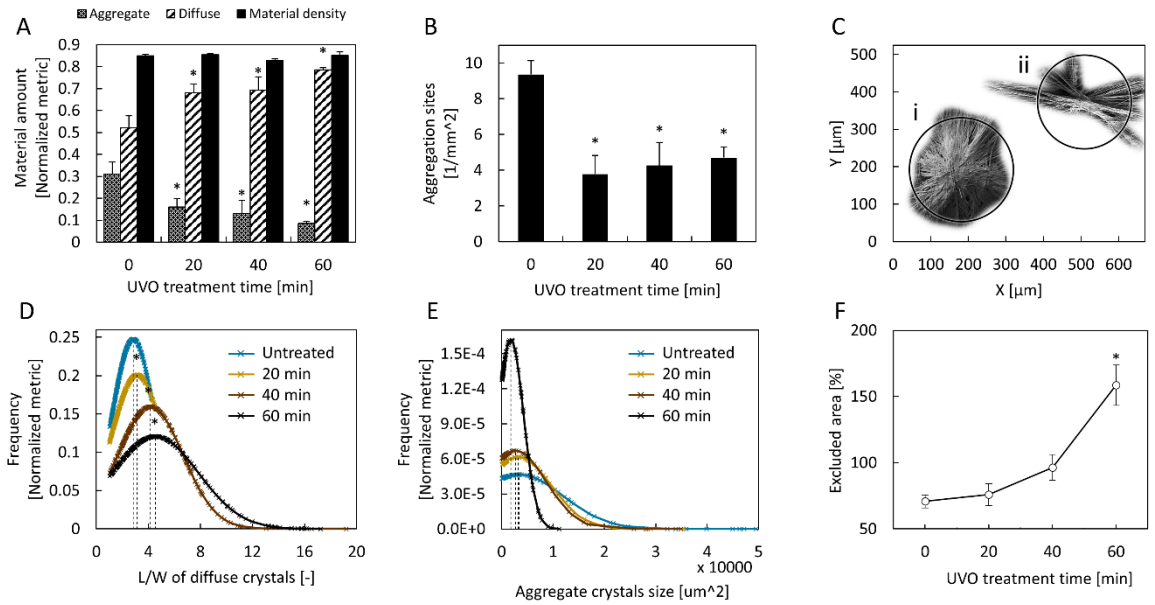

Figure 5.6: Morphological analysis of the coatings.
(A) Amount of material in aggregate and diffuse form quantified with binarization and crystal size-based thresholding with respect to UVO treatment time. Bars shown in black

denote the total coating material density comprised of diffuse and aggregate material (n=4, *denotes statistical significance with respect to untreated, $p<0.05$). (B) Number of aggregation sites per unit area with respect to UVO treatment time (n=4, *denotes statistical significance with respect to untreated, $p<0.05$). (C) Two representative aggregate crystals are shown for untreated (i) and UVO treated DCB for 60 min (ii) with equivalent circles placed at the center of gravity. (D) Distribution of length/width parameter for diffuse crystals with respect to UVO treatment times. (E) Distribution of aggregate crystal size with respect to UVO treatment times. (F) Aggregate crystal excluded area with respect to the equivalent circle (shown in panel C for two typical crystals) with respect to UVO treatment time (n=4, *denotes statistical significance with respect to untreated, $p<0.05$). (For interpretation of the references to color in this figure legend, the reader is referred to the Web version of this article.)

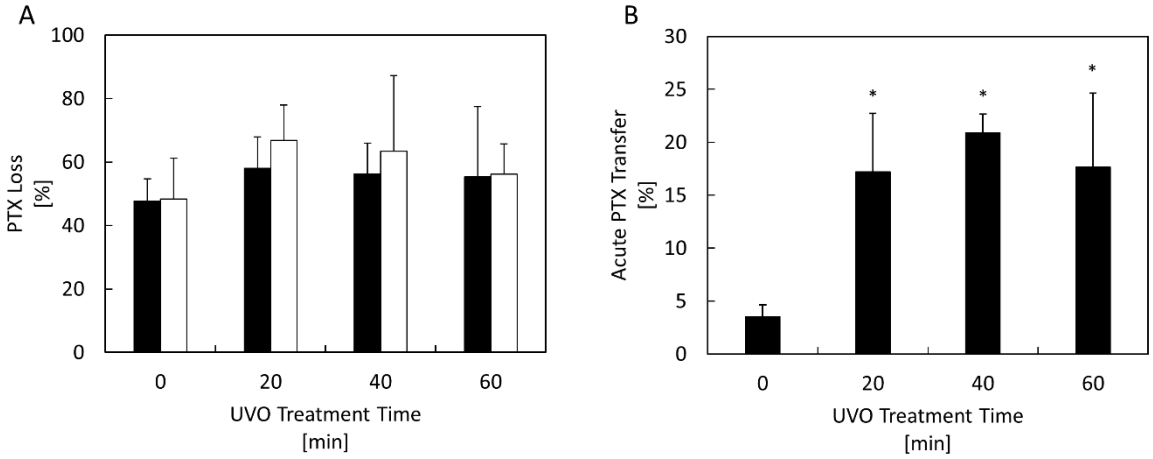

Figure 5.7: Estimation of drug delivery efficiency.
(A) PTX loss from urea-PTX coatings following 30 sec and 3 min static submersion times. (B) Acute drug transfer to the arterial wall following simulated DCB deployment (n=4, *denotes statistical significance with respect to untreated, $p<0.05$).

		Hydrophilicity	Coating morphology		Drug stability	Functionality
		Static contact angle	Diffuse coating fraction	Aggregate size	PTX loss	Acute PTX transfer
Hydrophilicity	Static contact angle	1	-0.96*	0.94	-0.90	-0.97*
Coating morphology	Diffuse coating fraction		1	-0.79*	0.79	0.86
	Aggregate size			1	-0.99*	-0.96*
Drug stability	PTX loss				1	0.93
Functionality	Acute PTX transfer					1

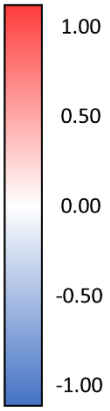

Figure 5.8: Correlation among biophysical response variables.
Pearson's correlation coefficients developed with mean values of response variables obtained across all urea-PTX coating variants. (* denotes statistical significance between variables, $p<0.05$). (For interpretation of the references to color in this figure legend, the reader is referred to the Web version of this article.)

CHAPTER 6

DISSERTATION SUMMARY AND CONCLUSION

6.1 MAJOR CONTRIBUTIONS TO THE FIELD

The work discussed in this doctoral dissertation is focused on the role of geometrical features in study of vascular disease severity, advancing clinical decision-making process and analysis of a drug delivery device to improve treatment effectiveness of a minimally-invasive endovascular procedure. These studies, firstly, will provide a nearly representative framework to understand effects of geometric variables on biophysics of the simulated phenomenon; Secondly, develop prediction models that are built on geometric parameters to estimate stress-based disease progression risk which is translationally applicable to clinical practice and can improve current clinical routines and outcomes; Finally, find association between intrinsic endovascular device coating geometry and therapy efficacy with an objective of optimizing drug device design by utilizing discovered associations between studied variables.

6.2 FUTURE WORKS

Study of geometric features in vascular disease-related conduit abnormalities, such as topics presented in chapters 2 and 3, motivates considering patient-specific scenarios, since disease progression and severity may vary with cases considerably. An immediate next step for these studies is to expand upon treatment technologies. In the case of AAA,

future work may utilize the previously developed parametric CAD platform to simulate aneurysmal scenarios and study structural mechanics with addition of an implant, e.g. stent graft. Given the regional heterogenous geometry and material properties, it is anticipated that a common stent graft - an endovascular intervention technology – will alter structural stress levels at high risk areas by application of new boundary conditions at stent anchors. Therefore, further investigation in this field may result in developing stent graft or stent anchor designs that are inspired and are specific to a set of aneurysmal scenarios, if not strictly patient-specific.

Furthermore, the studies regarding the DCB therapy, presented in previous chapters, investigated current challenges of an existing endovascular technology found correlation between key design and procedural variables to maximize acute drug transfer. The reasonably anticipated following study, covered in chapter 5, intended to propose and evaluate a method to utilize established correlations to produce systematic and repeatable changes in coating and subsequently, drug transfer. Nevertheless, the proposed methodology can be further studied to verify added value in comparison to current practices in the following disciplines: (1) biocompatibility; (2) wash-off during tracking; (3) post-deployment wash-off; (4) drug uptake (vs. acute transfer). We have performed an initial surface chemistry analysis to understand how UVO-caused changes to surface functional groups. To that end, X-ray photoelectron spectroscopy (XPS) was used for uncoated DCB specimens prior to and following UVO. XPS irradiates the sample surface with an x-ray beam in a vacuum chamber, and can identify chemical elements and bonds between these elements [186,187]. Our preliminary results show that UVO not only generates oxygen-based species at the surface but also breaks some C-C and C-N bonds (Figure 6.1). Deconvoluted

peaks and assignment of features for two carbon charging (C 1s) spectra (untreated and 20 min UVO) are shown in Figure 6.1C-D. Increase of balloon surface hydrophilicity (discussed in chapter 5) as a result of UVO treatment, can be mainly attributed to oxygenation of Nylon 12 via formation of polar hydroxyl, carbonyl and carboxylic acid functional groups (Figure 6.1). For treated samples, we noticed a new peak attributed to formation of carbonates (Figure 6.1D). Since carbonates are active ions, more work in this field is necessary to evaluate biocompatibility and/or develop reaction protocols to remove these ions. Additionally, biocompatibility studies should be conducted to further investigate C-N bond breakdown effects and whether this process will result in NOx generations. Together, these additional assays can help further developing UVO treatment as a biocompatible, safe and feasible procedure in commercial production of DCB.

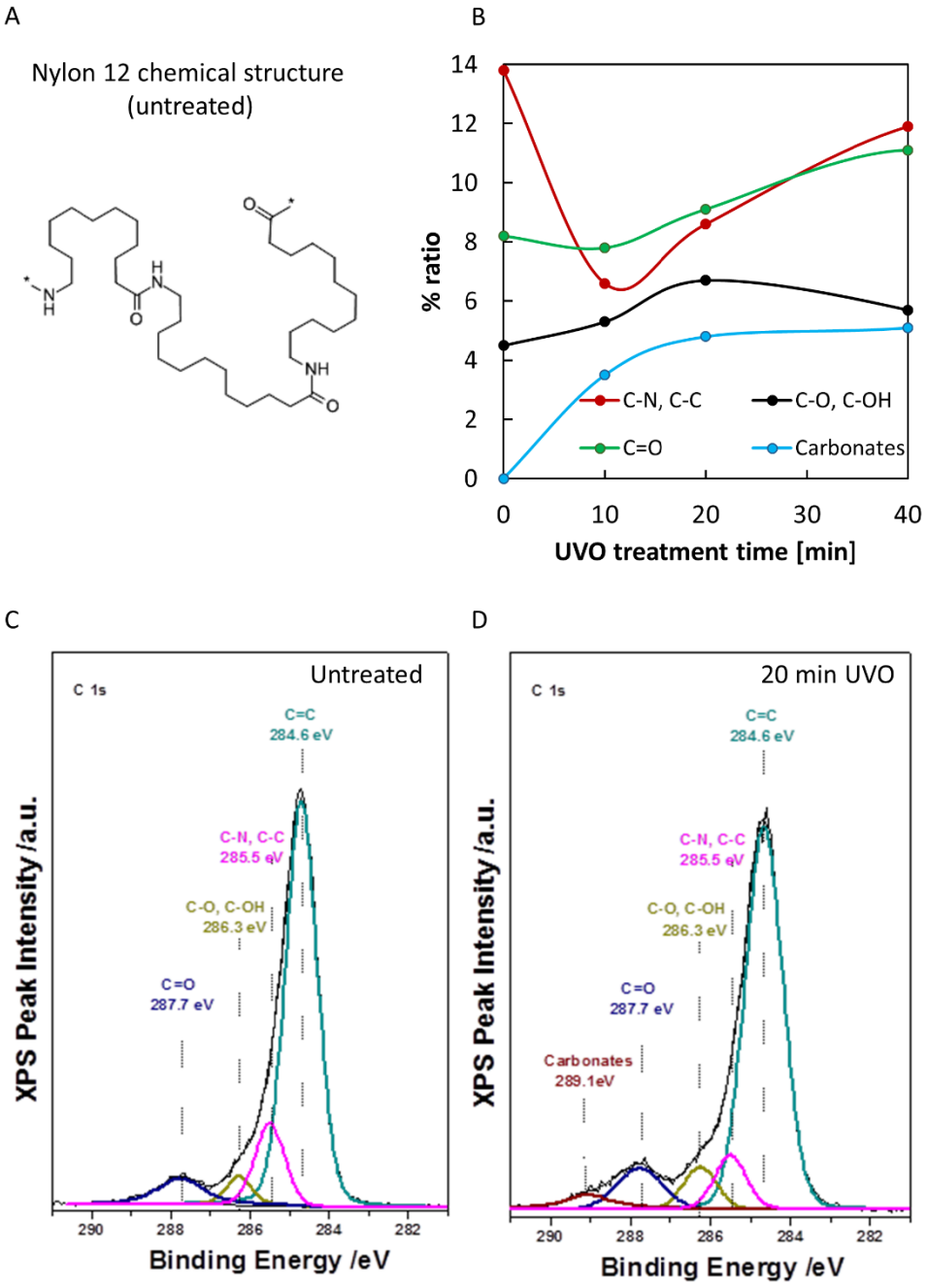

Figure 6.1: Nylon 12 structure and XPS analysis of UVO surface treatment.
(A) Nylon 12 chemical structure is shown, (B) effect of UVO irradiation time on carbon bonds is acquired after deconvolution and quantification of C 1s spectra. (C) X-ray photoelectron spectrum and deconvoluted peaks are shown for - untreated Nylon 12 film. (D) – UVO-treated Nylon 12 after being treated for 20 minutes. (For interpretation of the references to color in this figure legend, the reader is referred to the Web version of this article.)

REFERENCES

1. Mendis S, Puska P, Norrving B, World Health Organization., World Heart Federation., World Stroke Organization. *Global Atlas on Cardiovascular Disease Prevention and Control*. World Health Organization in collaboration with the World Heart Federation and the World Stroke Organization; 2011.

2. Jadidi M, Desyatova A, MacTaggart J, Kamenskiy A. Mechanical stresses associated with flattening of human femoropopliteal artery specimens during planar biaxial testing and their effects on the calculated physiologic stress–stretch state. *Biomech Model Mechanobiol*. 2019;18(6):1591-1605. doi:10.1007/s10237-019-01162-0

3. Nichols GA, Bell TJ, Pedula KL, O'Keeffe-Rosetti M. Medical care costs among patients with established cardiovascular disease. *Am J Manag Care*. 2010;16(3):e86-e93. http://www.ncbi.nlm.nih.gov/pubmed/20205493. Accessed March 6, 2019.

4. Hirsch AT, Criqui MH, Treat-Jacobson DJ, et al. Peripheral arterial disease detection, awareness, and treatment in primary care. *Jama*. 2001;286(11):1317-1324. doi:joc11056 [pii]

5. Sternberg K, Grabow N, Petersen S, et al. Advances in Coronary Stent Technology - Active Drug-Loaded Stent Surfaces for Prevention of Restenosis and Improvement of Biocompatibility. *Curr Pharm Biotechnol*. 2013;14(1):76-90. doi:10.2174/1389201011314010011

6. Koskas F, Kieffer E. Long-term survival after elective repair of infrarenal abdominal aortic aneurysm: results of a prospective multicentric study. Association for Academic Research in Vascular Surgery (AURC). *Ann Vasc Surg*. 1997;11(5):473-481.

7. Liapis CD, Bell SPRF, Mikhailidis D, et al. ESVS Guidelines. Invasive Treatment for Carotid Stenosis: Indications, Techniques. *Eur J Vasc Endovasc Surg*. 2009;37(4):1-19. doi:10.1016/J.EJVS.2008.11.006

8. S. Celi, S. Berti, M. Mariani, F. Di Puccio, P. Forte. Investigation on the effect of the wall thickness in rupture risk estimation of aaa by a probabilistic finite element approach. *Eur Heart J*. 2010;31(1):284.

9. Chaikof EL. Caring for patients with an abdominal aortic aneurysm: Data, knowledge, and wisdom. *J Vasc Surg*. 2009;50(4 SUPPL.):S1. doi:10.1016/j.jvs.2009.07.020

10. Sharzehee M, Khalafvand SS, Han H-C. Fluid-structure interaction modeling of aneurysmal arteries under steady-state and pulsatile blood flow: a stability analysis. *Comput Methods Biomech Biomed Engin*. 2018;21(3):219-231. doi:10.1080/10255842.2018.1439478

11. Dobrin PB. Pathophysiology and pathogenesis of aortic aneurysms. Current concepts. *Surg Clin North Am*. 1989;69(4):687-703. doi:10.1016/s0039-6109(16)44876-0

12. Jadidi M, Habibnezhad M, Anttila E, et al. Mechanical and structural changes in human thoracic aortas with age. *Acta Biomater*. 2020;103:172-188. doi:10.1016/j.actbio.2019.12.024

13. Stather PW, Sidloff DA, Rhema IA, Choke E, Bown MJ, Sayers RD. A review of current reporting of abdominal aortic aneurysm mortality and prevalence in the literature. *Eur J Vasc Endovasc Surg*. 2014;47(3):240-242. doi:10.1016/j.ejvs.2013.11.007

14. Darling RC, Messina CR, Brewster DC, Ottinger LW. Autopsy study of unoperated abdominal aortic aneurysms. The case for early resection. *Circulation*. 1977;56(3 Suppl):II161-4.

15. Kubicek L, Staffa R, Novotny T, et al. Abdominal Aortic Aneurysm Rupture Risk Prediction Based on Computer-aided Vascular Wall Stress Assessment Using Finite Element Method – The Future of Decision Making Process. *Eur J Vasc Endovasc Surg*. 2019;58(6):e306-e307. doi:10.1016/j.ejvs.2019.06.915

16. Morris DR, Ayabe K, Inoue T, et al. Evidence-Based Carotid Interventions for Stroke Prevention: State-of-the-art Review. *J Atheroscler Thromb*. 2017;24(4):373-387. doi:10.5551/jat.38745

17. Sharzehee M, Fatemifar F, Han HC. Computational simulations of the helical buckling behavior of blood vessels. *Int j numer method biomed eng*. 2019;35(12). doi:10.1002/cnm.3277

18. Sousa LC, Castro CF, António CC, et al. Computational simulation of carotid stenosis and flow dynamics based on patient ultrasound data – A new tool for risk assessment and surgical planning. *Adv Med Sci*. 2016;61(1):32-39. doi:10.1016/j.advms.2015.07.009

19. Jahromi R, Pakravan HA, Saidi MS, Firoozabadi B. Primary stenosis progression versus secondary stenosis formation in the left coronary bifurcation: A mechanical point of view. *Biocybern Biomed Eng*. 2019;39(1):188-198. doi:10.1016/j.bbe.2018.11.006

20. Samaee M, Tafazzoli-Shadpour M, Alavi H. Coupling of shear–circumferential stress pulses investigation through stress phase angle in FSI models of stenotic artery using experimental data. *Med Biol Eng Comput*. 2017;55(8):1147-1162. doi:10.1007/s11517-016-1564-z

21. Texakalidis P, Giannopoulos S, Kokkinidis DG, Jabbour P, Reavey-Cantwell J, Rangel-Castilla L. Outcome of Carotid Artery Endarterectomy in Statin Users versus Statin-Naïve Patients: A Systematic Review and Meta-Analysis. *World Neurosurg*. 2018;116:444-450.e1. doi:10.1016/j.wneu.2018.05.160

22. Montorsi P, Galli S, Ravagnani PM, Roffi M. Symptomatic Carotid Artery Disease: Revascularization. *Prog Cardiovasc Dis*. 2017;59(6):601-611. doi:10.1016/j.pcad.2017.04.002

23. Long Q, Xu XY, Ariff B, Thom SA, Hughes AD, Stanton A V. Reconstruction of blood flow patterns in a human carotid bifurcation: A combined CFD and MRI study. *J Magn Reson Imaging*. 2000;11(3):299-311. doi:10.1002/(SICI)1522-2586(200003)11:3<299::AID-JMRI9>3.0.CO;2-M

24. Choi G, Lee JM, Kim H-J, et al. Coronary Artery Axial Plaque Stress and its Relationship With Lesion Geometry. *JACC Cardiovasc Imaging*. 2015;8(10):1156-1166. doi:10.1016/j.jcmg.2015.04.024

25. Thukkani AK, Kinlay S. Endovascular Intervention for Peripheral Artery Disease. *Circ Res*. 2015;116(9):1599-1613. doi:10.1161/CIRCRESAHA.116.303503

26. Shazly T, Kolachalama VB, Ferdous J, Oberhauser JP, Hossainy S, Edelman ER. Assessment of material by-product fate from bioresorbable vascular scaffolds. *Ann Biomed Eng*. 2012;40(4):955-965. doi:10.1007/s10439-011-0445-8

27. Sarode K, Spelber DA, Bhatt DL, et al. Drug Delivering Technology for Endovascular Management of Infrainguinal Peripheral Artery Disease. *JACC Cardiovasc Interv*. 2014;7:827-839. doi:10.1016/j.jcin.2014.05.008

28. Gongora CA, Shibuya M, Wessler JD, et al. Impact of Paclitaxel Dose on Tissue Pharmacokinetics and Vascular Healing: A Comparative Drug-Coated Balloon Study in the Familial Hypercholesterolemic Swine Model of Superficial Femoral In-Stent Restenosis. *JACC Cardiovasc Interv*. 2015;8(8):1115-1123. doi:10.1016/J.JCIN.2015.03.020

29. Yazdani SK, Pacheco E, Nakano M, et al. Vascular, downstream, and pharmacokinetic responses to treatment with a low dose drug-coated balloon in a swine femoral artery model. *Catheter Cardiovasc Interv*. 2014;83(1):132-140. doi:10.1002/ccd.24995

30. Kolachalama VB, Pacetti SD, Franses JW, et al. Mechanisms of Tissue Uptake and Retention in Zotarolimus-Coated Balloon Therapy. *Circulation*. 2013;127(20):2047-2055. doi:10.1161/CIRCULATIONAHA.113.002051

31. Gray WA, Granada JF. Drug-Coated Balloons for the Prevention of Vascular Restenosis. *Circulation*. 2010;121(24):2672-2680. doi:10.1161/CIRCULATIONAHA.110.936922

32. Granada JF, Stenoien M, Buszman PP, et al. Mechanisms of tissue uptake and retention of paclitaxel-coated balloons: impact on neointimal proliferation and healing. *Open Hear*. 2014;1(1):e000117. doi:10.1136/openhrt-2014-000117

33. Byrne RA, Joner M, Alfonso F, Kastrati A. Drug-coated balloon therapy in coronary and peripheral artery disease. *Nat Rev Cardiol*. 2014;11(1):13-23. doi:10.1038/nrcardio.2013.165

34. Waksman R, Pakala R. Drug-Eluting Balloon: The Comeback Kid? *Circ Cardiovasc Interv*. 2009;2(4):352-358. doi:10.1161/CIRCINTERVENTIONS.109.873703

35. De Labriolle A, Pakala R, Bonello L, Lemesle G, Scheinowitz M, Waksman R. Paclitaxel-eluting balloon: From bench to bed. *Catheter Cardiovasc Interv*. 2009;73(5):643-652. doi:10.1002/ccd.21895

36. Heilmann T, Richter C, Noack H, et al. Drug Release Profiles of Different Drug-coated Balloon Platforms. *Eur Cardiol Rev*. 2010;6(4):40. doi:10.15420/ECR.2010.8.2.40

37. Azar D, Ohadi D, Rachev A, Eberth JF, Uline MJ, Shazly T. Mechanical and geometrical determinants of wall stress in abdominal aortic aneurysms: A computational study. Tang D, ed. *PLoS One*. 2018;13(2):e0192032. doi:10.1371/journal.pone.0192032

38. Azar D, Torres WM, Davis LA, et al. Geometric determinants of local hemodynamics in severe carotid artery stenosis. *Comput Biol Med*. 2019;114:103436. doi:10.1016/j.compbiomed.2019.103436

39. Chang GH, Azar DA, Lyle C, Chitalia VC, Shazly T, Kolachalama VB. Intrinsic coating morphology modulates acute drug transfer in drug-coated balloon therapy. *Sci Rep*. 2019;9(1):6839. doi:10.1038/s41598-019-43095-9

40. Azar D, Lott JT, Jabbarzadeh E, Shazly T, Kolachalama VB. Surface Modification Using Ultraviolet-Ozone Treatment Enhances Acute Drug Transfer in Drug-Coated Balloon Therapy. *Langmuir*. April 2020:acs.langmuir.0c00298. doi:10.1021/acs.langmuir.0c00298

41. Timaran CH, Veith FJ, Rosero EB, et al. Endovascular aortic aneurysm repair in patients with the highest risk and in-hospital mortality in the United States. *Arch Surg*. 2007;142(6):520-525. doi:10.1001/archsurg.142.6.520

42. Vandy F, Upchurch GRJ. Endovascular aneurysm repair: current status. *Circ Cardiovasc Interv*. 2012;5(6):871-882. doi:10.1161/CIRCINTERVENTIONS.111.966184

43. Uchida N. Open stent grafting for complex diseases of the thoracic aorta: Clinical utility. *Gen Thorac Cardiovasc Surg*. 2013;61(3):118-126. doi:10.1007/s11748-012-0151-y

44. Hinterseher I, Kuffner H, Berth H, et al. Long-term quality of life of abdominal aortic aneurysm patients under surveillance or after operative treatment. *Ann Vasc Surg*. 2013;27(5):553-561. doi:10.1016/j.avsg.2012.05.028

45. Aljabri B, Al Wahaibi K, Abner D, et al. Patient-reported quality of life after abdominal aortic aneurysm surgery: a prospective comparison of endovascular and open repair. *J Vasc Surg*. 2006;44(6):1182-1187. doi:10.1016/j.jvs.2006.08.015

46. United Kingdom Small Aneurysm Trial Participants. Long-Term Outcomes of Immediate Repair Compared with Surveillance of Small Abdominal Aortic Aneurysms. *N Engl J Med*. 2002;346(19):1445-1452. doi:10.1056/NEJMoa013527

47. Lund GB, Trerotola SO, Scheel PJJ. Percutaneous translumbar inferior vena cava cannulation for hemodialysis. *Am J Kidney Dis*. 1995;25(5):732-737.

48. Ruddy JM, Jones JA, Ikonomidis JS. Pathophysiology of thoracic aortic aneurysm (TAA): is it not one uniform aorta? Role of embryologic origin. *Prog Cardiovasc Dis*. 2013;56(1):68-73. doi:10.1016/j.pcad.2013.04.002

49. Nordon IM, Hinchliffe RJ, Loftus IM, Thompson MM. Pathophysiology and epidemiology of abdominal aortic aneurysms. *Nat Rev Cardiol*. 2011;8(2):92-102. doi:10.1038/nrcardio.2010.180

50. Meijer CA, Stijnen T, Wasser MNJM, Hamming JF, van Bockel JH, Lindeman JHN. Doxycycline for stabilization of abdominal aortic aneurysms: a randomized trial. *Ann Intern Med*. 2013;159(12):815-823. doi:10.7326/0003-4819-159-12-201312170-00007

51. Baxter BT, Terrin MC, Dalman RL. Medical management of small abdominal aortic aneurysms. *Circulation*. 2008;117(14):1883-1889. doi:10.1161/CIRCULATIONAHA.107.735274

52. Kent KC, Zwolak RM, Jaff MR, et al. Screening for abdominal aortic aneurysm: a consensus statement. *J Vasc Surg*. 2004;39(1):267-269. doi:10.1016/j.jvs.2003.08.019

53. Stroupe KT, Lederle FA, Matsumura JS, et al. Cost-effectiveness of open versus endovascular repair of abdominal aortic aneurysm in the OVER trial. *J Vasc Surg*. 2012;56(4):901-9.e2. doi:10.1016/j.jvs.2012.01.086

54. Danyi P, Elefteriades JA, Jovin IS. Medical therapy of thoracic aortic aneurysms. *Trends Cardiovasc Med*. 2012;22(7):180-184. doi:10.1016/j.tcm.2012.07.017

55. Sharma AK, Lu G, Jester A, et al. Experimental abdominal aortic aneurysm formation is mediated by IL-17 and attenuated by mesenchymal stem cell treatment. *Circulation*. 2012;126(11 Suppl 1):S38-45. doi:10.1161/CIRCULATIONAHA.111.083451

56. BC Weiford. *Braunwald's Heart Disease*. Vol 294.; 2005.

57. Humphrey JD. *Cardiovascular Solid Mechanics: Cells, Tissues, and Organs*. Springer New York; 2013. https://books.google.com/books?id=gwbSBwAAQBAJ.

58. Georgakarakos E, Ioannou C V, Kamarianakis Y, et al. The Role of Geometric Parameters in the Prediction of Abdominal Aortic Aneurysm Wall Stress. *Eur J Vasc Endovasc Surg*. 2010;39(1):42-48. doi:10.1016/j.ejvs.2009.09.026

59. Giannoglou G, Giannakoulas G, Soulis J, et al. Predicting the Risk of Rupture of Abdominal Aortic Aneurysms by Utilizing Various Geometrical Parameters: Revisiting the Diameter Criterion. *Angiology*. 2006;57(4):487-494. doi:10.1177/0003319706290741

60. Chauhan SS, Gutierrez CA, Thirugnanasambandam M, et al. The Association Between Geometry and Wall Stress in Emergently Repaired Abdominal Aortic Aneurysms. *Ann Biomed Eng*. 2017;45(8):1908-1916. doi:10.1007/s10439-017-1837-1

61. Raghavan ML, Kratzberg J, Castro de Tolosa EM, Hanaoka MM, Walker P, da Silva ES. Regional distribution of wall thickness and failure properties of human abdominal aortic aneurysm. *J Biomech*. 2006;39(16):3010-3016. doi:10.1016/j.jbiomech.2005.10.021

62. Gasser TC, Auer M, Labruto F, Swedenborg J, Roy J. Biomechanical rupture risk assessment of abdominal aortic aneurysms: Model complexity versus predictability of finite element simulations. *Eur J Vasc Endovasc Surg*. 2010;40(2):176-185. doi:10.1016/j.ejvs.2010.04.003

63. Raghavan ML, Vorp DA, Federle MP, Makaroun MS, Webster MW. Wall stress distribution on three-dimensionally reconstructed models of human abdominal aortic aneurysm. *J Vasc Surg*. 2000;31(4):760-769. doi:10.1067/mva.2000.103971

64. Vorp DA, Vande Geest JP. Biomechanical determinants of abdominal aortic aneurysm rupture. *Arterioscler Thromb Vasc Biol*. 2005;25(8):1558-1566. doi:10.1161/01.ATV.0000174129.77391.55

65. Fujikura K, Luo J, Gamarnik V, et al. A novel noninvasive technique for pulse-wave imaging and characterization of clinically-significant vascular mechanical properties in vivo. *Ultrason Imaging*. 2007;29(3):137-154. doi:10.1177/016173460702900301

66. Nanayakkara BG, Gunarathne CK, Sanjeewa A, Gajaweera KAR. Geometric anatomy of the aortic- common iliac bifurcation. *Gall Med J*. 2007;12(1):8-12.

67. Holzapfel GA, Gasser TC, Ogden RW. A new constitutive framework for arterial wall mechanics and a comparative study of material models. *J Elast*. 2000;61(1-3):1-48. doi:10.1023/A:1010835316564

68. Gasser TC, Ogden RW, Holzapfel G a. Hyperelastic modelling of arterial layers with distributed collagen fibre orientations. *J R Soc Interface*. 2006;3(6):15-35. doi:10.1098/rsif.2005.0073

69. Weisbecker H, Pierce DM, Regitnig P, Holzapfel GA. Layer-specific damage experiments and modeling of human thoracic and abdominal aortas with non-atherosclerotic intimal thickening. *J Mech Behav Biomed Mater*. 2012;12:93-106. doi:10.1016/j.jmbbm.2012.03.012

70. Pierce DM, Maier F, Weisbecker H, et al. Human thoracic and abdominal aortic aneurysmal tissues: Damage experiments, statistical analysis and constitutive modeling. *J Mech Behav Biomed Mater*. 2015;41:92-107. doi:10.1016/j.jmbbm.2014.10.003

71. Bottasso CL, Detomi D. A procedure for tetrahedral boundary layer mesh generation. *Eng Comput*. 2002;18(1):66-79. doi:10.1007/s003660200006

72. Tran AP, Fang Q. Fast and high-quality tetrahedral mesh generation from neuroanatomical scans. 2000:1-20.

73. Maas SA, Ellis BJ, Ateshian GA, Weiss JA. FEBio: Finite Elements for Biomechanics. *J Biomech Eng*. 2012;134(1):011005. doi:10.1115/1.4005694

74. Raghavan ML, Webster MW, Vorp DA. Ex vivo biomechanical behavior of abdominal aortic aneurysm: Assessment using a new mathematical model. *Ann Biomed Eng*. 1996;24(5):573-582. doi:10.1007/BF02684226

75. Roy D, Holzapfel GA, Kauffmann C, Soulez G. Finite element analysis of abdominal aortic aneurysms: Geometrical and structural reconstruction with application of an anisotropic material model. *IMA J Appl Math (Institute Math Its Appl*. 2014;79(5):1011-1026. doi:10.1093/imamat/hxu037

76. Stevens RRF, Grytsan A, Biasetti J, Roy J, Liljeqvist ML, Christian Gasser T. Biomechanical changes during abdominal aortic aneurysm growth. *PLoS One*. 2017;12(11). doi:10.1371/journal.pone.0187421

77. Fillinger MF, Raghavan ML, Marra SP, Cronenwett JL, Kennedy FE. In vivo analysis of mechanical wall stress and abdominal aortic aneurysm rupture risk. *J Vasc Surg*. 2002;36(3):589-597. doi:10.1067/mva.2002.125478

78. Fillinger M. Who Should We Operate On and How Do We Decide: Predicting Rupture and Survival in Patients with Aortic Aneurysm. *Semin Vasc Surg*. 2007;20(2):121-127. doi:10.1053/j.semvascsurg.2007.04.001

79. Vande Geest JP, Wang DHJ, Wisniewski SR, Makaroun MS, Vorp DA. Towards a noninvasive method for determination of patient-specific wall strength distribution in abdominal aortic aneurysms. *Ann Biomed Eng*. 2006;34(7):1098-1106. doi:10.1007/s10439-006-9132-6

80. Di Martino ES, Bohra A, Vande Geest JP, Gupta N, Makaroun MS, Vorp DA. Biomechanical properties of ruptured versus electively repaired abdominal aortic aneurysm wall tissue. *J Vasc Surg*. 2006;43(3):570-576. doi:10.1016/j.jvs.2005.10.072

81. Rodríguez JF, Ruiz C, Doblaré M, Holzapfel GA. Mechanical stresses in abdominal aortic aneurysms: influence of diameter, asymmetry, and material anisotropy. *J Biomech Eng*. 2008;130(2):021023. doi:10.1115/1.2898830

82. Raghavan ML, Vorp DA. Toward a biomechanical tool to evaluate rupture potential of abdominal aortic aneurysm: Identification of a finite strain constitutive model and evaluation of its applicability. *J Biomech*. 2000;33(4):475-482. doi:10.1016/S0021-9290(99)00201-8

83. Venkatasubramaniam AK, Fagan MJ, Mehta T, et al. A comparative study of aortic wall stress using finite element analysis for ruptured and non-ruptured abdominal aortic aneurysms. *Eur J Vasc Endovasc Surg*. 2004;28(2):168-176. doi:10.1016/j.ejvs.2004.03.029

84. Rissland P, Alemu Y, Einav S, Ricotta J, Bluestein D. Abdominal Aortic Aneurysm Risk of Rupture: Patient-Specific FSI Simulations Using Anisotropic Model. *J Biomech Eng*. 2009;131(3):031001. doi:10.1115/1.3005200

85. Dorfmann A, Wilson C, Edgar ES, Peattie RA. Evaluating patient-specific abdominal aortic aneurysm wall stress based on flow-induced loading. *Biomech Model Mechanobiol*. 2010;9(2):127-139. doi:10.1007/s10237-009-0163-4

86. Zarins CK, Xu C, Glagov S. Atherosclerotic enlargement of the human abdominal aorta. *Atherosclerosis*. 2001;155(1):157-164. doi:10.1016/S0021-9150(00)00527-X

87. Vorp DA. Biomechanics of abdominal aortic aneurysm. *J Biomech*. 2007;40(9):1887-1902. doi:10.1016/j.jbiomech.2006.09.003

88. Vorp DA, Raghavan ML, Webster MW. Mechanical wall stress in abdominal aortic aneurysm: Influence of diameter and asymmetry. *J Vasc Surg*. 1998;27(4):632-639. doi:10.1016/S0741-5214(98)70227-7

89. Doyle BJ, Callanan A, Burke PE, et al. Vessel asymmetry as an additional diagnostic tool in the assessment of abdominal aortic aneurysms. *J Vasc Surg*. 2009;49(2):443-454. doi:10.1016/j.jvs.2008.08.064

90. Scotti CM, Shkolnik AD, Muluk SC, Finol E a. Fluid-structure interaction in abdominal aortic aneurysms: effects of asymmetry and wall thickness. *Biomed Eng Online*. 2005;4(1):64. doi:10.1186/1475-925X-4-64

91. Del Corso L, Moruzzo D, Conte B, et al. Tortuosity, kinking, and coiling of the carotid artery: expression of atherosclerosis or aging? *Angiology*. 1998;49(5):361-371. doi:10.1177/000331979804900505

92. Sacks MS, Vorp DA, Raghavan ML, Federle MP, Webster MW. In vivo three-dimensional surface geometry of abdominal aortic aneurysms. *Ann Biomed Eng*. 1999;27(4):469-479.

93. Fillinger MF, Marra SP, Raghavan ML, Kennedy FE. Prediction of rupture risk in abdominal aortic aneurysm during observation: Wall stress versus diameter. *J Vasc Surg*. 2003;37(4):724-732. doi:10.1067/mva.2003.213

94. Papaharilaou Y, Ekaterinaris JA, Manousaki E, Katsamouris AN. A decoupled fluid structure approach for estimating wall stress in abdominal aortic aneurysms. *J Biomech*. 2007;40(2):367-377. doi:10.1016/j.jbiomech.2005.12.013

95. Pappu S, Dardik A, Tagare H, Gusberg RJ. Beyond Fusiform and Saccular: A Novel Quantitative Tortuosity Index May Help Classify Aneurysm Shape and Predict Aneurysm Rupture Potential. *Ann Vasc Surg*. 2008;22(1):88-97. doi:http://dx.doi.org/10.1016/j.avsg.2007.09.004

96. Giannakoulas G, Giannoglou G, Soulis J, et al. A computational model to predict aortic wall stresses in patients with systolic arterial hypertension. *Med Hypotheses*. 2005;65(6):1191-1195. doi:10.1016/j.mehy.2005.06.017

97. Vande Geest JP, Schmidt DE, Sacks MS, Vorp DA. The effects of anisotropy on the stress analyses of patient-specific abdominal aortic aneurysms. *Ann Biomed Eng*. 2008;36(6):921-932. doi:10.1007/s10439-008-9490-3

98. Coward LJ, Featherstone RL, Brown MM. Safety and efficacy of endovascular treatment of carotid artery stenosis compared with carotid endarterectomy: A cochrane systematic review of the randomized evidence. *Stroke*. 2005;36(4):905-911. doi:10.1161/01.STR.0000158921.51037.64

99. Naylor AR, Mehta Z, Rothwell PM, Bell PRF. Carotid Artery Disease and Stroke During Coronary Artery Bypass: a Critical Review of the Literature. *Eur J Vasc Endovasc Surg*. 2002;23:283-294. doi:10.1053/ejvs.2002

100. Pokras R, Dyken ML. Dramatic changes in the performance of endarterectomy for diseases of the extracranial arteries of the head. *Stroke*. 1988;19(10):1289-1290.

101. Kolachalama VB, Bressloff NW, Nair PB, Shearman CP. Predictive haemodynamics in a one-dimensional human carotid artery bifurcation. Part I: Application to stent design. *IEEE Trans Biomed Eng*. 2007;54(5):802-812. doi:10.1109/TBME.2006.889188

102. Leng X, Zhou B, Deng X, et al. Determination of Viscoelastic Properties of human Carotid Atherosclerotic Plaque by Inverse Boundary Value Analysis. *IOP Conf Ser Mater Sci Eng*. 2018;381:012171. doi:10.1088/1757-899X/381/1/012171

103. Merei B, Badel P, Davis L, Sutton MA, Avril S, Lessner SM. Atherosclerotic plaque delamination: Experiments and 2D finite element model to simulate plaque peeling in two strains of transgenic mice. *J Mech Behav Biomed Mater*. 2017;67:19-30. doi:10.1016/J.JMBBM.2016.12.001

104. Shahidian A, Hassankiadeh AG. Stress analysis of internal carotid artery with low stenosis level: the effect of material model and plaque geometry. *J Mech Med Biol*. 2017;17(06):1750098. doi:10.1142/S0219519417500981

105. Huang Y, Gloviczki P, Duncan AA, et al. Outcomes after early and delayed carotid endarterectomy in patients with symptomatic carotid artery stenosis. *J Vasc Surg*. 2018;67(4):1110-1119.e1. doi:10.1016/j.jvs.2017.09.021

106. Ricotta JJ, AbuRahma A, Ascher E, Eskandari M, Faries P, Lal BK. Updated Society for Vascular Surgery guidelines for management of extracranial carotid disease: Executive summary. *J Vasc Surg*. 2011;54(3):832-836. doi:10.1016/J.JVS.2011.07.004

107. Dabagh M, Vasava P, Jalali P. Effects of severity and location of stenosis on the hemodynamics in human aorta and its branches. *Med Biol Eng Comput*. 2015;53(5):463-476. doi:10.1007/s11517-015-1253-3

108. Kim BJ, Lee KM, Kim HY, et al. Basilar Artery Plaque and Pontine Infarction Location and Vascular Geometry. *J Stroke*. 2018;20(1):92-98. doi:10.5853/jos.2017.00829

109. Kolachalama VBB, Bressloff NWW, Nair PBB, Shearman CPP. Predictive Haemodynamics in a One-Dimensional Human Carotid Artery Bifurcation. Part II: Application to Graft Design. *IEEE Trans Biomed Eng*. 2008;55(3):1176-1184. doi:10.1109/TBME.2007.912398

110. Schirmer CM, Malek AM. Computational fluid dynamic characterization of carotid bifurcation stenosis in patient-based geometries. *Brain Behav*. 2012;2(1):42-52. doi:10.1002/brb3.25

111. Liu X, Ren L, Xiong H, et al. Functional assessment of the stenotic carotid artery by CFD based pressure gradient evaluation. *Am J Physiol Hear Circ Physiol*. 2016;(47):645-653. doi:10.1152/ajpheart.00888.2015

112. Kefayati S, Milner JS, Holdsworth DW, Poepping TL. In Vitro Shear Stress Measurements Using Particle Image Velocimetry in a Family of Carotid Artery Models: Effect of Stenosis Severity, Plaque Eccentricity, and Ulceration. Mofrad MRK, ed. *PLoS One*. 2014;9(7):e98209. doi:10.1371/journal.pone.0098209

113. Asgharzadeh H, Asadi H, Meng H, Borazjani I. A non-dimensional parameter for classification of the flow in intracranial aneurysms. II. Patient-specific geometries. *Phys Fluids*. 2019;31(3):031905. doi:10.1063/1.5081451

114. Xu P, Liu X, Zhang H, et al. Assessment of boundary conditions for CFD simulation in human carotid artery. *Biomech Model Mechanobiol*. 2018. doi:10.1007/s10237-018-1045-4

115. Chen Y, Zhang P, Deng X, Fan Y, Xing Y, Xing N. Improvement of hemodynamic performance using novel helical flow vena cava filter design. *Sci Rep*. 2017;7(1):40724. doi:10.1038/srep40724

116. Antiga L, Steinman DA. Robust and objective decomposition and mapping of bifurcating vessels. *IEEE Trans Med Imaging*. 2004;23(6):704-713. doi:10.1109/TMI.2004.826946

117. Cicha I, Wörner A, Urschel K, et al. Carotid Plaque Vulnerability A Positive Feedback Between Hemodynamic and Biochemical Mechanisms. 2011. doi:10.1161/STROKEAHA.111.627265/-/DC1

118. Filardi V. Carotid artery stenosis near a bifurcation investigated by fluid dynamic analyses. *Neuroradiol J*. 2013;26(4):439-453. doi:10.1177/197140091302600409

119. Hosseini HS, Taber LA. How mechanical forces shape the developing eye. *Prog Biophys Mol Biol*. 2018;137:25-36. doi:10.1016/j.pbiomolbio.2018.01.004

120. Li Z-Y, Tan FPP, Soloperto G, Wood NB, Xu XY, Gillard JH. Flow pattern analysis in a highly stenotic patient-specific carotid bifurcation model using a turbulence model. *Comput Methods Biomech Biomed Engin*. 2015;18(10):1099-1107. doi:10.1080/10255842.2013.873033

121. Malota Z, Glowacki J, Sadowski W, Kostur M. Numerical analysis of the impact of flow rate, heart rate, vessel geometry, and degree of stenosis on coronary hemodynamic indices. *BMC Cardiovasc Disord*. 2018;18(1):132. doi:10.1186/s12872-018-0865-6

122. Gharahi H, Zambrano BA, Zhu DC, DeMarco JK, Baek S. Computational fluid dynamic simulation of human carotid artery bifurcation based on anatomy and volumetric blood flow rate measured with magnetic resonance imaging. *Int J Adv Eng Sci Appl Math*. 2016;8(1):46-60. doi:10.1007/s12572-016-0161-6

123. Marshall I, Zhao S, Papathanasopoulou P, Hoskins P, Xu XY. MRI and CFD studies of pulsatile flow in healthy and stenosed carotid bifurcation models. *J Biomech*. 2004;37(5):679-687. doi:10.1016/j.jbiomech.2003.09.032

124. Prim DA, Mohamed MA, Lane BA, et al. Comparative Biaxial Mechanics of Mammalian Carotid Arteries. *PLoS One*. 2018:1-19.

125. Zhao S., Ariff B, Long Q, et al. Inter-individual variations in wall shear stress and mechanical stress distributions at the carotid artery bifurcation of healthy humans. *J Biomech*. 2002;35(10):1367-1377. doi:10.1016/S0021-9290(02)00185-9

126. Vignon-Clementel IE, Figueroa CA, Jansen KE, Taylor CA. Outflow boundary conditions for 3D simulations of non-periodic blood flow and pressure fields in deformable arteries. *Comput Methods Biomech Biomed Engin*. 2010;13(5):625-640. doi:10.1080/10255840903413565

127. Goldstein LB. Extracranial Carotid Artery Stenosis. 2003. doi:10.1161/01.STR.0000097803.90702.31

128. Tian F-B, Zhu L, Fok P-W, Lu X-Y. Simulation of a pulsatile non-Newtonian flow past a stenosed 2D artery with atherosclerosis. *Comput Biol Med*. 2013;43(9):1098-1113. doi:10.1016/J.COMPBIOMED.2013.05.023

129. Debakey ME, Lawrie GM, Glaeser DH. Patterns of Atherosclerosis and their Surgical Significance. *Ann Surg*. 1985;201(2):132. doi:10.1097/00000658-198502000-00001

130. Zarins CK, Giddens DP, Bharadvaj BK, Sottiurai VS, Mabon RF, Glagov S. Carotid bifurcation atherosclerosis. Quantitative correlation of plaque localization with flow velocity profiles and wall shear stress. *Circ Res*. 1983;53(4):502-514. http://www.ncbi.nlm.nih.gov/pubmed/6627609. Accessed September 19, 2018.

131. Holme PA, Orvim U, Hamers MJ, et al. Shear-induced platelet activation and platelet microparticle formation at blood flow conditions as in arteries with a severe stenosis. *Arterioscler Thromb Vasc Biol*. 1997;17(4):646-653. http://www.ncbi.nlm.nih.gov/pubmed/9108776. Accessed September 19, 2018.

132. Su B, Huo Y, Kassab GS, et al. Numerical investigation of blood flow in three-dimensional porcine left anterior descending artery with various stenoses. *Comput Biol Med*. 2014;47(1):130-138. doi:10.1016/j.compbiomed.2014.01.001

133. Gallo D, Steinman DA, Morbiducci U. Insights into the co-localization of magnitude-based versus direction-based indicators of disturbed shear at the carotid bifurcation. *J Biomech*. 2016;49(12):2413-2419. doi:10.1016/j.jbiomech.2016.02.010

134. Lee S-W, Antiga L, Steinman DA. Correlations Among Indicators of Disturbed Flow at the Normal Carotid Bifurcation. *J Biomech Eng*. 2009;131(6):061013. doi:10.1115/1.3127252

135. Markl M, Wegent F, Zech T, et al. In Vivo Wall Shear Stress Distribution in the Carotid Artery Effect of Bifurcation Geometry, Internal Carotid Artery Stenosis, and Recanalization Therapy. 2010. doi:10.1161/CIRCIMAGING.110.958504

136. Banks J, Bressloff NW. Turbulence Modeling in Three-Dimensional Stenosed Arterial Bifurcations. *J Biomech Eng*. 2007;129(1):40. doi:10.1115/1.2401182

137. Stroud JS, Berger SA, Saloner D. Numerical Analysis of Flow Through a Severely Stenotic Carotid Artery Bifurcation. *J Biomech Eng*. 2002;124(1):9. doi:10.1115/1.1427042

138. Tan FPP, Soloperto G, Bashford S, et al. Analysis of Flow Disturbance in a Stenosed Carotid Artery Bifurcation Using Two-Equation Transitional and Turbulence Models. *J Biomech Eng*. 2008;130(6):061008. doi:10.1115/1.2978992

139. Cetin S, Unal G. A higher-order tensor vessel tractography for segmentation of vascular structures. *IEEE Trans Med Imaging*. 2015;34(10):2172-2185. doi:10.1109/TMI.2015.2425535

140. Kweon J, Yang DH, Kim GB, et al. Four-dimensional flow MRI for evaluation of post-stenotic turbulent flow in a phantom: comparison with flowmeter and computational fluid dynamics. *Eur Radiol*. 2016;26(10):3588-3597. doi:10.1007/s00330-015-4181-6

141. Benjamin EJ, Blaha MJ, Chiuve SE, et al. Heart Disease and Stroke Statistics—2017 Update: A Report From the American Heart Association. *Circulation*. 2017;135(10):e146-e603. doi:10.1161/CIR.0000000000000485

142. Fowkes FGR, Rudan D, Rudan I, et al. Comparison of global estimates of prevalence and risk factors for peripheral artery disease in 2000 and 2010: a systematic review and analysis. *Lancet*. 2013;382(9901):1329-1340. doi:10.1016/S0140-6736(13)61249-0

143. Krishnan P, Faries P, Niazi K, et al. Stellarex Drug-Coated Balloon for Treatment of Femoropopliteal Disease. *Circulation*. 2017;136(12):1102-1113. doi:10.1161/CIRCULATIONAHA.117.028893

144. Laird JR, Schneider PA, Tepe G, et al. Durability of Treatment Effect Using a Drug-Coated Balloon for Femoropopliteal Lesions: 24-Month Results of IN.PACT SFA. *J Am Coll Cardiol*. 2015;66(21):2329-2338. doi:10.1016/J.JACC.2015.09.063

145. Rosenfield K, Jaff MR, White CJ, et al. Trial of a Paclitaxel-Coated Balloon for Femoropopliteal Artery Disease. *N Engl J Med*. 2015;373(2):145-153. doi:10.1056/NEJMoa1406235

146. Schneider PA, Laird JR, Tepe G, et al. Treatment Effect of Drug-Coated Balloons Is Durable to 3 Years in the Femoropopliteal Arteries. *Circ Cardiovasc Interv*. 2018;11(1). doi:10.1161/CIRCINTERVENTIONS.117.005891

147. Tepe G, Laird J, Schneider P, et al. Drug-Coated Balloon Versus Standard Percutaneous Transluminal Angioplasty for the Treatment of Superficial Femoral and Popliteal Peripheral Artery Disease. *Circulation*. 2015;131(5):495-502. doi:10.1161/CIRCULATIONAHA.114.011004

148. Herdeg C, Oberhoff M, Baumbach A, et al. Local paclitaxel delivery for the prevention of restenosis: biological effects and efficacy in vivo. *J Am Coll Cardiol*. 2000;35(7):1969-1976. doi:10.1016/S0735-1097(00)00614-8

149. Waksman R, Serra A, Loh JP, et al. Drug-coated balloons for de novo coronary lesions: results from the Valentines II trial. *EuroIntervention*. 2013;9(5):613-619. doi:10.4244/EIJV9I5A98

150. Popov VL. *Contact Mechanics and Friction*. Berlin, Heidelberg: Springer Berlin Heidelberg; 2017. doi:10.1007/978-3-662-53081-8

151. Shull KR. Contact mechanics and the adhesion of soft solids. *Mater Sci Eng R Reports*. 2002;36(1):1-45. doi:10.1016/S0927-796X(01)00039-0

152. Adams GG, Nosonovsky M. Contact modeling - forces. *Tribol Int*. 2000;33:431-442. www.elsevier.com/locate/triboint. Accessed March 4, 2019.

153. McKee CT, Last JA, Russell P, Murphy CJ. Indentation versus tensile measurements of Young's modulus for soft biological tissues. *Tissue Eng Part B Rev*. 2011;17(3):155-164. doi:10.1089/ten.TEB.2010.0520

154. Xue Z, Huang Y, Hwang KC, Li M. The Influence of Indenter Tip Radius on the Micro-Indentation Hardness. 2002. doi:10.1115/1.1480409

155. Kolachalama VB, Shashar M, Alousi F, et al. Uremic Solute-Aryl Hydrocarbon Receptor-Tissue Factor Axis Associates with Thrombosis after Vascular Injury in Humans. *J Am Soc Nephrol*. 2018;29(3):1063-1072. doi:10.1681/ASN.2017080929

156. Nath A, Li I, Roberts LR, Chan C. Elevated free fatty acid uptake via CD36 promotes epithelial-mesenchymal transition in hepatocellular carcinoma. *Sci Rep*. 2015;5:14752. doi:10.1038/srep14752

157. Zanoni I, Tan Y, Di Gioia M, et al. An endogenous caspase-11 ligand elicits interleukin-1 release from living dendritic cells. *Science*. 2016;352(6290):1232-1236. doi:10.1126/science.aaf3036

158. Kabir J, Lobo M, Zachary I. Staurosporine induces endothelial cell apoptosis via focal adhesion kinase dephosphorylation and focal adhesion disassembly independent of focal adhesion kinase proteolysis. *Biochem J*. 2002;367(Pt 1):145-155. doi:10.1042/BJ20020665

159. Loh JP, Waksman R. Paclitaxel Drug-Coated Balloons: A Review of Current Status and Emerging Applications in Native Coronary Artery De Novo Lesions. *JACC Cardiovasc Interv*. 2012;5(10):1001-1012. doi:10.1016/J.JCIN.2012.08.005

160. Jackson D, Tong D, Layland J. A review of the coronary applications of the drug coated balloon. *Int J Cardiol*. 2017;226:77-86. doi:10.1016/J.IJCARD.2016.09.045

161. Indermuehle A, Bahl R, Lansky AJ, et al. Drug-eluting balloon angioplasty for in-stent restenosis: a systematic review and meta-analysis of randomised controlled trials. doi:10.1136/heartjnl-2012-303945

162. Fischman DL, Leon MB, Baim DS, et al. A Randomized Comparison of Coronary-Stent Placement and Balloon Angioplasty in the Treatment of Coronary Artery Disease. *N Engl J Med*. 1994;331(8):496-501. doi:10.1056/NEJM199408253310802

163. Dan K, Garcia-Garcia HM, Waksman R. Letter by Dan et al Regarding Article, "Treatment Effect of Drug-Coated Balloons Is Durable to 3 Years in the Femoropopliteal Arteries: Long-Term Results of the IN.PACT SFA Randomized Trial." *Circ Cardiovasc Interv*. 2018;11(6). doi:10.1161/CIRCINTERVENTIONS.118.006679

164. Schneider PA, Laird JR, Tepe G, et al. Response by Schneider et al to Letter Regarding Article, "Treatment Effect of Drug-Coated Balloons Is Durable to 3 Years in the Femoropopliteal Arteries: Long-Term Results of the IN.PACT SFA Randomized Trial." *Circ Cardiovasc Interv*. 2018;11(6). doi:10.1161/CIRCINTERVENTIONS.118.006699

165. Scheinert D, Duda S, Zeller T, et al. The LEVANT i (lutonix paclitaxel-coated balloon for the prevention of femoropopliteal restenosis) trial for femoropopliteal revascularization: First-in-human randomized trial of low-dose drug-coated balloon versus uncoated balloon angioplasty. *JACC Cardiovasc Interv*. 2014;7(1):10-19. doi:10.1016/j.jcin.2013.05.022

166. Tepe G, Zeller T, Albrecht T, et al. Local Delivery of Paclitaxel to Inhibit Restenosis during Angioplasty of the Leg. *N Engl J Med*. 2008;358(7):689-699. doi:10.1056/NEJMoa0706356

167. Rissanen TT, Uskela S, Eränen J, et al. Drug-coated balloon for treatment of de-novo coronary artery lesions in patients with high bleeding risk (DEBUT): a single-blind, randomised, non-inferiority trial. *Lancet*. 2019;394(10194):230-239. doi:10.1016/S0140-6736(19)31126-2

168. Katsanos K, Spiliopoulos S, Kitrou P, Krokidis M, Karnabatidis D. Risk of Death Following Application of Paclitaxel-Coated Balloons and Stents in the Femoropopliteal Artery of the Leg: A Systematic Review and Meta-Analysis of Randomized Controlled Trials. *J Am Heart Assoc*. 2018;7(24). doi:10.1161/JAHA.118.011245

169. Anderson JA, Lamichhane S, Remund T, Kelly P, Mani G. Preparation, characterization, in vitro drug release, and cellular interactions of tailored paclitaxel releasing polyethylene oxide films for drug-coated balloons. *Acta Biomater*. 2016;29:333-351. doi:10.1016/j.actbio.2015.09.036

170. Lamichhane S, Anderson J, Remund T, Kelly P, Mani G. Dextran sulfate as a drug delivery platform for drug-coated balloons: Preparation, characterization, *in vitro*

drug elution, and smooth muscle cell response. *J Biomed Mater Res Part B Appl Biomater*. 2016;104(7):1416-1430. doi:10.1002/jbm.b.33494

171. Mandal PK, Sarifuddin, Kolachalama VB. Computational Model of Drug-Coated Balloon Delivery in a Patient-Specific Arterial Vessel with Heterogeneous Tissue Composition. *Cardiovasc Eng Technol*. 2016;7(4):406-419. doi:10.1007/s13239-016-0273-y

172. Kempin W, Kaule S, Reske T, et al. In vitro evaluation of paclitaxel coatings for delivery via drug-coated balloons. *Eur J Pharm Biopharm*. 2015;96:322-328. doi:10.1016/j.ejpb.2015.08.010

173. Kotzan AS, Nagel S, Reske T, et al. In vitro determination of drug transfer from drug-coated balloons. *PLoS One*. 2013;8(12):2-9. doi:10.1371/journal.pone.0083992

174. Speck U, Stolzenburg N, Peters D, Scheller B. How does a drug-coated balloon work? Overview about coating technologies and their impact. *J Cardiovasc Surg*. 2015. doi:R37Y9999N00A150095 [pii]

175. Cortese B, Bertoletti A. Paclitaxel coated balloons for coronary artery interventions: A comprehensive review of preclinical and clinical data. *Int J Cardiol*. 2012;161(1):4-12. doi:10.1016/j.ijcard.2011.08.855

176. Hehrlein C. Drug-coated balloons-the importance of packing and dosing antiproliferative drugs. *Catheter Cardiovasc Interv*. 2015;86(2):287-288. doi:10.1002/ccd.26091

177. Richey T, Iwata H, Oowaki H, Uchida E, Matsuda S, Ikada Y. Surface modification of polyethylene balloon catheters for local drug delivery. *Biomaterials*. 2000;21(10):1057-1065. doi:10.1016/S0142-9612(99)00281-1

178. Woolford SE, Tran M, NguyenPho A, McDermott MK, Oktem B, Wickramasekara S. Optimization of balloon coating process for paclitaxel coated balloons via micro-pipetting method. *Int J Pharm*. 2019;554:312-321. doi:10.1016/j.ijpharm.2018.11.006

179. Xue C, Lott JT, Kolachalama VB. Estimation of Size and Contact Angle of Evaporating Sessile Liquid Drops Using Texture Analysis. 2019. doi:10.1021/acs.langmuir.8b04043

180. Giacoppo D, Cassese S, Harada Y, et al. Drug-Coated Balloon Versus Plain Balloon Angioplasty for the Treatment of Femoropopliteal Artery Disease An Updated Systematic Review and Meta-Analysis of Randomized Clinical Trials. 2016. doi:10.1016/j.jcin.2016.06.008

181. Giacoppo D, Alfonso F, Xu B, et al. Paclitaxel-coated balloon angioplasty vs. drug-eluting stenting for the treatment of coronary in-stent restenosis: a comprehensive, collaborative, individual patient data meta-analysis of 10

randomized clinical trials (DAEDALUS study). *Eur Heart J*. September 2019. doi:10.1093/eurheartj/ehz594

182. Klumb C, Lehmann T, Aschenbach R, Eckardt N, Teichgräber U. Benefit and risk from paclitaxel-coated balloon angioplasty for the treatment of femoropopliteal artery disease: A systematic review and meta-analysis of randomised controlled trials. *EClinicalMedicine*. 2019;16:42-50. doi:10.1016/j.eclinm.2019.09.004

183. Tesfamariam B. Local arterial wall drug delivery using balloon catheter system. *J Control Release*. 2016;238:149-156. doi:10.1016/j.jconrel.2016.07.041

184. Tzafriri AR, Parikh SA, Edelman ER. Taking paclitaxel coated balloons to a higher level: Predicting coating dissolution kinetics, tissue retention and dosing dynamics. *J Control Release*. 2019;310:94-102. doi:10.1016/j.jconrel.2019.08.019

185. Vig JR. UV/ozone cleaning of surfaces. *J Vac Sci Technol A Vacuum, Surfaces, Film*. 1985;3(3):1027-1034. doi:10.1116/1.573115

186. Siegbahn K. Electron Spectroscopy for Atoms, Molecules, and Condensed Matter. *Science (80-)*. 1982;217(4555):111-121. doi:10.1126/science.217.4555.111

187. Andrade JD. X-ray Photoelectron Spectroscopy (XPS). In: *Surface and Interfacial Aspects of Biomedical Polymers*. Boston, MA: Springer US; 1985:105-195. doi:10.1007/978-1-4684-8610-0_5

APPENDIX A

JOURNAL PERMISSION FOR USE OF MANUSCRIPT

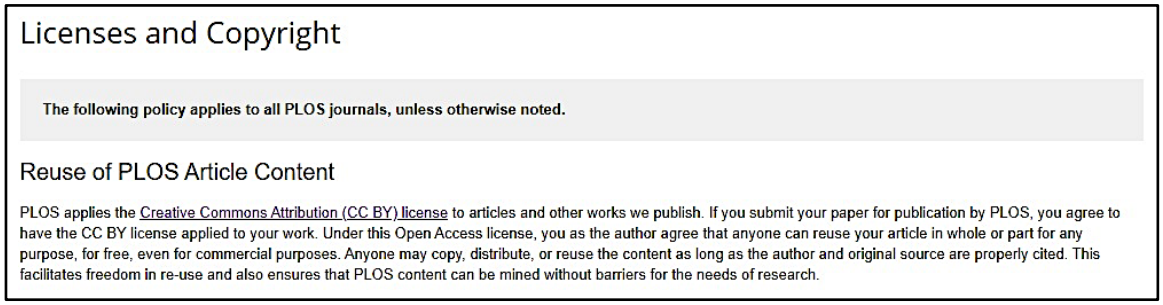

Licenses and Copyright

The following policy applies to all PLOS journals, unless otherwise noted.

Reuse of PLOS Article Content

PLOS applies the Creative Commons Attribution (CC BY) license to articles and other works we publish. If you submit your paper for publication by PLOS, you agree to have the CC BY license applied to your work. Under this Open Access license, you as the author agree that anyone can reuse your article in whole or part for any purpose, for free, even for commercial purposes. Anyone may copy, distribute, or reuse the content as long as the author and original source are properly cited. This facilitates freedom in re-use and also ensures that PLOS content can be mined without barriers for the needs of research.

Figure A.1: Permission from PLOS Journals – PLOS One to include published manuscript in this dissertation.
Chapter 2 is included in this dissertation with permission from the publisher. Information can be found at <https://journals.plos.org/plosone/s/licenses-and-copyright>

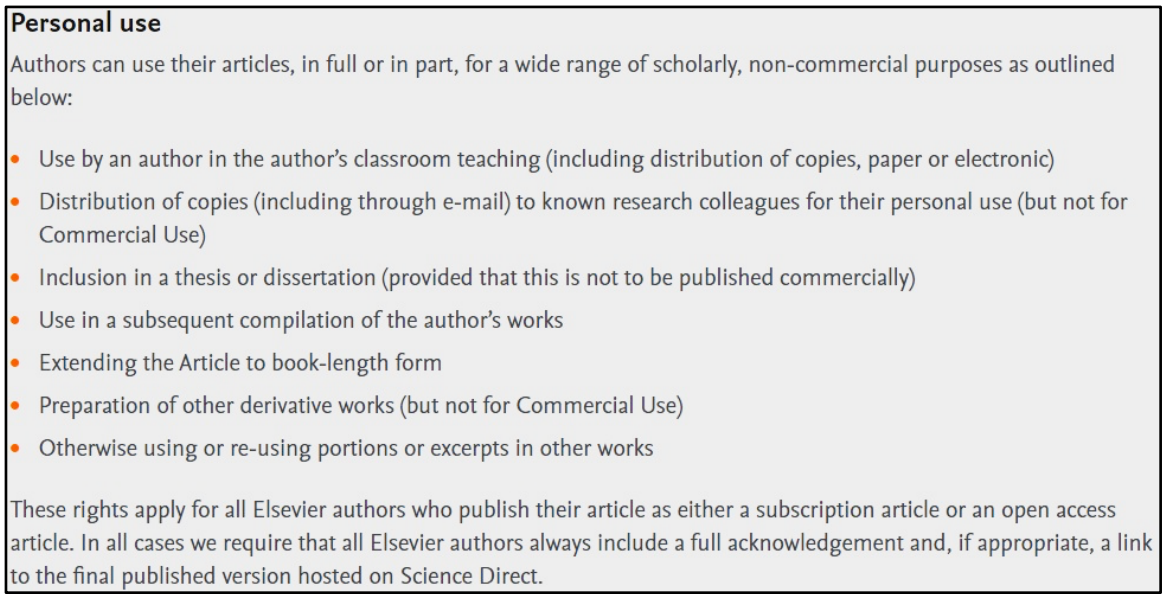

Personal use

Authors can use their articles, in full or in part, for a wide range of scholarly, non-commercial purposes as outlined below:

- Use by an author in the author's classroom teaching (including distribution of copies, paper or electronic)
- Distribution of copies (including through e-mail) to known research colleagues for their personal use (but not for Commercial Use)
- Inclusion in a thesis or dissertation (provided that this is not to be published commercially)
- Use in a subsequent compilation of the author's works
- Extending the Article to book-length form
- Preparation of other derivative works (but not for Commercial Use)
- Otherwise using or re-using portions or excerpts in other works

These rights apply for all Elsevier authors who publish their article as either a subscription article or an open access article. In all cases we require that all Elsevier authors always include a full acknowledgement and, if appropriate, a link to the final published version hosted on Science Direct.

Figure A.2: Permission from Elsevier Journals – Computers in Biology and Medicine to include published manuscript in this dissertation.

Chapter 3 is included in this dissertation with permission from the publisher. Information can be found at <https://www.elsevier.com/about/policies/sharing> and <https://www.elsevier.com/about/policies/copyright>. Included article can be found at <https://doi.org/10.1016/j.compbiomed.2019.103436>

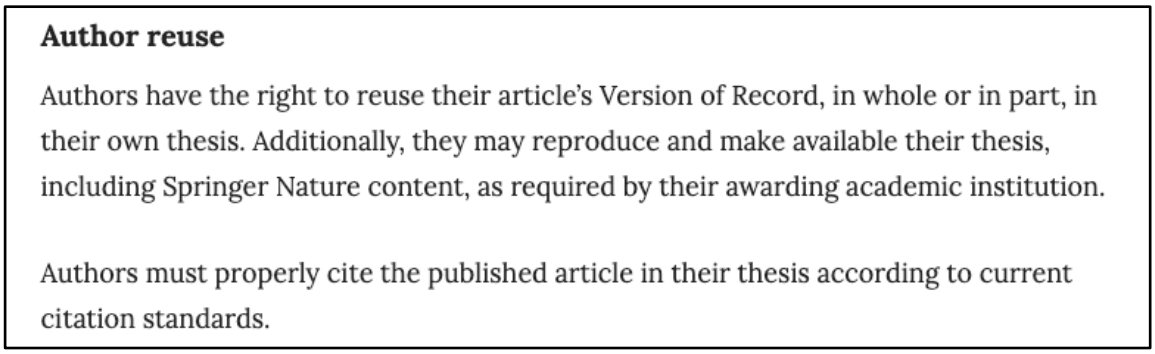

Author reuse

Authors have the right to reuse their article's Version of Record, in whole or in part, in their own thesis. Additionally, they may reproduce and make available their thesis, including Springer Nature content, as required by their awarding academic institution.

Authors must properly cite the published article in their thesis according to current citation standards.

Figure A.3: Permission from Springer Nature – Scientific Reports to include published manuscript in this dissertation.

Chapter 4 is included in this dissertation with permission from the publisher. Information can be found at <https://www.nature.com/nature-research/reprints-and-permissions/permissions-requests>

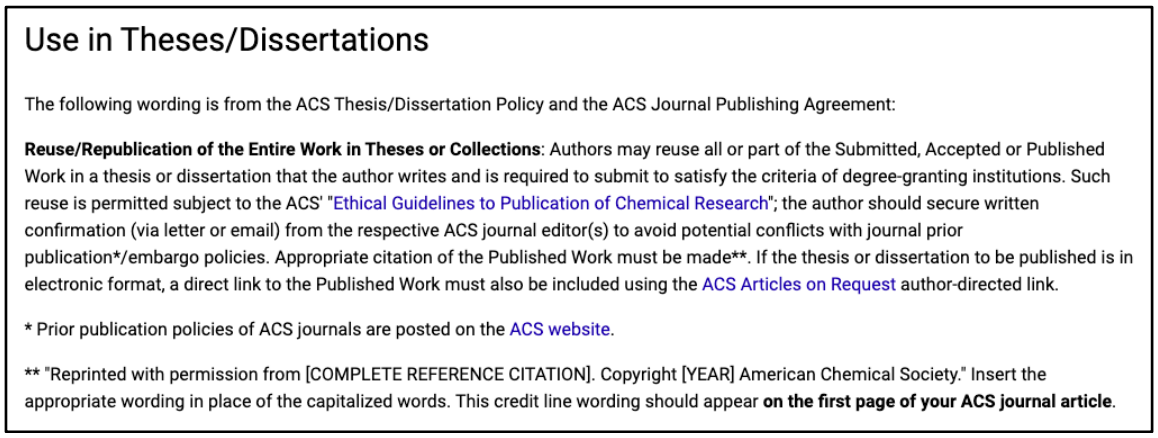

Use in Theses/Dissertations

The following wording is from the ACS Thesis/Dissertation Policy and the ACS Journal Publishing Agreement:

Reuse/Republication of the Entire Work in Theses or Collections: Authors may reuse all or part of the Submitted, Accepted or Published Work in a thesis or dissertation that the author writes and is required to submit to satisfy the criteria of degree-granting institutions. Such reuse is permitted subject to the ACS' "Ethical Guidelines to Publication of Chemical Research"; the author should secure written confirmation (via letter or email) from the respective ACS journal editor(s) to avoid potential conflicts with journal prior publication*/embargo policies. Appropriate citation of the Published Work must be made**. If the thesis or dissertation to be published is in electronic format, a direct link to the Published Work must also be included using the ACS Articles on Request author-directed link.

* Prior publication policies of ACS journals are posted on the ACS website.

** "Reprinted with permission from [COMPLETE REFERENCE CITATION]. Copyright [YEAR] American Chemical Society." Insert the appropriate wording in place of the capitalized words. This credit line wording should appear **on the first page of your ACS journal article**.

Figure A.4: Permission from ACS Publications – Langmuir to include submitted, accepted or published manuscript in this dissertation.

Chapter 5 is included in this dissertation with permission from the publisher. Information can be found at <https://pubs.acs.org/page/copyright/permissions_otherpub.html>